



Office of Graduate Studies

Dissertation / Thesis Approval Form

This form is for use by all doctoral and master's students with a dissertation/thesis requirement. Please print clearly as the library will bind a copy of this form with each copy of the dissertation/thesis. All doctoral dissertations must conform to university format requirements, which is the responsibility of the student and supervising professor. Students should obtain a copy of the Thesis Manual located on the library website.

Dissertation/Thesis Title: Exploring the Electronic Landscape at Interfaces and Junctions in Semiconductor Nanowire Devices with Subsurface Local Probing of Carrier Dynamics.

Author: Terrence McGuckin

This dissertation/thesis is hereby accepted and approved.

Signatures:

Examining Committee

Chair _____

Members _____

Academic Advisor _____

Department Head _____

**Exploring the Electronic Landscape at Interfaces and Junctions in Semiconductor Nanowire
Devices with Subsurface Local Probing of Carrier Dynamics.**

A Thesis

Submitted to the Faculty

of

Drexel University

by

Terrence McGuckin

in partial fulfillment of the

requirements for the degree

of

Doctor of Philosophy

July 2015

© Copyright 2015
Terrence McGuckin.

This work is licensed under the terms of the Creative Commons Attribution-ShareAlike license Version 3.0. The license is available at
<http://creativecommons.org/licenses/by-sa/3.0/>.

Dedications

I dedicate this thesis to Zoe and Calyx, my two favorite people. I love you.

Acknowledgments

My greatest thanks goes towards my thesis advisor Dr. Jonathan Spanier, for his support and patience throughout the PhD process at Drexel. The most important part of any endeavor is the journey, and my personal journey has been a bit unusual for most PhD students, and I'm glad to have shared this time together. With out the latitude to see how far we could use EBIC as a technique, none of this research would have been possible. I would also like to thank my thesis committee, Dr. Jason Baxter, Dr. Steven May, Dr. Daniel Gianola, Dr. Timothy Kurweig, and Dr. Caroline Schauer. I have appreciated all their feedback and suggestions and have lead me to better present my work and develop as a scientist. Dr. Schauer was the graduate advisor for most of my time at Drexel and has always offered guidance, I am deeply honored that she was also my committee chair.

The people that made this experience the most rewarding are the members of the Spanier research group, who are not only very gifted scientists but are dear friends. Special thanks goes towards Dr. Guannan Chen for our work in applying EBIC to study radial hetero-structures in core shell AlGaAs/ GaAs nanowires. This project was one of the most rewarding and we both learned and tremendous amount and tackled a very complex problem. Dr. Chris Hawley was incredibly generous with his time in discussing manuscripts and providing essential feedback. All of the TEM images of the Si MACE nanowires were taken by Chris. Guannan and Chris both grew the Ge nanowires I used in my measurements. Dr. Maria Torres came to our group at a time of transition and made us a much more cohesive group. Maria and I embarked on studying BFO and PZT with EBIC and we discovered that the absorbed current response had a direct correlation to domains in that material and she confirmed it with PFM. Dr. Oren Leaffer was always very generous with his time and was instrumental in debugging one of the earlier EBIC prototypes that lead to the majority of the work presented in this thesis. Dr. Stephanie Johnson joined the Spanier group the same year as I did, we supported each other through out graduate school and I'm glad to count her as a friend. Dr. Eric Gallo and Dr. Stephen Nonnenmann were great mentors in becoming and new grad student.

I learned most of my fabrication knowledge from them. Special thanks goes to Dr. Tsachi Livneh, who was a great mentor and I had the pleasure of exploring MoS₂ devices with EBIC.

The majority of EBIC measurements were conducted in Drexel's CRF. If it wasn't for the help and great patience of Dr. Craig Johnson and Dr. Edward Basgall I wouldn't have been able to interface to the FEI DB 235 and take all of these great measurements. The Si MACE nanowire project would not have been possible without the input of Dr. Daniel Gianola and his students. The Si MIS nanowires were all fabricated and measured at Brookhaven National Laboratories Center for Functional Nanomaterials. The expertise and time that the staff Dr. Fernando Camino, Dr. Ming Lu, and Dr. Aaron Stein provided is deeply appreciated. Special thanks goes to Dr. Fernando Camino, we performed the EBIC analysis of the Si PN junction on the Helios at the CFN. I greatly appreciate all of his help in making this technique available on the Helios and look forward to our future collaborations.

I want to thank our collaborators in Dr. Lane Martin's group who provided us with the BFO and PZT samples. To Dr. Paola Prete and Dr. Nico Levergne I want to offer my gratitude to providing us the AlGaAs/GaAs nanowires that Guannan fabricated into the devices we measured together.

To Dr. Jean Berney and Sammuel Sonderegger of Attolight I want to thank for all of your support and generosity as colleagues and mentors of my company Ephemeron Labs. I very much look forward to continue making the best correlative microscopy SEM ever!

To my all friends who have offered guidance, support, and love, I can't thank you enough. Specifically, I'd like to thank Andrew Righter a dear friend and kindred spirit who helped me write a Linux kernel driver that was key to making the latest version of our EBIC system a success. To my friends who remind me to always play cosmic jokes on myself, Dr. Justin McDaniel, Kaycie Chute, Tony Sacksteder, Kurt Swanson, Emily Missner, and Kaitlyn Debassie, thanks and right back at you!

My greatest thanks goes to my family. With my partner Amy Kwasnicki, I have shared one of the greatest experiments with the most promising results in building a life together and raising our two children Zoe and Calyx. Zoe just started Kindergarten at the same time I started graduate school, and now she is growing into a dynamic young woman, I couldn't be prouder. Calyx has grown to

be one of the most creative, compassionate, and sincere people I know and he is only eight. Having a family with Amy, Zoe, and Calyx has made everything that much more worth while, and I look forward to the adventures we will share in the future.

Table of Contents

LIST OF TABLES	ix
LIST OF FIGURES	x
ABSTRACT	xvi
1. INTRODUCTION	1
1.1 Thesis Synopsis	3
2. FROM BAND THEORY TO DEVICES	7
2.1 Band Theory	7
2.2 Doping and the Fermi level	8
2.3 Transport Dynamics in Devices	11
2.3.1 Recombination and Generation	13
2.3.2 Current Density Equations	13
2.3.3 Continuity Equations	13
2.4 Device Building Blocks	15
2.4.1 PN Junction	15
2.4.2 Hetero-Junctions	17
2.4.3 Metal Semiconductor Contacts	17
2.4.4 Metal Insulator Semiconductor	18
2.4.5 Defects and Interfaces	19
2.5 Summary	20
3. INTRODUCTION TO EBIC	22
3.1 Signals from Primary E-beam	22
3.2 Probing of Semiconductors	23
3.2.1 Junctions	25
3.2.2 Defects	26

3.2.3	Electron Beam Absorbed Current	28
3.3	Nano-structured Devices	29
3.3.1	EBIC on nanowire devices	30
3.3.2	Simulated local probing	30
3.4	Qualitative EBIC	30
3.5	Quantitative EBIC	33
4.	FABRICATION OF NANOWIRES AND DEVICES	34
4.1	Vapor Liquid Solid Growth	34
4.2	MACE of Silicon Nanowires	35
4.2.1	Etching p-type nanowires	37
4.3	Device Fabrication	42
4.3.1	Nanowire Deposition on a Substrate	42
4.3.2	E-beam Lithography	43
4.3.3	Metal Contacts	45
5.	EVOLUTION OF FIELD-INDUCED IMPACT IONIZATION	48
5.1	Hot carriers	48
6.	GAAs/AlGaAs CORE-SHELL NANOWIRES	59
6.1	Drift-diffusion coupling	61
6.2	Interaction Volume	63
6.3	Characteristic Lengths	64
6.4	Selectively Probing Core and Shell	67
6.5	Radial Profiles	70
6.6	Summary	71
7.	BANDBENDING IN GE NANOWIRES	74
7.1	Experiment setup	76
7.2	Transport Behavior	77
7.3	Evolution of Surface States	79

7.4 Carrier Generation Profile	82
7.4.1 Profiles across the nanowire axis	85
7.4.2 Summary	87
8. LOCAL PROBING OF Si MIS NANOWIRE DEVICES	89
8.0.3 Test structure	89
8.0.4 EBIC of MIS nanowires	90
8.0.5 Summary	95
9. APPLICATIONS TO OTHER SYSTEMS	97
9.1 Electron Beam Absorbed Current	98
9.1.1 Bismuth Ferrite	98
9.1.2 Lead Zirconate Titanate	101
9.2 2D Materials and Devices	102
9.3 Solar Cells	106
10. CONCLUSIONS AND FUTURE WORK	108
10.1 Conclusions	108
10.2 Future Work	109
BIBLIOGRAPHY	111
VITA	119

List of Tables

List of Figures

2.1	Band structure (a)Si, (b) GaAs. Bandgap shown in grey, adapted from ¹	8
2.2	Schematic band diagram, density of states, Fermi Dirac distribution, and carrier concentration for (a) intrinsic,(b) n type, and (c) p-type semiconductors at thermal equilibrium. Adapted from ²	9
2.3	Schematic of an abrupt PN junction. (a) Carrier concentration for holes and electrons on either side of PN junction with p-type and n-type section and space charge region (b) Charge Q from donor and acceptor atoms (c) E field (d)Built in potential ψ_{bi} , integral of E field (e) Band diagram of abrupt junction with intrinsic, E_i and Fermi level E_f labeled.	16
2.4	Energy band diagram of metal-semiconductor contacts. (a) shows metal and semiconductor with repect to vacuum level and the work function and electron affinity(b) connected system with a gap and Fermi levels lining up (c) gap is reduced with enhanced barrier (d) No gap is present. Adapted from ²	18
2.5	Energy band diagram for metal semiconductor junction at thermal equilibrium for (a) n-type , (b) p-type semiconductors.Adapted from ²	18
2.6	Energy band diagram for MIS junction for p-type (top) and n-type (bottom) in (a) Accumulation mode (b) Depletion (c) Inversion mode. Adapted from ² .	19
3.1	Electron beam interaction with sample and signal types.	23
3.2	Monte Carlo simulation of interaction volume of electron beam with Si sample with (a)1kV (b)3kV, and (c) 5kV electron energy. Scale bar is 500nm. Color represents energy released and is normalized to a logarithmic scale.	24
3.3	EBIC schematic of PN junctions. Signal amplifier(shown as an op-amp) provides a virtual ground to the n type contact and the p-type contact is grounded. This allows for two conduction paths to ground and a for carriers to be separated by the built in E-field. (a) Planar EBIC measurement of a buried junction Varying the incident beam energy denoted by the red arrows changes the depth profile. (b) Cross-section of PN junction orthogonal to the imaging plane. Minority carrier diffusion lengths can be directly measure on either side of the junction, as well as the extent of the depletion region.	26
3.4	EBIC schematic of Schottky junctions. Signal amplifier(shown as an op-amp) provides a virtual ground to the contact forming the junction and the other ohmic contact with no barrier is grounded. This allows for two conduction paths to ground and a for carriers to be separated by the built in E-field. (a) Planar EBIC measurement of a buried junctions and can show a net difference in current if defects are located within the depletion region and local have a high recombination rate. (b) Cross-section of Schottky junction orthogonal to the imaging plane. Minority carrier diffusion lengths can be directly measure on one side of the junction, as well as the extent of the depletion region.	27
3.5	EBIC schematic for MSM devices, where there is a blocking contact on either side of the device. This schematic can also work for EBAC where there is only one conduction path to ground and defects can be imaged outside of any depletion region.	28

4.5 E-beam lithography process and metal deposition. (i) Si substrate with 200nm of thermal oxide is spin coated with PMMA. (ii) where PMMA is exposed to E-beam it dissolves in development process. (iii) Deposition of metal on sample both exposed area and PMMA. (iv) metal is deposited on substrate after lift off process where PMMA is dissolved in NMP removing un-patterned metal.	44
4.6 (a) Si MIS device with e-beam defined contacts (1-2) are ohmic contacts with sputtered Al with 1 percent Si(3) is a Schottky contact with oxide left underneath as a barrier, scale bar is $2 \mu\text{m}$. (b) Several devices fabricate on one substrate, scale bar is $500 \mu\text{m}$	44
5.1 (a) Schematic of EBIC measurements, (b) SEM image of MSM contacted GeNW (diameter 60 nm, scale bar is $1 \mu\text{m}$), and (c) EBIC images with V_b denoted in each. Each image is normalized relative to a maximum current scale bar is 500 nm. (d) Current-voltage data for the GeNW prior to (red, solid) and following (black, with crosses) EBIC imaging and the formation of a localized high E-field near the anode and is attributed to dislocations. (d) Current vs voltage measurements conduct before and after EBIC measurements are conducted. The response before EBIC is characteristic of a MSM device with Schottky contacts at each end. The hysteresis in the measurements after EBIC is attributed to dislocations charging and discharging that were formed after impact ionization process.	52
5.2 (a) Current profiles taken from EBIC images at selected values of V_b for the GeNW shown in Fig. 5.1 as denoted in the legend. The locations of the cathode (1) and anode (2) are denoted by dashed lines. (b) Corresponding potential profiles obtained from integrating the current. The EBIC profile for $V_b = 0.96\text{V}$ (black, solid) was collected last among this series of EBIC data on this device, and the local maximum in the EBIC current is seen to be much larger than that collected for nearly all other (larger) values of V_b . (c) EBIC profiles collected at $V_b = 6.5\text{V}$ with $V_g = -1$ and $V_g = -3\text{V}$. Also shown in (c) is that for reverse polarity (RP) ($V_b = -6.5\text{V}$), and its corresponding potential profile (d) (dashed red lines in each); for the trace collected under reverse bias, (1) and (2) denote the locations of the anode and cathode, respectively.	54
5.3 (a) Current profiles collected from a separate Schottky-contacted GeNW (diameter 100 nm) under $V_g = 0\text{V}$, -1V , and -3V after a dislocation near the anode (2) was formed under the same bias condition as that for the other GeNW, with the cathode location denoted here by (1). (b) EBIC profiles obtained with this GeNW at lower biases were qualitatively similar to that of the wire shown in Fig. 5.2 although the response for this GeNW is considerably larger than the incident beam current. Gating of the GeNW is seen to predominately affect the dislocation(s) centered at $0.85 \mu\text{m}$	56
6.1 Evolution of the electronic landscape at the onset of small bias voltage. (a) EBIC images and selected line profiles $V_b = 0 \text{ V}$ (middle) and $V_b = 0.1 \text{ V}$ (bottom) taken along the center axis of the nanowire (red dash-dot line in SEM image). The right side contact is grounded. The black dash-dot lines denote zero current. The scale bar is 500 nm. A circuit diagram is superimposed on the SEM image to indicate the bias direction. (b) Series of EBIC images collected $-20 \text{ mV} < V_b < +20 \text{ mV}$. Red dots indicate the location along the nanowire where the sign of the current changes. (c) The EBIC central axis line profiles extracted from (b). Profiles are offset by 50 pA for clarity.	64

6.2 EBIC at low accelerating voltage V_{acc} . (a) EBIC maps of a single NW device at $V_b = 0.1, 0.2, 0.3, 0.4$, and 0.5 V (right side contact is grounded). White dashed lines indicate the locations of the contacts. The secondary electron image (top) is collected simultaneously, and the scale bar is 500 nm. (b) Line profiles along NW axial direction. Best fittings are shown in solid lines (black) on both sides of the EBIC signal maxima. (c) the electron drift component (solid squares) is separated from the diffusion-drift decay length (open circles); both are plotted versus V_b . The line in (c) is a linear fit of the drift length vs. V_b .	65
6.3 Beam energy-selective EBIC revealing transport in GaAs core. (a) Illustration of beam interaction with the two parallel transport channels having different excess carrier transport properties. The different length of red arrows indicates the mobility difference and the purple arrow indicates the possible interaction between the core and the shell. (b) Comparison of the EBIC line profiles under $V_{acc} = 5$ kV (black) and $V_{acc} = 10$ kV (red) at $V_b = 0.5$ V. Inset shows evolution of the decay lengths versus V_b for $V_{acc} = 5$ kV (black squares) and $V_{acc} = 10$ kV (red squares). Monte-Carlo simulations of (c) beam trajectories when the beam is on the central NW axis and (d) carrier generation dependence on beam incident positions obtained by integrating in core and shell areas in maps, for (e) in GaAs/Al _{0.24} Ga _{0.76} As nanowire cross-sections with hexagonal facets, under two different values of V_{acc} . (e) EBIC profiles at central axis (black) and side axis in shell region (red) as denoted in the inset (scale bar is 500 nm), revealing opposite drift directions.	68
6.4 High-resolution radial profiles at zero bias. (a) and (e) Radial line profiles extracted at 200 nm intervals with $V_{acc} = 10$ kV and $V_{acc} = 3$ kV from EBIC maps (b) and (d) respectively, where black dashed lines denote the corresponding axial locations from which profiles in (a) and (e) have been extracted in an electrically-interfaced nanowire as illustrated in (c). Radial line profiles presented in (a) and (e) have two colors: red indicates positive current and blue negative. Grey areas in (a) and (e) denote areas exterior to the nanowire. Radial current profiles are offset by 20 pA in (a) and 10 pA in (e) for clarity.	70
7.1 (a) Secondary image of Ge nanowire (b) EBIC image taken at 0 V bias, after a 5.0V voltage sweep showing parallel conduction channels for holes (outer shell) and electrons (center), scale bar is 500 nm. The spatial resolution of the scan is 5 nm.	77
7.2 In-situ current vs. voltage sweeps of Ge nanowire inside the SEM chamber with the beam blanked(dark current response). Measurements are taken after EBIC scan held at previous voltage.(a) Voltage sweeps from 0.2 V, 0.4 V, 0.6 V, 0.8 V, and 1.0 V with EBIC scans taken after each sweep. (b) Voltage sweeps from 1.0 V, 1.4 V, 2.0 V, 2.5 V, 3.0 V, 4.0 V, 5.0 V, EBIC scans taken after each each sweep.	78
7.3 EBIC images from scans after 0.0 V to 1.0 V sweeps applied . (a) Sequence of EBIC profiles along the left side(green), right side(blue) of the Ge nanowire axis, profile from the center. Profiles are offset by 75pA for each scan. The profiles extracted from EBIC images (b). (b) Scale bar for EBIC images is 100 nm.	80
7.4 EBIC images from scans after from 1.4 V to 5.0 V sweeps. (a) Sequence of EBIC profiles along the left side(green), right side(blue) of the Ge nanowire axis, profile from center (black). The cross over point for where the center(black) and side profiles(green, blue) diverge is denoted with magenta circle. The first cross over point(after 1.4 V sweep) and the last(5.0 V sweep) are marked with cyan dashed lines. Profiles are offset by 75pA for each scan. The profiles extracted from EBIC images (b), scale bar for EBIC images is 100 nm.	81

7.5 (a) Band diagram along the axis of the Ge nanowire depicting the depletion region due to the Schottky contacts at either end. (b) Band diagram in radial direction in regions away from Schottky contact, shows electrons in traps at the surface (black dots), and holes open circles accumulating near the surface of the nanowire. (c) illustration showing the depletion in gray	83
7.6 (Monte Carlo electron flights simulations of 1000 electrons at -40 nm (a) , 0 nm (b), and +40 nm(c) beam positions. (d) Radial distribution of carriers generated from beam positions 45 nm to 5 nm, with 50 nm the center of the 100 nm nanowire. (e) Simulated cross sectional profiles, total Δn , Δp created per incident electron within the nanowire moving the incident beam position 5nm for each point in the depleted zone region I(green) and the neutral zone region II(blue). Also plotted are the sum(red) of the two regions and the difference (black).	84
7.7 Cross-section profiles and EBIC images after 0.0 V to 0.6 voltage sweeps, taken at 150 nm intervals across the nanowire axis from corresponding EBIC image and voltage bias profiles are offset -37pA for each interval the dash lines denote the section of the image plotted in profile. The scale bar in the EBIC images is 100nm. The all units are in pA	86
7.8 Cross-section profiles and EBIC images taken after voltage sweeps from 1.0 V to 4.0 V , taken at 150 nm intervals across the nanowire axis from corresponding EBIC image and voltage bias profiles are offset -37pA for each interval the dash lines denote the section of the image plotted in profile. The scale bar in the EBIC images is 100nm. The all units are in pA	87
8.1 Side view of MIS test structure Schottky contact is shown in yellow, deposition of metal is directional and not continuous for thin extended contact that is electron transparent. Si nanowire is shown in pink, with ohmic contact in grey.	90
8.2 (a)Secondary electron image of p-type Si nanowire with sputtered aluminum contact and evaporated contacts,A thicker 120 nm evaporated contact goes over the sputtered Al contact to maintain electrical continuity form the top of the nanowire to the electrode contacts, scale bar is $2\mu m$. (b) Progressive EBIC scans from 0 V to 4.0 V bias. The left contact is the cathode the right contact is the anode. Acceleration voltage of the e-beam is 10kV, probe current is 100pA	91
8.3 EBIC image of Si nanowire Fig. 8.2 with extracted profile(a) 4 V bias applied to device, scale bar is $2 \mu m$. (b)extracted profile from (a) along dashed line. Region 1,2 underneath MIS contact of sputter 12nm Al. Region 1(pink) denotes where diffusion length near cathode. Region 3(green) drift/diffusion length from anode.(a) and (b) are aligned to extracted profile.	92
8.4 SE and EBIC images collected from Si MIS NW device at 5kV.(a)SE image, scale bar $2\mu m$. (b)EBIC image (c) Extracted profile from (b) dashed line signal from MIS contact.	93
8.5 EBIC images under MIS contact of Si nanowire with extracted profiles denoted by dashed black lines(a) 0 V bias, scale bar 125 nm. (b) 6 V bias, scale bar 150 nm. EBIC profiles are offset by -40 pA and are extracted from EBIC images at the dashed lines.	95
9.1 (a)Bismuth Ferrite Domains imaged by EBAC, scale bar in 250 nm. (b)Profile extracted from (a) orthogonal to domain orientation denoted by dashed line. Signal level is less than 0.5 pA between domains	99

9.2 Carbon contamination from overlapping scan blue area as an offset compared to red area. Contrast mechanism does not change, scale bar is 320 nm.	100
9.3 EBAC of PZT A and C domains are visible ,scale bar is 540 nm, acceleration voltage of 5kV101	
9.4 EBAC of PZT both A and C domains are visible, with triangular defects with the same crystallographic orientation, scale bar is 240 nm.	102
9.5 EBIC response of MoS ₂ device with two electrodes at 0V bias, the sample has multiple layers that overlap, scale bar is 1.5 μ m	103
9.6 Higher magnification scan showing one electrode of MoS ₂ device at 0 V bias. Interfaces between layers are visible in EBIC mode as well as folding of layers., scale bar is 620 nm.	104
9.7 Multi layer MoS ₂ device with Cr/Au contacts(a)1 V bias (b) 3 V bias (c)5 V bias. Scale bars are 620 nm.	105
9.8 Cross section of Si solar cell p-type substrate with n-type top layer simultaneous sampling of SE and EBIC (a)SE image, scale bar 5 microns(b)EBIC image, scale bar 5 microns, green dashed line shows position extracted profile.(c)Extracted profile from (b), inset shows close up profile of ridges due to doping profile(d) natural log of (c) (inverted) with least squares fit L_P , dashed red line and L_n dashed green line on either side of depletion region.	106

Abstract

Exploring the Electronic Landscape at Interfaces and Junctions in Semiconductor Nanowire Devices
with Subsurface Local Probing of Carrier Dynamics.

Terrence McGuckin
Jonathan E. Spanier

The solid state devices that are pervasive in our society are based on building blocks composed of interfaces between materials and junctions that manipulate how charge carriers behave in a device. As the dimensions of these devices are reduced to the nanoscale, surfaces and interfaces play a larger role in the behavior of carriers in devices and must be thoroughly investigated to understand not only the material properties but how these materials interact. Separating the effects of these different building blocks is a challenge, as most testing methods measure the performance of the whole device.

Semiconductor nanowires represent an excellent test system to explore the limits of size and novel device structures. The behavior of charge carriers in semiconductor nanowire devices under operational conditions is investigated using local probing technique electron beam induced current (EBIC). The behavior of locally excited carriers are driven by the forces of drift, from electric fields within a device at junctions, surfaces, contacts and, applied voltage bias, and diffusion. This thesis presents the results of directly measuring these effects spatially with nanometer resolution, using EBIC in Ge, Si, and complex heterostructure GaAs/AlGaAs nanowire devices.

Advancements to the EBIC technique, have pushed the resolution from tens of nanometers down to 1 to 2 nanometers. Depth profiling and tuning of the interaction volume allows for the separating the signal originating from the surface and the interior of the nanowire. Radial junctions and variations in bands can now be analyzed including core/shell hetero-structures. This local carrier probing reveals a number of surprising behaviors. Most notably, directly imaging the evolution of surface traps filling with electrons causes bandbending at the surface of Ge nanowires that leads to an enhancement in the charge separation of electrons and holes, and enabling the extraction of different characteristic lengths from GaAs and AlGaAs in core/shell nanowires.

For new and emerging solid state materials, understanding charge carrier dynamics is crucial to designing functional devices. Presented here are examples of the wide applicability of EBIC and its variants, through imaging domains in ferroelectric materials, local electric fields and defects in 2D semiconductor material MoS_2 , and gradients in doping profiles of solar cells. Measuring the local behavior of carrier dynamics, EBIC has the potential to be a key metrology technique in correlative microscopy, enabling a deeper understanding of materials and how they interact within devices.

Chapter 1: Introduction

When we think about how modern society functions, one of the first things that comes to mind are the electronic devices, smart phones, tablets and computers, that connect us to each other, allow us to communicate and organize, and drive our economies. Each of these contain billions of solid-state devices that make up the semiconductor chips, displays, light emitting diodes, and sensors.

We will rely increasingly on technologies based on solid-state devices, solar cells to generate renewable energy, power electronics to distribute that energy, solid state lasers to enable communication over fiber optics, light emitting diodes to light our homes and cities. These enabling technologies at the most fundamental level rely on the physics of solid state devices. The basic building blocks of these devices come from the material properties of their crystal structures.

To go from the basic properties of materials to how we make devices we have to consider how to change the behavior of semiconductors and manipulate their conduction, energy gaps and fields. Doping, adding impurities to the crystal lattice to either donate an electron or accept an electron, is one of the most fundamental methods of changing the behavior of semiconductors and building devices allowing us to tune properties of the semiconductor and change its conduction and energy levels. Junctions between semiconductors that are doped differently or have different compositions, insulators, and metals allow us to design and build devices. A homo-junction is the simplest type of device and consists of a junction between a

p-type and n-type semiconductor.

Hetero-junctions are formed when taking two semiconductors with different compositions and putting them in contact with each other. Hetero-junctions are the core of many semiconductor devices particularly opto-electronics, LEDs and room temperature solid state lasers where they are used to form quantum wells and form super-lattices.

Metal semiconductor junctions can either form an energy barrier and can be used to make a diode, or have no barrier or a tunneling contact where we can make an ohmic contact to a material.

Finally the most important junction that has been most widely used is the metal-insulator-semiconductor junction, which is the foundation of the metal oxide semiconductor field effect transistor. The most famous of which is the SiO_x-Si interface that is used throughout the integrated circuit industry and how Silicon Valley got its name.

Conceptually, these building blocks are easy enough to understand and are predictable in the simple picture of putting these materials together. However, many of the assumptions that guide the design of these devices break down at the interfaces between materials and surfaces where the assumption of an infinite periodic structure is no longer valid. At these interfaces there can be dangling bonds that have states that lie within the band gap of the material and are a source of traps, places where charge is trapped and can be a source or sink of carriers.

Crystalline defects present another challenge to our assumptions, since they can locally contain far more charge than the surrounding material and its doping level.

At these defects we cannot assume the same paths of conduction for carriers. Electrically active defects have discrete energy states that sit in a quantum well, many of which reside in the band gap resulting in complex behavior that is hard to predict.

With the size of devices getting smaller, the thickness of layers is also getting much thinner, approaching only a few mono-layers of material. The devices are not limited to being fabricated in 2D layers: with the invention of the FinFET, most current integrated digital semiconductor chips are fabricated in 3D structures.

As we explore the limits of finite dimensions of solid state devices, these interfaces, surfaces and defects play a dominant role in device performance as the number of states can greatly exceed the doping levels of the material. We need an imaging technique that can separate the response of junctions and interfaces spatially and operate on a functioning device, and be able to characterize the effects they have on internal electric fields and the operation of the device. We need a functional imaging technique that can probe subsurface effects with nanometer scale resolution. If our goal is to probe both surfaces and the internal structure of nano-scale devices, we must use a method of locally exciting carriers. The electron beam of a scanning electron microscope (SEM) provides the local probe that meets these criteria.

1.1 Thesis Synopsis

To understand the internal fields and dynamics of carriers and the effects of interfaces we electrically contact the device and measure the electron beam induced current (EBIC). Measuring the EBIC signal, we can directly image junctions in a material and depletion regions. Outside the depletion region, we can extract the

diffusion of minority carriers, electrons in a p-type doped material and holes in a n-type doped material. Chapter 2 is an introduction to solid state devices. Chapter 3 provides an introduction a detailed explanation of EBIC and what can be learned with different devices.

To understand the effects of reduced dimensions and spatially confined structures we examine a number of test systems based on nanowires to look at the effects of different operating conditions and see how the response of the semiconductor nanowire changes. We examine three different device structures: germanium metal-semiconductor-metal (MSM) nanowires with Schottky contacts, GaAs/AlGaAs radial heterostructures with ohmic contacts, and silicon nanowire metal-insulator-semiconductor devices.

In the germanium nanowire MSM device, we explore the evolution of response as we increase an applied bias and fully deplete the channel. After sufficient external bias is applied and the channel is fully depleted, we study the effects of gating and higher bias to understand the onset of pre-breakdown behavior in structures that have limited dimensions. In bulk devices these effects extend over a larger area and the concentration of carriers is different. We detected a permanent change in the nanowires that we attribute to impact ionization damage that was still present at reverse polarity and lower voltages.

Radial structures in nanowires present a great challenge in characterization. There have been a number of proposed devices with radial structures that allow for quick separation of carriers particularly in optoelectronic devices such as solar cells. The GaAs/AlGaAs structure nanowire gives us the opportunity to study a sam-

ple that not only has a complex geometry but also has a Type I heterostructure with the AlGaAs having a different bandgap and mobilities for carriers than the GaAs. The challenge with this type of sample is how to know where the signal is coming from and which carriers are you measuring. We utilize electron flight simulations with the geometry of the nanowire to produce simulated radial profiles of where the carriers are being created and use this to extract am-bipolar drift-diffusion lengths for both the outer shell material AlGaAs and the core material GaAs.

The last type of interface we explore is a silicon nanowire device that has a radial metal insulator semiconductor MIS junction. Like the radial PN junction this structure can also lead to a quick extraction of carriers before they can recombine. The doping level is key to understanding the extent of where the depletion region will form. It is vital then to have a known doping concentration. This is a challenge in using nanowires grown using the vapor-liquid-solid growth technique. To simplify this we produce wire using a known doping concentration by etching them from a Si wafer using the metal assisted chemical etching (MACE).

Nanowires and other structures produced using the MACE technique can have a very clean interface and very deep structures, not accessible with other techniques. The fabrication and design of MIS nanowires test structures is detailed in Chapter 4. The EBIC analysis of Si MIS nanowires is detailed in Chapter 8, where we discuss effects of band-bending and carrier inversion on nanowire structures of reduced dimension and carrier inversion.

To explore these systems with the resolution to examine the interfaces and confined dimensions we had to push the limits of detection beyond what was possible

with current methods. We had to increase the spatial resolution, detection level, dynamic range and signal to noise ratio.

With these advances we were able to extend the use of this technique to applications not previously accessible. In Chapter 9, we will explore using electron beam absorbed current (EBAC) we are able to image domains in bismuth ferrite BFO and PZT, which are correlated with results from piezo force microscopy (PFM) measurements, even though the signal between domains was less than 500 fA. With 2D electronic materials MoS_2 we are able to provide bias and image folding of layers even though the interaction volume is significantly smaller than any other material system we have used. In traditional Si solar cells we have imaged not only the P-N junction, but we also detected smaller variations that reveal the effects of dopants counteracting each other in the graded doping profile.

Chapter 2: From Band theory to Devices

The importance of semiconductors, in realizing the applications and devices, is the ability to change their behavior through altering their energy states and behavior of charges inside them. Semiconductors have the ability to interact with light absorbing energy and emitting it in the visible spectrum. This allows to make light, LEDs and lasers, and electricity, solar cells and thermo-electrics, in the most efficient way possible.

In this chapter we explore the origin of processes taking place in semiconductor materials devices and the basic building blocks that allow us to make devices. Understanding these fundamentals will allow us to interpret the results and effects we show in Chapters 5, 6, and 7.

2.1 Band Theory

The periodic structure of the crystal lattice and the behavior of electrons in that structure allow us to predict whether a material is a metal, insulator, or semiconductor. The theorem most applicable to understanding semiconductors that allows us to predict their optical and electronic properties is the Bloch theorem, which describes the behavior of electrons as a wave in a periodic potential due to the arrangement of atoms in a crystal in k space (Fourier space).

The Kronig-Penney model treats electrons in a one dimensional case that considers the behavior of electrons in a periodic potential U_0 allowing us to calculate the energy of electrons as a function of k . Once we can establish the relationship

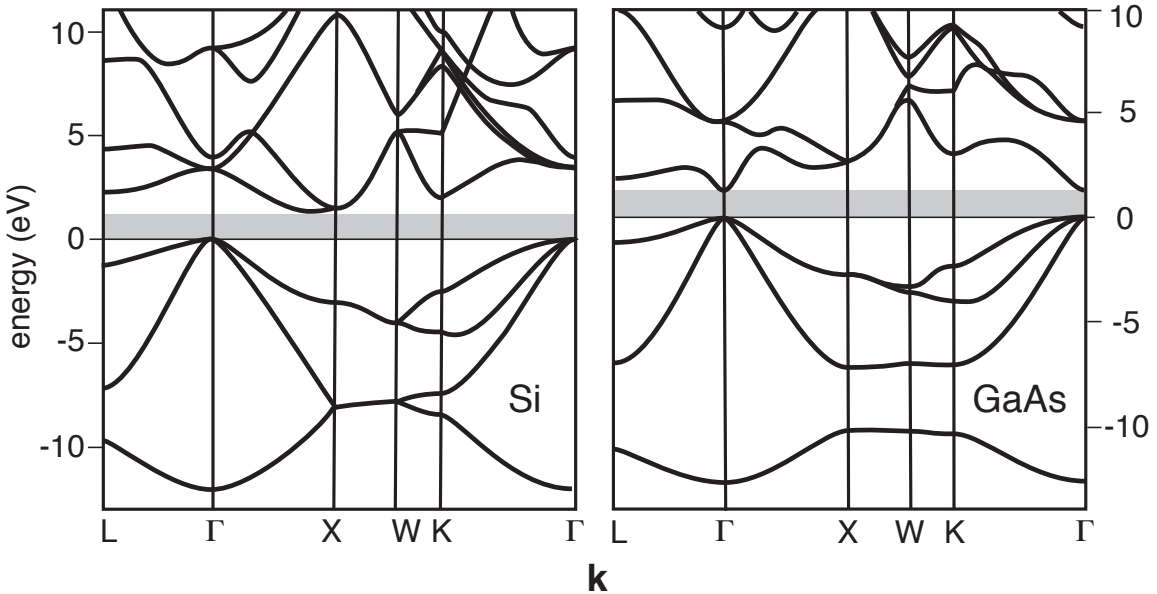


Figure 2.1: Band structure (a)Si, (b) GaAs. Bandgap shown in grey, adapted from¹

between energy E and momentum k we can treat electrons as free using Newton's equations with momentum and an effective mass. This approximation makes it easier to design devices with the desired properties, selecting the effective mass at energy minima in the conduction band for electrons and the energy maxima in the valence band for holes. These two points determine the band gap. Using the effective mass we can predict the force E -fields exert on electrons as they move through a material.

2.2 Doping and the Fermi level

The Fermi level for an intrinsic semiconductor lies in the middle of the band gap. It defines the point where half of the states will be filled above and below. It can be obtained by realting Eq. 2.1 and 2.2.

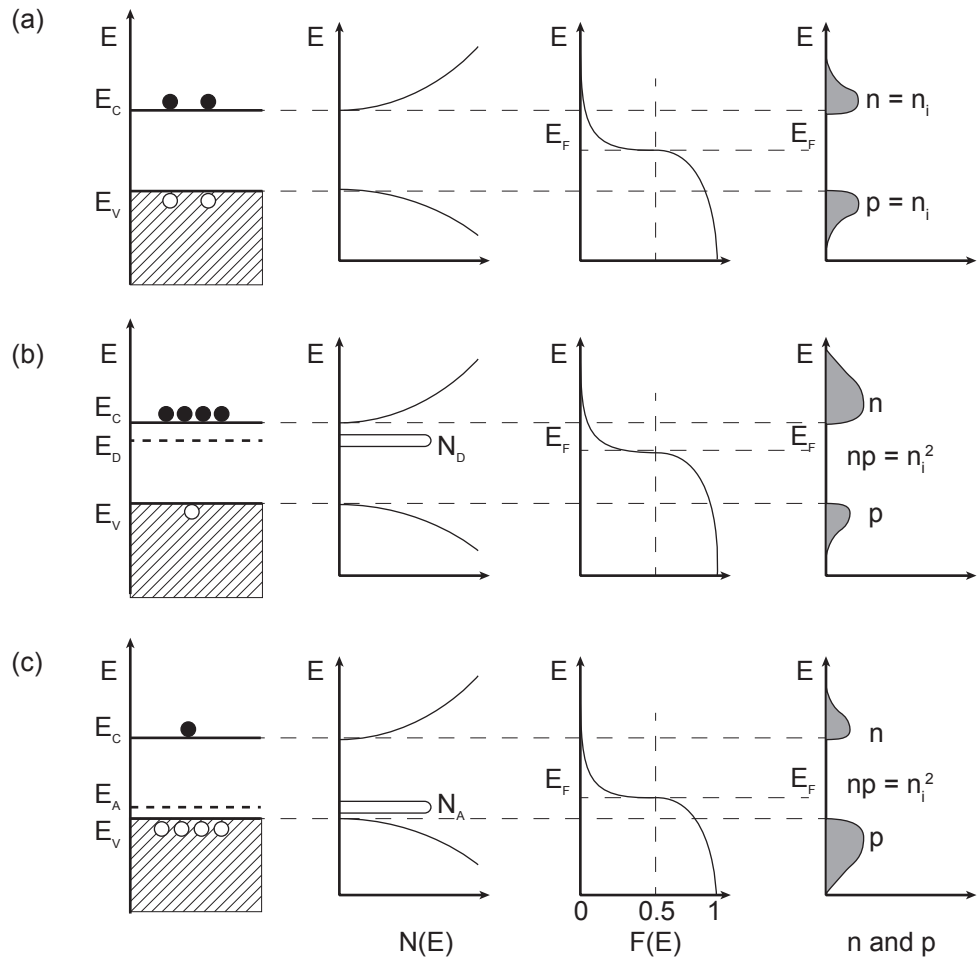


Figure 2.2: Schematic band diagram, density of states, Fermi Dirac distribution, and carrier concentration for (a) intrinsic, (b) n type, and (c) p-type semiconductors at thermal equilibrium. Adapted from².

$$n = N_C \exp\left(-\frac{E_C - E_F}{kT}\right) \quad (2.1)$$

$$p = N_V \exp\left(-\frac{E_F - E_V}{kT}\right) \quad (2.2)$$

The Fermi level E_F will shift towards the conduction band for n-type or valence band p-type doping, (Fig. 2.2). As with the intrinsic semiconductor, the Fermi level in extrinsic semiconductors is the point where the states have a probability of being half filled, accounting for why it shifts towards the conduction band or valence band depending on the doping type. At thermal equilibrium the Fermi level in each of the p-type portion and the n-type portion allows us to predict the built in potential of the junction. In junctions the Fermi level will remain constant across the device in thermal equilibrium, and under bias or excitation we have quasi Fermi levels for each type of carrier. At equilibrium the number of carriers in a device will be governed by the intrinsic level with the following relationship

$$n_i^2 = p * n \quad (2.3)$$

The total number of carriers will both n and p will always be equal to the number of intrinsic carriers squared, as illustrated in Fig. 2.2 in the number of carriers for each type of doping. If $n * p$ is $> n_i^2$ in a region, than recombination processes will dominate. If $n * p$ is $< n_i^2$ in a region, than generation processes will dominate. This only happens when the device is out of equilibrium and is driven by an external source. For LEDs carriers are injected from the contacts and recombination is

the dominate process. For solar cells a depletion region means there are very few carriers and the level is less than n_i^2 , and generation processes dominate.

2.3 Transport Dynamics in Devices

The movement of carriers in semiconductors are primarily concerned with drift due to the force exerted on carrier, electron or hole, by an electric field and through diffusion of carriers from high concentration to a lower concentration. The drift velocity with the units of $\text{cm}^2/\text{V} - \text{s}$ is defined as

$$v_d = \mu E \quad (2.4)$$

Acoustic phonons and ionized impurities greatly affect the mobility of carriers in polar semiconductors Ge and Si through scattering events. This means it can be described by mean free time, which takes into account the effective mass of the carrier.

$$\mu_{n,p} = \frac{q\tau_m}{m^*} \quad (2.5)$$

For semiconductors the drift current taking into account the contribution of holes and electrons is defined as

$$J = q(\mu_n n + \mu_p p)E \quad (2.6)$$

Drift currents are present in devices with an applied electric field that is external and from built in potentials such as the PN junction discussed in section 2.4.1 and can be caused by the local injection of carriers .

The other key component that must be discussed in probing the local electrical properties is diffusion of carriers. When locally there is a higher concentration of electrons, the flux is governed by Fick's law

$$\frac{d\Delta n}{dt}|_x = -D_n \frac{d\Delta n}{dx} \quad (2.7)$$

and holes

$$\frac{d\Delta p}{dt}|_x = D_p \frac{d\Delta p}{dx}. \quad (2.8)$$

The current due to this flux for electrons is

$$J_n = qD_n \frac{d\Delta n}{dx} \quad (2.9)$$

and holes

$$J_p = -qD_p \frac{d\Delta p}{dx}. \quad (2.10)$$

The relationship between the diffusion coefficient and mobility is from the Einstein relation, by setting the drift component to equal the diffusion component in a semiconductor without an external field, but with nonuniform doping.

The Einstein relation for electrons and holes is given by

$$D_n = \left(\frac{kT}{q} \right) \mu_n \quad (2.11)$$

$$D_p = \left(\frac{kT}{q} \right) \mu_p \quad (2.12)$$

Finally, another important parameter and metric is the diffusion length defined as

$$L_d = \sqrt{D\tau}. \quad (2.13)$$

2.3.1 Recombination and Generation

The net difference between recombination and generation rates is how we can measure the local changes in semiconductors and allow us to map the separation of charge. This local difference is what drives the observable current. The recombination rate is directly related to the light that can be collected in cathodeluminescence.

2.3.2 Current Density Equations

At steady state conditions taking both the drift and diffusion components to current for electrons and holes we have

$$J_n = q\mu_n n E + qD_n \nabla n \quad (2.14)$$

$$J_p = q\mu_p p E - qD_p \nabla p. \quad (2.15)$$

2.3.3 Continuity Equations

For time dependent relations, the continuity equations from electrons and holes are needed to account for low level injection, generation and recombination and the

current flowing into and out of a region. The source of the generation rates G_n and G_p are caused from external influences: light, impact ionization, and in the case of our interests the local carriers generated by an electron beam. These are given by

$$\frac{\partial n}{\partial t} = G_n - U_n + \frac{1}{q} \nabla \cdot J_n \quad (2.16)$$

$$\frac{\partial p}{\partial t} = G_p - U_p - \frac{1}{q} \nabla \cdot J_p \quad (2.17)$$

For the one dimensional case and low level injection condition, which is the condition that we are operating under in the experiments described in this thesis, Equations 2.16, 2.17 reduce to

$$\frac{\partial n_p}{\partial t} = G_n - \frac{n_p - n_{p0}}{\tau_n} + n_p \mu_n \frac{\partial E}{\partial x} + \mu_n E \frac{\partial n_p}{\partial x} + D_n \frac{\partial^2 n_p}{\partial x^2} \quad (2.18)$$

$$\frac{\partial p_n}{\partial t} = G_p - \frac{p_n - p_{n0}}{\tau_p} - p_n \mu_p \frac{\partial E}{\partial x} - \mu_p E \frac{\partial p_n}{\partial x} + D_n \frac{\partial^2 p_n}{\partial x^2}. \quad (2.19)$$

For clarity n_p denotes electrons as the minority carriers in a p-type material, and p_n are holes in n type material. These equations 2.18, 2.19 and the boundary conditions of the specific device are what govern the EBIC response that we observe. This is how EBIC is sensitive to the electric fields and carrier dynamics inside a device. This relationship allows for EBIC to image depletion regions and diffusion lengths of minority carriers. In subsequent chapters we make assumptions that are device specific to interpret the EBIC response.

2.4 Device Building Blocks

Making semiconductors into devices involves controlling the behavior of charge carriers inside the material. This is done through controlling the number of carriers, the fields within a device by making junctions, and energy bands. Manipulating these variables we can make certain processes dominant in a device to realize different effects. The devices studied in Chapters 5, 6, and 7 all have aspects of these basic building blocks.

2.4.1 PN Junction

The PN junction forms the basis of most semiconductor devices and the physics of how we understand them. This junction is solely controlled through doping of the materials by adding impurities that have levels close to the valence band in the case of p-type doping that accept an electron, or close to the conduction band by donating an electron to the lattice. The E-field that forms at the PN junction is the simplest to understand in terms of behavior and serves as an excellent example when considering local probing techniques.

At the junction, the donor and acceptor atoms are exposed and cause a space charge region or depletion region to form. The charge within the depletion region creates an electric field that separates electrons and holes. Integrating the electric field over the depletion region gives us the built-in potential ψ_{bi} . In the energy band diagram, the built-in potential determines the band bending in the depletion region of the PN junction. At thermal equilibrium, the Fermi level E_f remains constant throughout the device. The PN junction is the basis of all LEDs and most

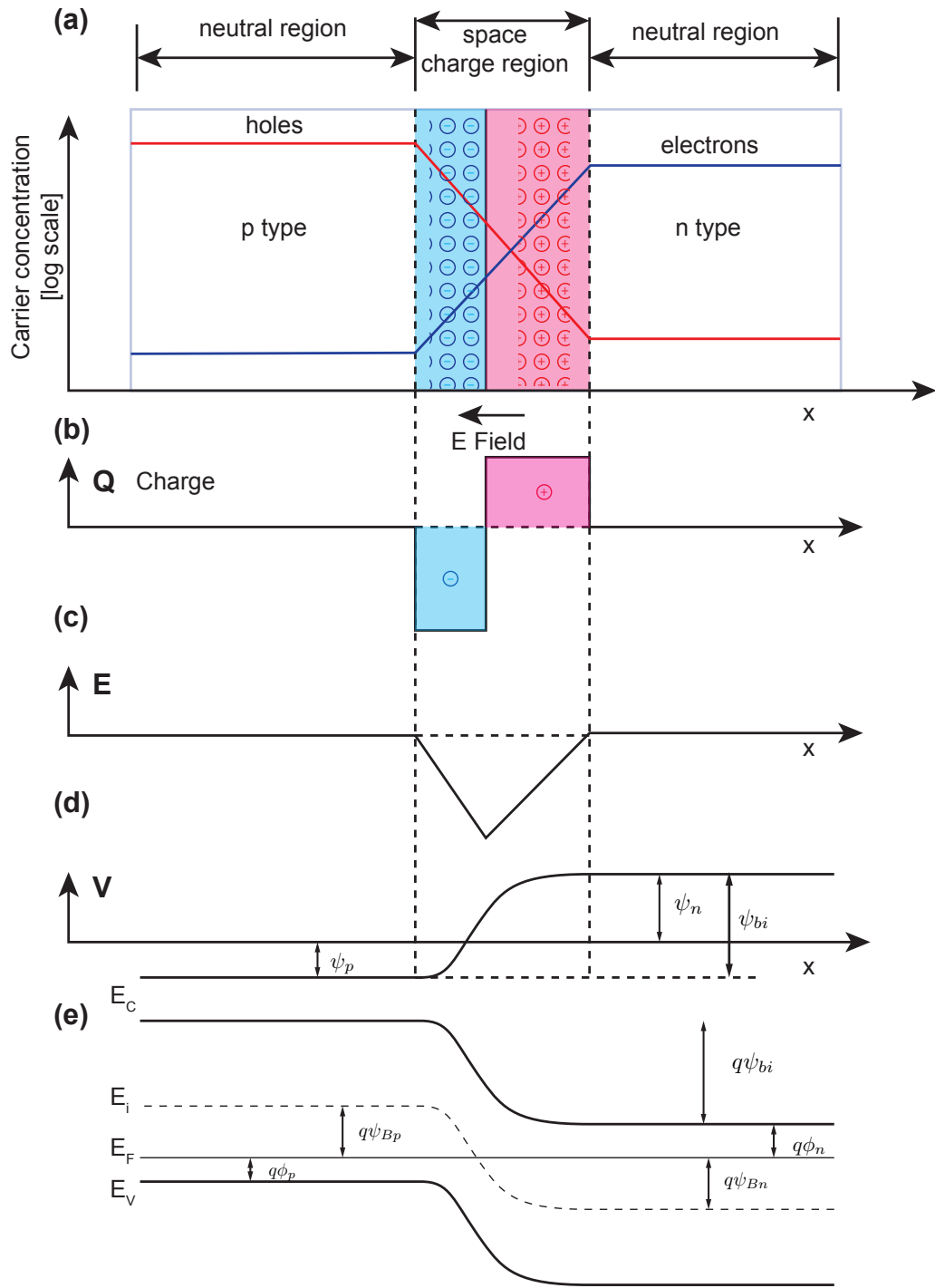


Figure 2.3: Schematic of an abrupt PN junction. (a) Carrier concentration for holes and electrons on either side of PN junction with p-type and n-type section and space charge region (b) Charge Q from donor and acceptor atoms (c) E field (d) Built in potential ψ_{bi} , integral of E field (e) Band diagram of abrupt junction with intrinsic, E_i and Fermi level E_f labeled.

photovoltaic devices. PN junctions are also found in all CMOS transistors.

2.4.2 Hetero-Junctions

The interface between two materials with different band gaps is a hetero-junction. In type I hetero-junctions the band gap of one material lies within the band gap of the other. The junction represents an important building block that can be used to engineer bands within a material. The band engineering can be used to create quantum wells inside a material these have wide applications in LEDs Solar cells and room temperature lasers.

In heterojunctions as with PN junctions the bending of the bands happens at the interface. When different doping regions are brought together in contact Fermi levels become aligned. In Chapter 6, a radial hetero-junction of AlGaAs and GaAs in nanowires is studied in detail.

2.4.3 Metal Semiconductor Contacts

Metal semi conductor contacts can be rectifying as with the case of a PN junction. The junction is the result of difference of electron affinity and the vacuum level. Materials can be blocking to one type carrier. As with the PN junction, the Fermi levels of the semiconductor and the metal align. Shown in Fig. 2.4 is a, diagrams how built in potential ψ_{Bn0} at the MS contact forms due to a difference of the work function of the metal ϕ_m and the electron affinity of semiconductor χ . The barrier at a MS contact can be enhanced by adding a thin insulator.

The energy band diagram of a MS contact, without a barrier enhancement layer, for n-type and p-type is shown in Fig. 2.5. The barrier at a MS contact is can be

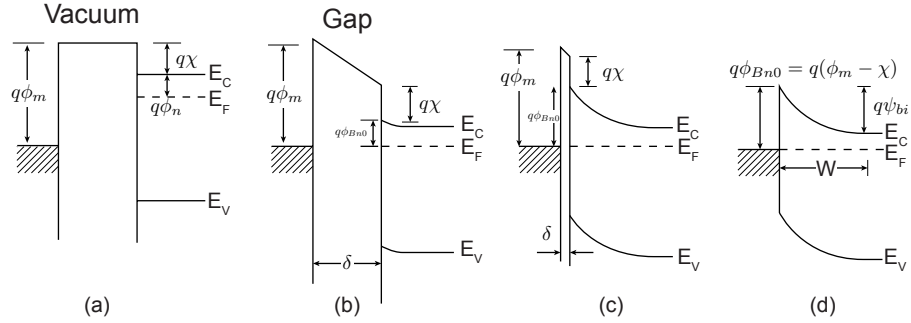


Figure 2.4: Energy band diagram of metal-semiconductor contacts. (a) shows metal and semiconductor with respect to vacuum level and the work function and electron affinity(b) connected system with a gap and Fermi levels lining up (c) gap is reduced with enhanced barrier (d) No gap is present. Adapted from².

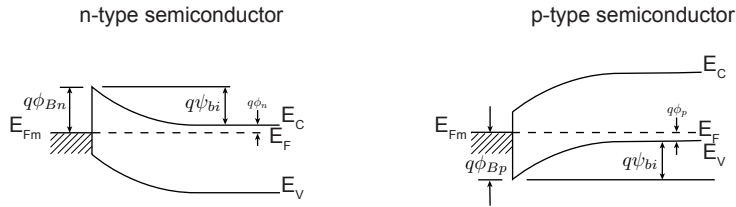


Figure 2.5: Energy band diagram for metal semiconductor junction at thermal equilibrium for (a) n-type , (b) p-type semiconductors.Adapted from².

blocking to either electrons or holes. The MS contact in a Schottky diode is one of the easiest methods of determining the diffusion lengths of minority carriers in a material.

2.4.4 Metal Insulator Semiconductor

The metal-insulator-semiconductor interface allows for one of the important semiconductor devices by the number the CMOS transistor. Applying a voltage on the metal (Fig.2.6 can change the band-bending at the surface semiconductor this works for both p-type and n-type semiconductors. In accumulation mode the bands shift for greater concentrations of the majority carrier with a negative voltage ap-

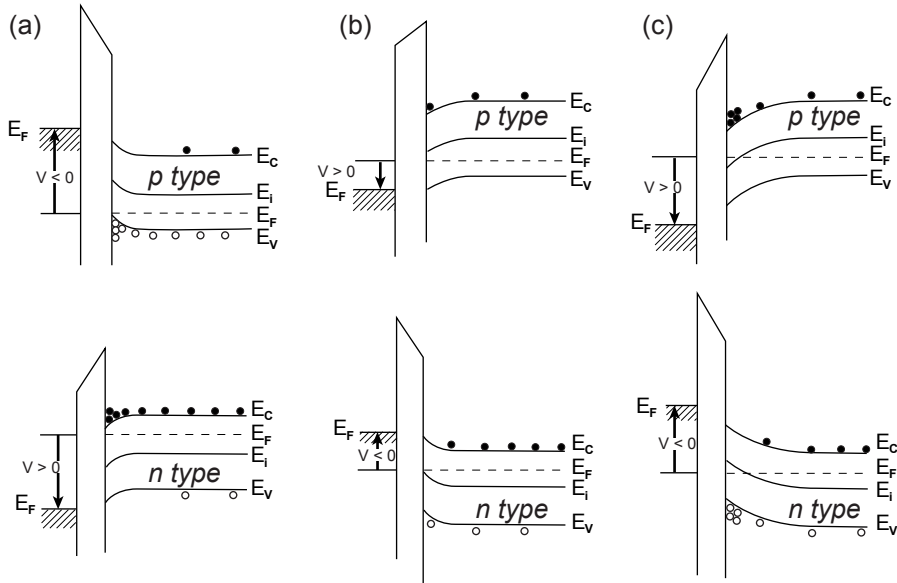


Figure 2.6: Energy band diagram for MIS junction for p-type (top) and n-type (bottom) in (a) Accumulation mode (b) Depletion mode (c) Inversion mode. Adapted from².

plied for p-type and positive voltage for n-type semiconductors. For p-type semiconductors applying a positive voltage will reduce the number of carriers in depletion mode if the voltage applied is great enough an inversion layer forms at the surface where a n-type layer is induced; the reverse is true for n-type materials.

The ability to change carrier type by applying a potential across this interface is the fundamental operating principle of all transistors and allows us to further modify and explore properties of material systems.

2.4.5 Defects and Interfaces

The periodic structure allows us to make the approximations that make designing devices possible. The assumption of a periodic structure does not apply to interfaces and defects. At these locations there can be states that exist inside the band gap that lead to different types of behavior that effect the performance of the device. The

energy states from defects and interfaces, also known as traps, can be the source of recombination and generation, processes that are explored further in Chapter 7 and have a major impact on how a device behaves. Understanding the role of these states and how they effect device performance is one of the main challenges in making devices. Characterizing these trap states and their electronic properties is a challenge and is one of the main uses of EBIC.

2.5 Summary

The basic building blocks of solid state devices primarily alter carrier dynamics, shifting populations of carriers in the valence and conduction bands, forming junctions, barriers and, E fields that drive carriers. The processes of carrier diffusion, drift, generation, and recombination determine the behavior of the device and how it interacts with external stimulus from interacting with light and applied voltage biases.

To understand the behavior of carriers inside of these devices we need to have a basic understanding of the mechanisms that control them. As devices are constructed from the interfaces between materials and modifications such as doping, the fabrication and processing of materials have a dramatic effect on the behavior of devices. Devices are made of multiple building blocks that we have introduce in this Chapter. To be able to study the effects of each of these, it is important to be able to spatially characterize the interfaces. In the next Chapter we discuss how the materials are processed and fabricated into devices. For the remainder of this Thesis we explore electron beam induced current (EBIC) as a technique to locally probe carrier dynamics and understand the origin of the observed effects and behavior of

carriers that impact the performance of a device.

Chapter 3: Introduction to EBIC

Electron beams generate electron-hole pairs in semiconductors in a spatially limited generation volume dependent on the incident energy of the beam and the scattering inside of the material. These electron-hole pairs can either recombine and release energy, radiative or non-radiatively, or they can result in current following through the material.

In devices these electron-hole pairs, can help measure semiconductor device parameters such as diffusion lengths of minority carriers, relaxation times, and image the extent of depletion regions. They are highly sensitive to local differences in E-fields in a material and are excellent at characterizing crystalline defects which can locally alter recombination rates. Since the technique was popularized in the early 1980's⁵, EBIC has been used to characterize a wide range of semiconductor materials and devices.

3.1 Signals from Primary E-beam

When the electron beam impinges on a semiconductor material it releases a substantial amount of energy. This can release characteristic X-rays that tell about the composition of the material. Light is emitted in the form of cathode luminescence when excited electron-hole pairs recombine. Backscatter electrons scatter off of the nucleus of the atom in the form of backscatter electrons. Secondary electrons are electrons excited in the materials that have enough energy to become released and travel freely in vacuum. Electron hole pairs inside the material that

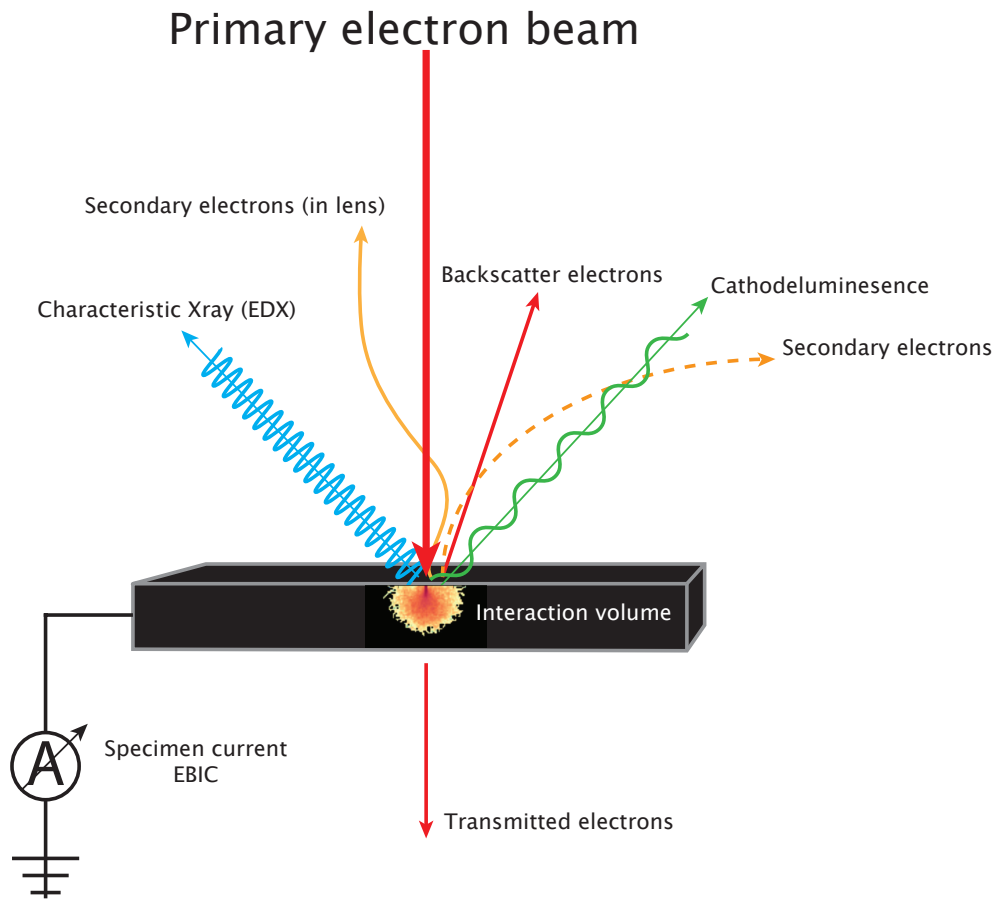


Figure 3.1: Electron beam interaction with sample and signal types.

do not recombine can be measured as a collected current. With a powerful enough beam and electron transparent sample that is sufficiently thin ($\approx 200\text{nm}$) transmitted electrons and elastically and inelastically electrons can also be measured. An excellent review on the physics behind these different imaging techniques can be found here⁶.

3.2 Probing of Semiconductors

Locally a high number of electron hole pairs are generated in a small volume. Typically the carrier concentration of Δp and Δn is determined by the generation rate,

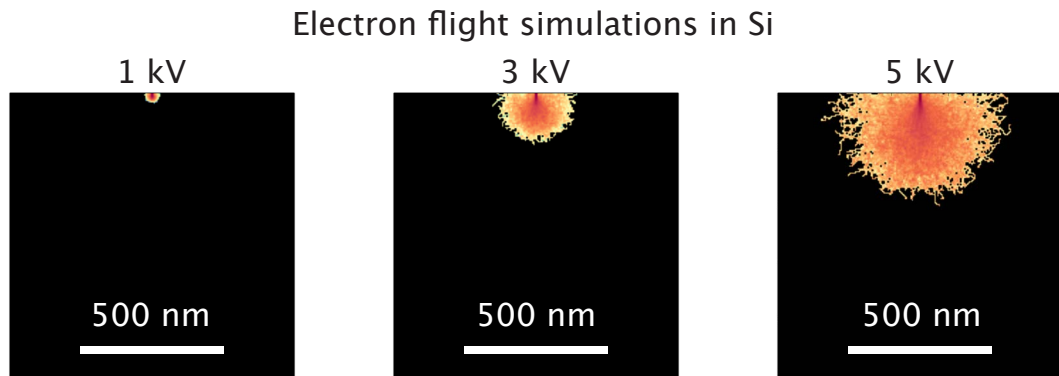


Figure 3.2: Monte Carlo simulation of interaction volume of electron beam with Si sample with (a) 1kV (b) 3kV, and (c) 5kV electron energy. Scale bar is 500nm. Color represents energy released and is normalized to a logarithmic scale.

Eq. 3.1 and the recombination rate Eq. 3.2 and the interaction volume. The interaction volume is usually described as a tear drop shape that is dependent on the atomic number (Z) contrast, atomic weight of the material, its density and the energy of the incident electron beam⁷.

To get a finer detail of this interaction volume, Monte Carlo simulations of electron flight path and scattering events⁸ can provide a more quantitative understanding of the nature of EBIC and CL contrast⁹. Estimating the number of carriers generated in a volume can be calculated by taking the energy dispersed and dividing it by $3E_g$

$$G = \frac{E - E_{th}}{E_i}. \quad (3.1)$$

The recombination rate for electrons and holes under low injection conditions

where $n * p < n_i^2$ is

$$U_n = \frac{\Delta n}{\tau_n}, U_p = \frac{\Delta p}{\tau_p} \quad (3.2)$$

The carrier lifetimes of minority carriers is given by

$$\tau_n = \frac{1}{\sigma_n v_{th} N_t}, \tau_p = \frac{1}{\sigma_p v_{th} N_t} \quad (3.3)$$

where N_t is the trap density.

The number of carriers generated in the interaction volume combined with the geometry of the sample is used extensively in Chapters 6 and 7 to generate simulated radial profiles across nanowires. The recombination rate is governed by the minority carrier lifetimes. These lifetimes can be measured directly by time resolved cathode-luminescence or indirectly through the Einstein relation and measuring their diffusion lengths.

3.2.1 Junctions

Depletion regions are readily imaged by EBIC due to efficient carrier collection and separation of generated electron hole pairs. On either side of a P-N junction the minority carrier diffusion lengths can be directly measured^{10;11}. The lifetime of minority carriers can be directly determined¹². For Schottky junctions the minority carrier diffusion lengths and the depletion region can be measured¹³.

Depth profiling of junctions can be achieved by varying the incident electron energy, producing a deeper interaction volume^{14;15}. The dopant profile of the junction can be confirmed with using SIMS¹⁶.

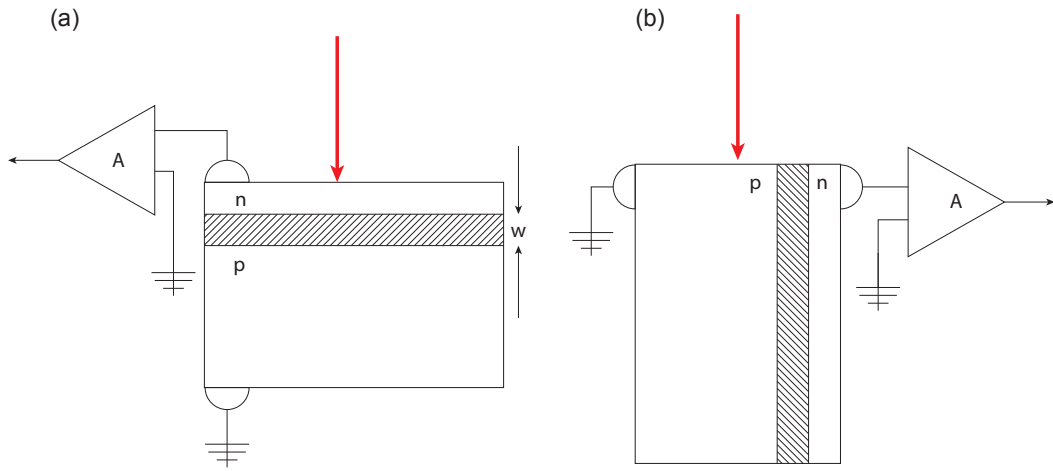


Figure 3.3: EBIC schematic of PN junctions. Signal amplifier(shown as an op-amp) provides a virtual ground to the n type contact and the p-type contact is grounded. This allows for two conduction paths to ground and a for carriers to be separated by the built in E-field. (a) Planar EBIC measurement of a buried junction Varying the incident beam energy denoted by the red arrows changes the depth profile. (b) Cross-section of PN junction orthogonal to the imaging plane. Minority carrier diffusion lengths can be directly measure on either side of the junction, as well as the extent of the depletion region.

3.2.2 Defects

The study of defects and their properties is one of the widest used applications of EBIC. At crystalline defects, there are several factors that can cause contrast in charge collection. For a detailed explanation of the scope of what can be measured of the electrical properties of crystalline defects, please refer to D.B. Holt¹⁷ for a definitive guide on CL and EBIC. These sites can have states that exist in the middle of the band gap and can be a site of both recombination and generation. If the defect is charged it can locally bend bands around it this can lead to either a greater recombination or generation. This can be seen in grain boundaries in multi crystalline Si^{18;19} and polycrystalline Si²⁰.

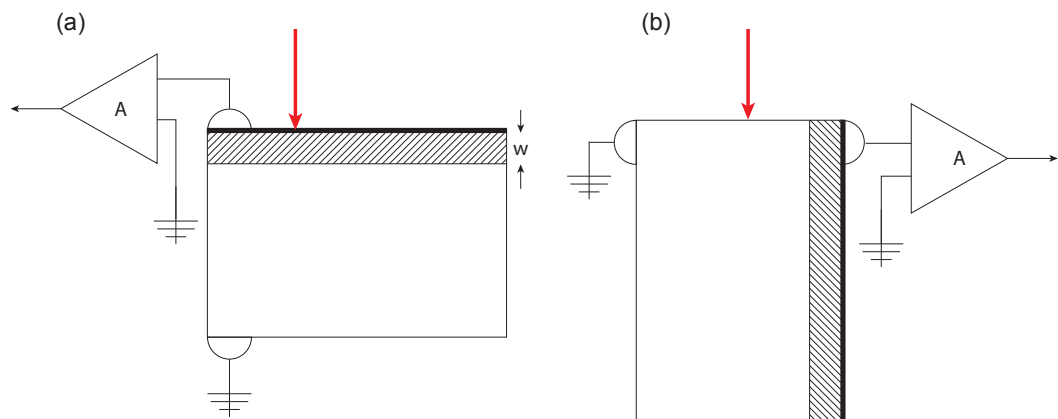


Figure 3.4: EBIC schematic of Schottky junctions. Signal amplifier(shown as an op-amp) provides a virtual ground to the contact forming the junction and the other ohmic contact with no barrier is grounded. This allows for two conduction paths to ground and a for carriers to be separated by the built in E-field. (a) Planar EBIC measurement of a buried junctions and can show a net difference in current if defects are located within the depletion region and local have a high recombination rate. (b) Cross-section of Schottky junction orthogonal to the imaging plane. Minority carrier diffusion lengths can be directly measure on one side of the junction, as well as the extent of the depletion region.

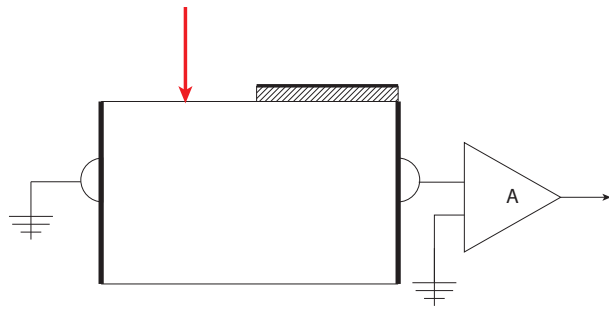


Figure 3.5: EBIC schematic for MSM devices, where there is a blocking contact on either side of the device. This schematic can also work for EBAC where there is only one conduction path to ground and defects can be imaged outside of any depletion region.

To aid in the contrast and detection limit, samples are made with a thin Au coating to create a Schottky junction that can increase the collection efficiency. Defects appear as a site of recombination with dark contrast when compared to the surrounding signal from the junction.

3.2.3 Electron Beam Absorbed Current

Most EBIC measurements are conducted with two contacts: one going to ground and the other going to a transimpedance amplifier that acts as a virtual ground. In this configuration the electrons and holes can be efficiently separated. If there is only one contact to the transimpedance amplifier, electron beam absorbed current (EBAC), carrier separation is not being measured, but instead the local differences between generation and recombination rates. The transimpedance amplifier will source or sink current to maintain charge neutrality. This is of interest because defects can be imaged outside of depletion regions without modifying the sample, Chapter 9.

EBAC has mainly been used by industry for fault analysis of conductive lines in

semiconductor integrated circuits²¹⁻²³. We greatly expand the capabilities of EBAC going beyond current uses, imaging domains in ferroelectric materials, where EBAC can be highly sensitive to the anisotropy in crystal structures.

3.3 Nano-structured Devices

For devices based on semiconductor nanowires, EBIC presents a challenge in that the surface to volume ratio is large enough that surface states and recombination play dominant role in the lifetime of carriers. This reduces the current signal drastically, such that it becomes a challenge to excite nanowires in a low injection condition where $\Delta n \Delta p <$ majority carrier concentration. To compensate for the low signal, lock-in amplifiers, which can recover a signal from a noise floor, have been used while using a lower beam current²⁴.

Lock-in techniques do have other benefits in collecting the signal as they can measure the phase and amplitude of a signal instead of the magnitude. Noise from the SEM and system ground in the form of a 60 Hz signal from the power lines is one of the biggest challenges.

In typical EBIC measurements where there is substantial gain from the incident beam interacting with a built-in field, there is no need for shielded wires for collecting the signal. When measuring signals on the order of tens to a few pA this is no longer adequate. Shielding the signal path is critical to measuring these signals. With proper shielding, lock-in techniques are not needed as there is sufficient signal to noise ratio.

3.3.1 EBIC on nanowire devices

EBIC has been used to characterize nanowire devices, but the results have been limited to the axial direction. Complex geometries that take into account the shape of interaction volume and distribution of carriers have not been carried out.

Axial junctions resulting from PN junctions and quantum dots grown inside the nanowire have been characterized using EBIC²⁵. Diffusion lengths of minority carriers were explored in Si nanowire Schottky diodes²⁴ where the authors estimated the value of the surface recombination velocity.

3.3.2 Simulated local probing

Due to the spatial confinement of carriers in the nanowire, some of the assumptions of a response due to excitation have to be questioned when Δn and Δp create their own local potentials. This was explored by³ in which the authors found a surprising result for ohmic devices where both diffusion and drift, from the local injection, both contribute to the observed current response. Devices with two Schottky contacts and Schottky diodes with one Schottky contact and one ohmic contact have a response that is expected to be dominated by minority carriers.

With a voltage bias applied, The response shifts and drift becomes a more dominant component in all types of devices. These simulation results provide a valuable basis to interpret an EBIC response.

3.4 Qualitative EBIC

Most EBIC results are qualitative in that they look at the relative signal difference and magnitude, whether it is dark or light contrast in comparison to the surround-

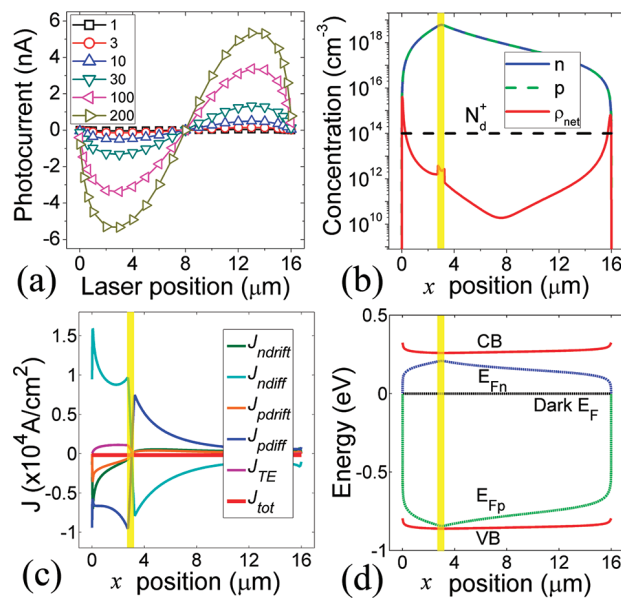


Figure 3.6: (a) Simulated zero-bias SPCM profiles of an N-type O-O device under different laser intensities as shown in the legend (units: kW/cm^2). (b) Distribution of ionized donor, electron, hole, and net charge densities, (c) current components distribution, and (d) band bending when laser (I laser = 200 kW/cm^2) is illuminating at x laser = 3 m, the position where the photocurrent peaks as shown in (a). The parameters used are $N_d = 10^{14} \text{ cm}^{-3}$, $\tau_p = \tau_n = 16 \text{ ns}$, laser spot size = 0.5 m. Note that a position-dependent carrier mobility has been considered due to intense laser illumination. Reprinted with permission from³. Copyright(2011) American Chemical Society.

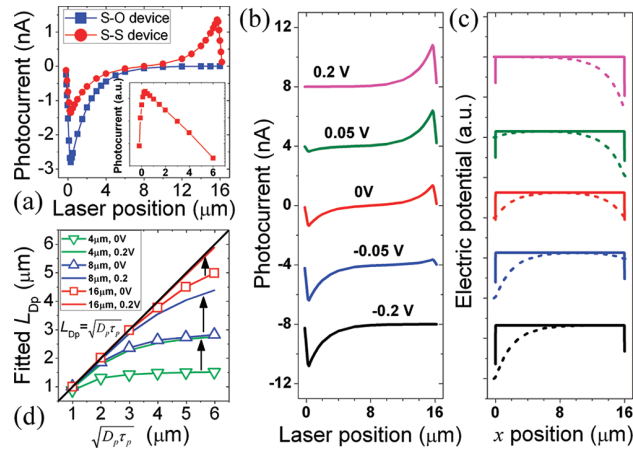


Figure 3.7: (a) Simulated zero-bias photocurrent profiles of an N-type S-S device under low level photoinjection. An S-O device is also shown for comparison. Inset shows the semilog plot of the S-S device SPCM. (b) Photocurrent of the S-S device under different bias. The right electrode is grounded. The SPCM profiles are offset by 4 nA each for clarity. (c) Electric potential profiles (in dark, solid lines) corresponding to different bias conditions shown in (b). Note the large band bending is limited within the depletion width in the left and right 50 nm only. Also shown for comparison is the line shape of integrating the photo-current in (b) over x (dashed lines). (d) Fitted minority diffusion length L_{Dp} compared with defined minority diffusion length $(D_p \tau_p)^{1/2}$ for three NW lengths (L_{NW}) and two different biases (V). The parameters used are same as those used in Figure 2 except the contact type. Reprinted with permission from³. Copyright(2011) American Chemical Society.

ing response. To collect the signal a spare imaging input from the SEM is used to collect the image from a preamplifier. The SEM however does not retain the magnitude of the signal; it just produces an image. The analog to digital converters (ADCs) in most SEMs are limited to 12 bits or 4096 signal levels, and often the data stored is reduced further to 8 bits. If there are DC offset currents from the sample or connections, a lower gain setting must be used and underlying information can be lost. Converting the observed signal to measured values is difficult as that information is usually lost when stored as an image format. In the typical configuration measuring both the secondary image and EBIC image at the same time are often not possible. Measuring both at the same time is critical for finding the edges of features to situate the EBIC signal against. It is possible to quantitatively measure diffusion lengths and depletion region widths using this method as the spatial information is intact.

3.5 Quantitative EBIC

To measure the signal levels we are seeking we need a wider dynamic range that can measure small currents and have a wide enough range to handle DC offsets. The internal scan generator that moves the position of the beam is also a limiting factor as the dwell has limitations. The ability to take many samples and average them before the beam moves position is important to recovering pA level signals. To accomplish these goals, a parallel effort was taken to develop a scan controller with high resolution ADCs and DACs and sample holder with appropriate levels of shielding with the capabilities to take these measurements. This work was done by Ephemerion Labs, Inc.(Philadelphia, PA).

Chapter 4: Fabrication of Nanowires and Devices

The nanowire devices studied in this thesis are fabricated using top down and bottom up approaches. The bottom up method uses a metallic catalyst on a Si/SiO_2 substrate where chemical precursors are decomposed on at the catalyst form a solution and the crystal grows as a precipitate when the solution becomes super saturated. This method is known as the VLS method (vapor liquid solid) and is the method used to produce the first nanowires²⁶. The second method is a top down fabrication approach where the nanowires are etched from a crystalline Si wafer²⁷. Both methods have advantages and make different types of structures possible.

The properties of the nanowire devices and all semiconductor devices are directly affected by the processes in which the materials are grown and the fabrication processing done to the devices. In this Chapter we highlight the methods that are relevant to the types of devices that measured in subsequent chapters.

4.1 Vapor Liquid Solid Growth

The VLS growth method has been used to fabricate numerous chemistries of nanowires from group IV elements Si and Ge the III/V compound semiconductors, GaAs and AlGaAs. The method is attractive for a number unique structures that would be very hard to fabricate in other modes. 2D quantum disks/dots have been grown in the middle of the nanowire by changing the precursors and growth conditions. Axial and radial junctions are possible with this growth mechanism²⁸.

Doping of the nanowire is also possible by adding in carrier gases with the

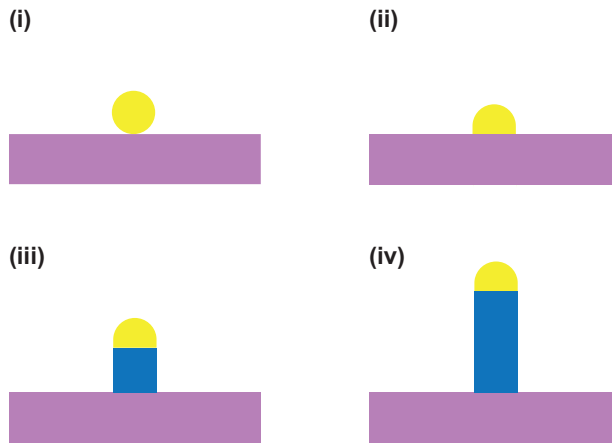


Figure 4.1: Vapor liquid solid growth of nanowires. (i) Substrate with catalyst gold colloid. (ii) Substrate is heated until colloid becomes liquid and forms a droplet on the surface. (iii) At the catalyst the precursor decomposes forming a solution of Ge and Au or Si and Au, this super saturates and the precipitate is a solid crystalline nanowire. (iv) Growth continues until the carrier gas stops and the nanowires are cooled leaving the catalyst at the end.

dopants during growth, although it has been hard to control the doping on the side walls of the material. For nanowire devices studied in this thesis, with the exception of the Si nanowires that were etched from a Si wafer, all of them are grown using the VLS method. The specifics of the growth conditions are explained in the relevant chapters.

4.2 MACE of Silicon Nanowires

Metal assisted chemical etching (MACE) of nanowires from a wafer has distinct advantages over growing nanowires. Silicon wafers have a known crystallographic orientation. The nanowires etched from the wafer all share the same orientation allowing for large arrays of nanowires with the same orientation. Defects in Si wafers are very low, and essentially can be thought of as defect-free. The wafers are of a known type and doping concentration. Fabricating nanowires from MACE process

allows for a direct comparison between the properties of nanowires of different size and geometry to devices and fabrication processes on the original wafer.

The MACE process has advantages over other etching processes, namely reactive ion etching. The main benefit is that it doesn't modify the surface of the material.

The MACE process uses a film of noble metal, a mixture of hydrogen peroxide, hydrofluoric acid and water to local oxidize the wafer in the presence of the metal and then the oxide is removed with hydrofluoric acid. This oxidation and etching of the oxide continues at fast etching rates until very long nanowires with high aspect ratios with no noticeable tapering occurring.

The noble metal, either silver or gold, is a source of positive carriers (holes) in the material. This promotes local oxidation in the presence of hydrogen peroxide. The peroxide does oxidize the other surfaces but at a much slower rate. Silver has a much higher etching rate than gold, but has some disadvantages in producing high quality structures. The main drawback is the silver becomes dissolved in the water or there are particles that become free of the film and can etch into the silicon on their own, creating porous structures. Porous silicon does have interesting properties with the interaction of light and large surface area and can be taken advantage of nanowires. Using the MACE process complex geometries and patterns have been fabricated out of both n-type and p-type silicon.

The etching direction is always in the $<100>$ direction even in $<111>$ wafers causing slanted nanowires and structures to be produced. This behavior makes sense as there is a greater number of bonds in the $<111>$ direction.

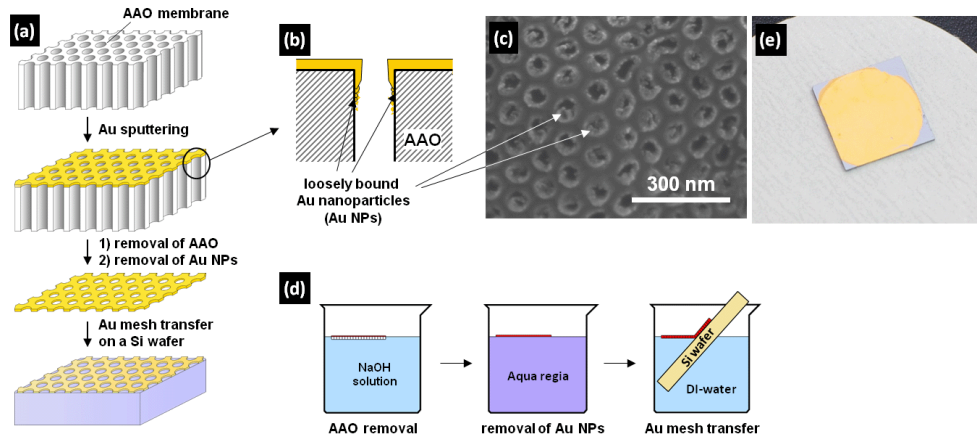


Figure 4.2: (a) A schematic procedure for the fabrication of gold mesh with arrays of nanoholes from anodic aluminum oxide (AAO) membrane. (b) A schematic cross-section of AAO after gold deposition, showing loosely bound gold nanoparticles (Au NPs) on the surface of pore wall. (c) An SEM image of the bottom surface of gold mesh, showing loosely connected Au NPs at the edges of nanoholes. (d) A schematic illustration of removal of AAO mask, Au NPs from the bottom surface of gold mesh, and transfer of gold mesh onto a silicon substrate. (e) A photograph of gold mesh transferred onto a Si(100) wafer (2 cm x 2 cm). Reprinted with permission from⁴. Copyright(2011) American Chemical Society.

4.2.1 Etching p-type nanowires

For the Si MIS devices studied in chapter 7, we etched a series of p-type silicon wafers from 10 ohm, 0.1 ohm and 0.01 ohm wafers. P-type silicon can produce a blocking contact with an oxide layer and an Al contact and an ohmic contact on bare Si. N-type silicon is readily etched with the MACE process, the choice of contact material for MIS devices is usually Au, which is more challenging to image with EBIC underneath contacts without spreading the electron beam.

For the noble metal we selected gold. Gold has a slower etching rate, but it is easier to control because the film stays intact during the etching process. There is still the issue with nanoparticles becoming loose and creating porous material at the start of the etching process, but that can be eliminated using a rinse in dilute

aquaregia (a mixture of HNO_3 , HCl with a ratio 1:3).

We originally tried to find a lithographic process using e-beam lithography and a negative tone resist to define arrays of dots and different sizes and coat the wafer with gold and lifting off the pattern. This did produce nanowires in some cases. However, it was difficult to reproduce the results from batch to batch.

To etch the nanowires we modified a process from⁴. The process is diagrammed in Fig. 4.2. We used anodized aluminum oxide (AAO) templates for a periodic array of holes of varying sizes from 50 to 300 nm in diameter. The AAO templates were sputtered with 20nm of Au to create a uniform film. The templates are dissolved in a solution $NaOH$ and the Au film is left floating on the surface. Taking a p-type $<100>$ Si wafer chip we place it into the solution at an angle then gently pull the chip out: Au film is reatined by the surface tension.

The film can be transferred to a rinse of deionized water to remove any $NaOH$ that is left from etching of the AAO templates. We then take an BOE etched Si wafer and deposit the film onto it by pulling at angle letting the surface tension hold it in place. Once the water dries we use a N_2 to further dry the sample. The film is held to the surface the subsequent processing through van der Waals forces and cannot be removed except in aquaregia.

To remove any Au nanoparticles that may become free in the etching solution we placed the chip in dilute aquaregia for 10 minutes. This is followed by a second rinse in DI water. We then place the chip in a solution of H_2O_2 , HF , and DI water for 1 hour.

The etching rate is highly dependent on the doping level of the wafer as this im-

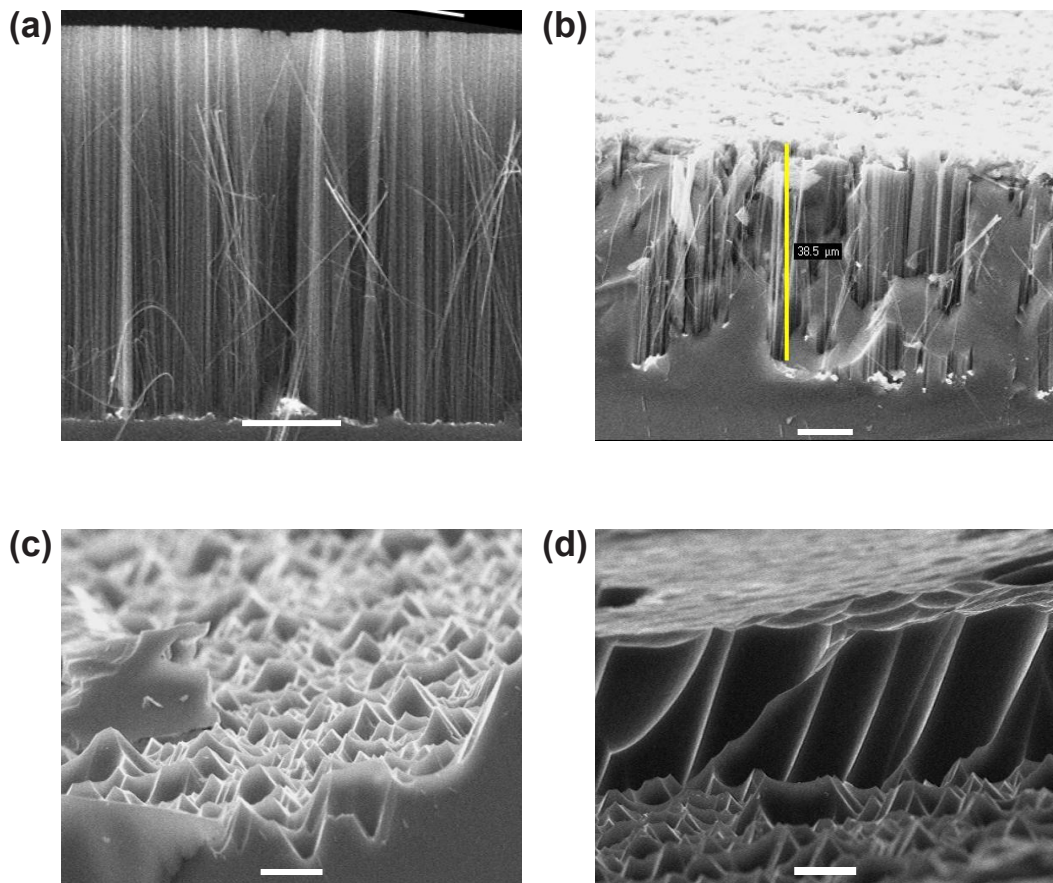


Figure 4.3: (a) Si nanowires etched from p-type $<100>$ wafer with a $2E15$ Doping level, etch rate of $40 \mu\text{m}$ an hour. (b) Si NAnowires etched form ptype $<100>$ wafer with doping level of $2E16$. (c) Etching of ptype $<100>$ wafer with doping level of $2E17$ in the presence of Au film. (d) same wafer as (c) shows both where metal is present and etching just on the surface. All scale bars are $10 \mu\text{m}$.

pacts how much hole injection occurs. We expected to have different etching rates for the different doping levels. The fastest etch rate of $100 \mu\text{m}$ an hour (Fig.4.3) was on the lightest doped wafer with a resistivity of and doping level of $2 * 10^{15} / \text{cm}^3$. The p type $<100>$ Si wafer with $2.0 * 10^{16} / \text{cm}^3$ level doping had an etch rate of $40 \mu\text{m}$ an hour.

For the highest doped p-type $<100>$ Si wafer, with a doping level of $2.0 * 10^{17} / \text{cm}^3$ no nanowires where etched. Instead we ended up with pyramid type

structures along the $<111>$ directions. There are two possible mechanisms that can lead to this behavior. The pyramid structures are only visible where the Au film was present. The film was porous just as in the case with the other lower doped nanowires. It has been observed that the dopants themselves, at high enough concentrations can promote etching. We observed etching everywhere even outside of the areas with the Au film. However, the pyramid structures are only present underneath where the Au film was present (Fig.4.3). This result identifies the limits of this technique in regards to etching higher doped materials in which the contribution of the dopants becomes a significant contributor to the etching behavior.

Crystal Orientation and Quality

The crystal orientation in the MACE process is determined by the wafer and preferential etching in the $<100>$ direction. We collected TEM micrographs of the same batch of Si nanowires used to make the device studied in Chapter 8. The crystal orientation was in the $<100>$ direction as expected, and they are single crystalline structures with no porosity found.

Oxide Thickness

The oxide thickness as determined by TEM is not consistent along the length of the wire, going from 10 nm in some regions to less than 2 nm in others whereas the etching rate appears to be uniform when looking at the length of the nanowires. For even etching rates of oxide buffered oxide etch (BOE) is used. Since the MACE etching solution contains both HF and H_2O_2 it is to be expected that both processes are active and that oxide growth and etching will happen at different rates outside of the region where the catalyst film is present. For a uniform oxide thickness we

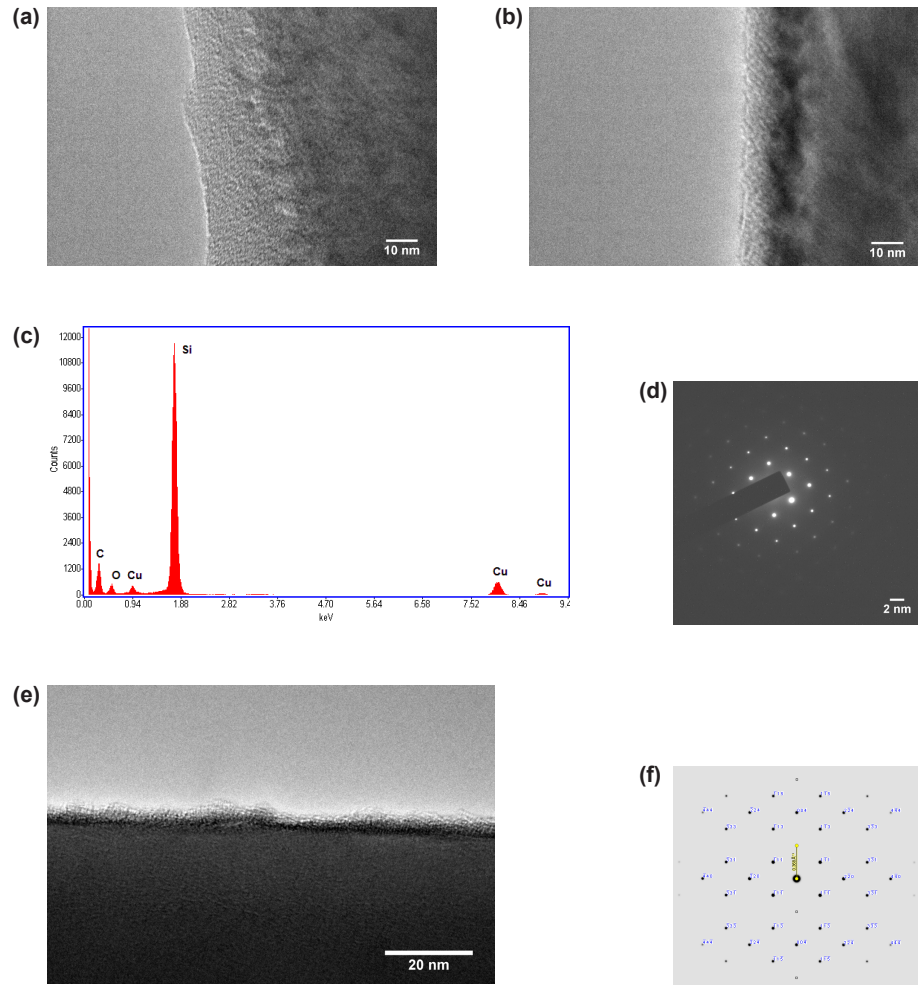


Figure 4.4: (a)(b) Two regions on same nanowire etched using MACE process with a doping level of $2E15/cm^3$, oxide thickness varies from 10 – 20 nm after MACE process.(c) Elemental analysis show Si and O peak form the wire Cu and C peaks are from TEM grid. (d) Diffraction pattern of (a)(b) shows nanowire is single crystalline. (e) TEM of $2E15/cm^3$ p-type nanowire after BOE etching process removing oxide and uniform thickness of 3 to 4 nm.(f)Calculated diffraction pattern for zone axis in (d).

need to treat the wires with a post etching process that selectively etches away the oxide.

Post Etching Treatment

To remove the Au film that is still left behind after the etching process, the sample is placed in non diluted aqua regia for 20 minutes. After the film is removed the sample is rinsed in DI water and then placed in a buffered oxide etching solution with a concentration of HF of 50:1 for 20 minutes, ensuring that the oxide is completely removed. Only a native oxide is present when devices are fabricated.

4.3 Device Fabrication

Making devices out of nanowires entails further processing, where electrical contacts and other interfaces to the semiconductor nanowire are made or modified through a passivation process.

4.3.1 Nanowire Deposition on a Substrate

To prepare a device out of a nanowire we need to place the nanowire on a substrate. The typical substrate used is a Si wafer that is degenerately doped, so it is highly conductive, with a thermal silicon oxide of 200 nm. This substrate allows for electrical contacts to be defined lithographically and have them electrically isolated from the substrate and each other. The degenerate semiconductor substrate under the SiO_2 can be used as a back gate contact or grounded during measurements to avoid charging of the substrate.

The chip containing the grown or etched nanowires is placed in IPA and sonicated for 1 second. This dislodges the nanowires from the substrate. We add a

drop of Tween 20 as a surfactant to keep the nanowires from sticking together. The device substrate is heated to 100 degrees C and a pipette is used to add a drop of the nanowires in solution a drop at a time. As the drop evaporates it leaves behind the nanowires. Since the substrate is heated, it causes the droplet to maintain a contact angle with the substrate instead of wetting to the surface. Under a optical microscope, nucleation of bubbles can be observed from where the nanowires are located.

To get rid of any remaining residue from the Tween 20, several more drops of IPA are added to the heated nanowire substrate until it has been rinsed clean. This also dislodges nanowires that are deposited on top of each other so that single nanowire devices can be made.

4.3.2 E-beam Lithography

For making single nanowire devices, E-beam lithography is one of the most versatile patterning tools we have. Using the high energy electron beam of an SEM (NPGS) or a dedicated system such JEOL 6300, at Brookhaven National Laboratory (BNL) it exposes a polymer resist PMMA that is spin coated on the substrate. PMMA, a positive resist, is exposed it under goes changes in solubility and is developed in a solution IPA and MIBK (ratio of 3:1) for 70 seconds and then rinsed in IPA for 20 seconds then air dried. Very fine features can be written with E beam lithography. In case of the dedicated system with high acceleration voltages of 100kV a resolution of 2 nm can be achieved.

The substrate has an array of markers on it so that electrode patterns on devices can be designed. A global set of alignment markers allows us to locate the



Figure 4.5: E-beam lithography process and metal deposition. (i) Si substrate with 200nm of thermal oxide is spin coated with PMMA. (ii) where PMMA is exposed to E-beam it dissolves in development process. (iii) Deposition of metal on sample both exposed area and PMMA. (iv) metal is deposited on substrate after lift off process where PMMA is dissolved in NMP removing un-patterned metal.

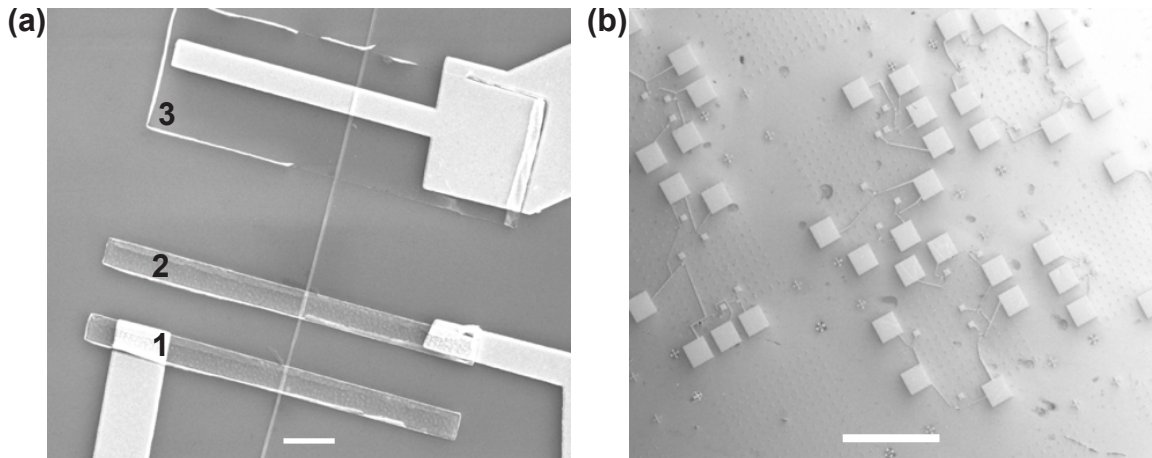


Figure 4.6: (a) Si MIS device with e-beam defined contacts (1-2) are ohmic contacts with sputtered Al with 1 percent Si(3) is a Schottky contact with oxide left underneath as a barrier, scale bar is 2 μm . (b) Several devices fabricate on one substrate, scale bar is 500 μm .

nanowires and pattern PMMA. With the system at BNL an entire wafer of markers on a Si wafer with 200nm of thermal oxide was written. The alignment markers need to be made out of Au so they visible to the electron backscatter detector used for finding the alignment markers and correcting for any rotations.

Using the alignment markers enables fabrication of devices with multiple lithography process steps and metalizations and subsequent patterns can be aligned with the first ones. Typically we fabricated many devices on the same substrate as seen in Fig. 4.6.

Once the sample has been exposed to the beam and developed a gentle plasma clean is applied to remove any residue from the development process.

4.3.3 Metal Contacts

The PMMA development process opens a window where the beam is exposed. Inside this window we can either etch the material or deposit more material. Etching is necessary in many devices to remove any oxide and contact the semiconductor to make an ohmic contact. In the case of the Si MIS nanowire in chapter 8, we used a 15 second dip in buffered oxide etch to remove the native oxide before depositing Al contacts.

In the case of the GaAs/AlGAs nanowires studied in chapter 6, several layers of metal are used to create the ohmic contacts as well as an annealing process.

Thermal Evaporation

In thermal evaporation the sample is placed inside an vacuum enclosure. The source material for the metal pattern is heated in a boat and an electrical current is passed through until the boat reaches the melting temperature of the material. A plume

of evaporated material gets deposited on the sample. The vapor pressure of the metal determines the deposition rate usually a rate of 0.1 to 0.4 angstroms per second monitored with a quartz micro-balance.

Typically in making metal contacts an adhesion layer is needed to make sure the metal sticks to the surface. Either Cr or Ti make excellent adhesion materials. Ti is very good at creating a diffusion barrier and prevents the top material from going into the substrate or the device underneath. After the adhesion layer is applied, the electrode material is deposited. For many of the Ge nanowire devices studied in this thesis we used Au as the deposition metal to make Schottky contacts.

Sputtering

Sputtering Ar ions bombard the surface of a target on a magnetron releasing atoms of the source material. This creates a plume of material with high energy atoms that bombard the surface. The grain size is much smaller and has good adhesion to the material. Sputtering has less line of sight characteristics making it hard to use in lift off processes. For the Si MIS nanowire device we specifically choose magnetron sputtering because it has a more conformal coating.

Liftoff

After the metal contacts are deposited, the rest of the un-patterned metal is removed through a lift-off process where the resist is dissolved in acetone or NMP and the metal comes off with it. Lift-off processes can take hours to avoid pulling up too much or leaving too much behind. The sidewalls of the resist are key to having a clean lift-off process. In some cases an undercut structure is created using a copolymer MMA that is exposed much more rapidly so the metal has a clean break

with the surface instead of being deposited on the sidewalls.

Annealing

Many of the nanowire devices we studied go through an annealing process. This forms bonds at the interface of the metal and semiconductor leading to more consistent transport behavior. Annealing is usually a required process for creating ohmic contacts. But both ohmic and Schottky contacted devices exhibit improved performance after an annealing process.

The GaAs/AlGaAs nanowire devices go through an RTA annealing process where it is rapidly heated by IR lamps. In the case of the Si MIS devices, the nanowires are annealed at 450 degrees C in an atmosphere of H_2 and Nitrogen with a base pressure of for 1 hr.

Chapter 5: Evolution of field-induced impact ionization

We report on the local effects of hot carriers on the transport characteristics within Ge nanowires investigated using electron beam induced current microscopy (EBIC). Dependence of both bias and gating on the EBIC current is collected and used to extract sets of local potential profiles along the nanowires. Applying voltage bias that is greater than the depletion threshold voltage, while imaging with EBIC, caused irreversible changes in the local electric field. These changes are attributed to interactions of hot carriers and field-induced impact ionization that leads to generation of dislocations. Dislocations result in a significant increase of the EBIC signal, consistent with a local environment that supports micro-plasma formation, including carrier multiplication.

5.1 Hot carriers

Hot carriers are central to the operation of a wide range of modern semiconductor devices. For example, one method for improving the efficiency of photovoltaics involves harvesting energy from hot carriers, which is usually lost as heat^{29–31}. Hot carriers are key to real-space transfer nanowire (NW) devices that permit novel modes of tuning nonlinear optoelectronic response characteristics³². The interaction of hot carriers with the lattice, forming micro-plasmas that possess an internal electric (E)-field, is known to cause carrier multiplication^{33–35}. The study of the role of hot carriers in the onset of field-induced breakdown in thin film devices is chal-

lenging; it is complicated by the relatively large area over which pre-breakdown or avalanche sites initiate and propagate. In contrast, the effects of hot carriers under high external bias field conditions can be more easily discerned in nanoscaled devices such as those based on NWs because of the geometric confinement.

While some insight into these effects may be gleaned from current-voltage measurements, they offer no spatial information. Scanning probe microscopy (SPM) techniques such as scanning photocurrent microscopy and electron beam induced current (EBIC) can be used to obtain the local differences in E-fields with high spatial resolution, which is only limited by the spot size of the SEM. EBIC is complementary to scanning photocurrent microscopy, but uses keV-scale electron energy excitation, and its highly local excitation permits finer spatial resolution than optical diffraction-limited techniques. These differences are significant for resolving variations in the local E-field in NWs owing to dislocations, to modulation in composition or to doping, and in NW devices with a contact separation much smaller than the optical diffraction limit. In addition, EBIC can be used to probe sub-surface regions, beneath electrical contacts, and under much higher-energy excitation.

Among single-component semiconductor NWs, the GeNW system is an attractive choice since it possesses the highest combined hole and electron mobilities². GeNWs attract interest for use in visible- and infrared-wavelength photoconductors due in part to their high conductivity³⁶. Here we show how the EBIC probing of the local field within metal-semiconductor-metal (MSM)-contacted GeNWs, with Schottky contacts, under bias and electrostatic gating reveals effects of the combination of high field and hot carriers on dislocation generation and carrier multiplication.

GeNWs were grown via Au nanoparticle-catalyzed chemical vapor deposition, as reported elsewhere³⁷. The as-grown GeNWs were briefly sonicated (~1 s) in isopropanol and transferred from solution onto degenerately doped *p*-type Si wafers possessing a 200-nm thick thermally grown SiO₂. The wafers were each back coated with 5 nm Cr and 100 nm-thick Au films to facilitate gating of the GeNWs and to ground the substrate to reduce charging effects. The GeNWs were electrically contacted (Fig. 5.1) using electron beam lithographic patterning of the contact metallization (5 nm Cr, 150 nm Au). For EBIC characterizations, each sample was then mounted into a ceramic chip carrier and wire bonded.

EBIC measurements were performed on the GeNW MSM devices under voltage bias (V_b) and substrate gating (V_g) using an in-house designed and built scan generator and data acquisition system. The acceleration voltage was 11.0 kV and the beam current was 50.0 pA. At 11.0 kV no charging was observed and the minimum amount of beam current was used to obtain a signal. Multiple scans taken at the same voltage bias show a consistent response. The electron beam was swept perpendicular to the axis of each GeNW with a dwell time of 20 ms per point and a step size of 15 nm. The spot size of the SEM used in the experiments is 1nm. Both DC²⁵ and lock-in methods²⁴ have been used to measure the EBIC response in NWs. Here, the current is measured at the cathode through a trans-impedance amplifier and is AC-coupled to remove any variance in the DC response over the time it takes to scan the wire. The secondary electron (SE) images and the EBIC image are obtained simultaneously; the SE signal is used to align the location and trajectory of the subsequent EBIC line-scans.

In order to understand the extent of the interaction volume of the e-beam with the GeNW, we performed Monte Carlo simulations on intrinsic Ge for a bulk sample ($5 \mu\text{m}$) and for a thin film (100 nm) of Ge using NIST Monte³⁸, with an incident beam energy of 11.0 kV. In the thin film simulation the electron beam remains narrow: the majority of electrons are confined to within 5 nm and the remainder are within 20 nm. Only a few of the electrons are scattered within the GeNW, causing little broadening of the interaction volume. Finer features than the interaction volume can be resolved because the signal is integrated over a new volume when the beam position is changed. Because the GeNW is electrically isolated from the substrate, once electrons exit the GeNW they no longer contribute to observed EBIC signal.

Current-voltage traces were collected prior to and following application of bias voltages during EBIC imaging Fig.5.1. GeNW MSM devices can be thought of as two back to back Schottky diodes with potential barriers at each contact. This response is representative of our GeNW MSM devices prior to application of a voltage bias and EBIC imaging. In the MSM device configuration one contact will be forward biased while the other is reversed biased. Many photo-diodes use this type of device configuration for low dark current. After all EBIC measurements, the observed current-voltage possesses a pronounced hysteresis, likely resulting from charging and discharging of the induced dislocation(s).

EBIC scans were performed sequentially on the GeNW from V_b (= 0.5 V) to V_b (= 5.5 V), with the exception of V_b = (0.96V) which was taken after all the other measurements and shows the GeNW did not return to its initial state. At V_b (=

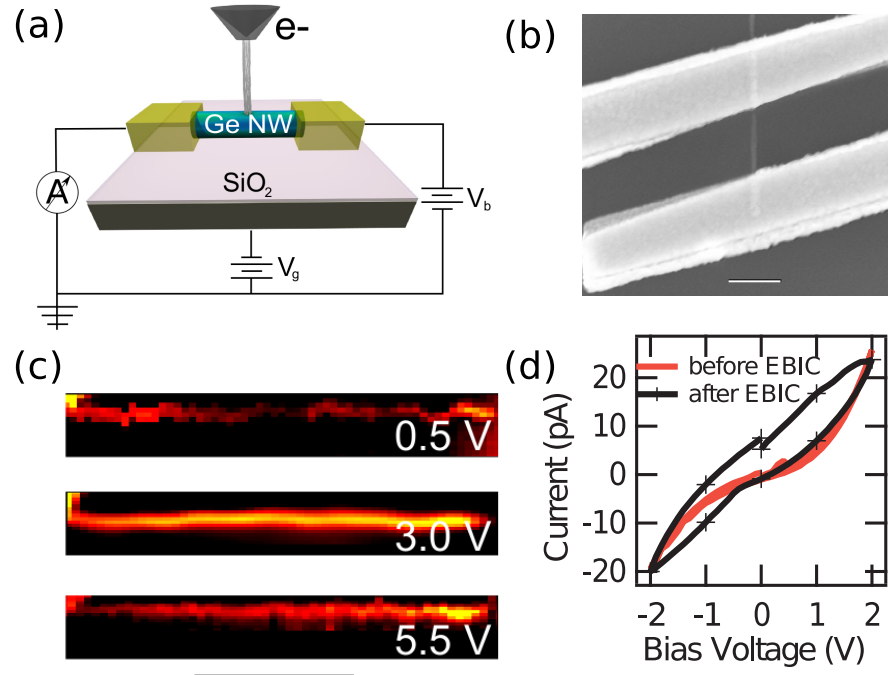


Figure 5.1: (a) Schematic of EBIC measurements, (b) SEM image of MSM contacted GeNW (diameter 60 nm, scale bar is 1 μm), and (c) EBIC images with V_b denoted in each. Each image is normalized relative to a maximum current scale bar is 500 nm. (d) Current-voltage data for the GeNW prior to (red, solid) and following (black, with crosses) EBIC imaging and the formation of a localized high E-field near the anode and is attributed to dislocations. (d) Current vs voltage measurements conduct before and after EBIC measurements are conducted. The response before EBIC is characteristic of a MSM device with Schottky contacts at each end. The hysteresis in the measurements after EBIC is attributed to dislocations charging and discharging that were formed after impact ionization process.

0.5V) the observed current response is only near the contacts; Ge has ambipolar transport due to the high mobility of electrons and holes, and both contribute to the response. For V_b (= 3.0 V), the GeNW is fully depleted and is seen to contribute to the observed response and a peak emerges ($1.1 \mu\text{m}$), close to the anode. Further increasing V_b (= 4V and 5.5V) past the point where the GeNW is fully depleted, leads to an increase of the peak, to 10.0 pA at $V_b = 5.5$ V. Plots of the relative potential within the GeNW are obtained by spatially integrating the EBIC signal (Fig. 5.2). At $V_b = 5.5$ V the peak dominates the EBIC response and the resulting potential profile (Fig. 5.2).

The most notable change in the EBIC response under increased bias and substrate gating ($V_g = -1.0$ V, -3.0 V, Fig. 5.2) is in the vicinity of a peak near $1.1 \mu\text{m}$. The GeNW is not intentionally doped, suggesting an accumulation of holes under gating conditions in the wire. A substantial increase in potential profile near $1.1 \mu\text{m}$ is seen (Fig. 5.2) with increased bias and gating; the evolution of this feature suggests that strong local E-field has formed, which maybe caused by dislocations induced from high energy holes impacting the lattice.

The polarity of the applied bias was then switched to investigate the character of the strong local E-field, the cathode is located at $1.3 \mu\text{m}$ and the anode at $0.0 \mu\text{m}$ (Fig. 5.2). If the wire was not exhibiting a permanent change, then the profiles of the EBIC signal would have had the same characteristic shape and slope gradually up from the cathode to the anode, however this was not the case. For ~ 300 nm from the anode, a nearly uniform current (50 pA) is seen, beyond which it is seen to decrease sharply. The localized strong E-field that we attribute to dislocation(s)

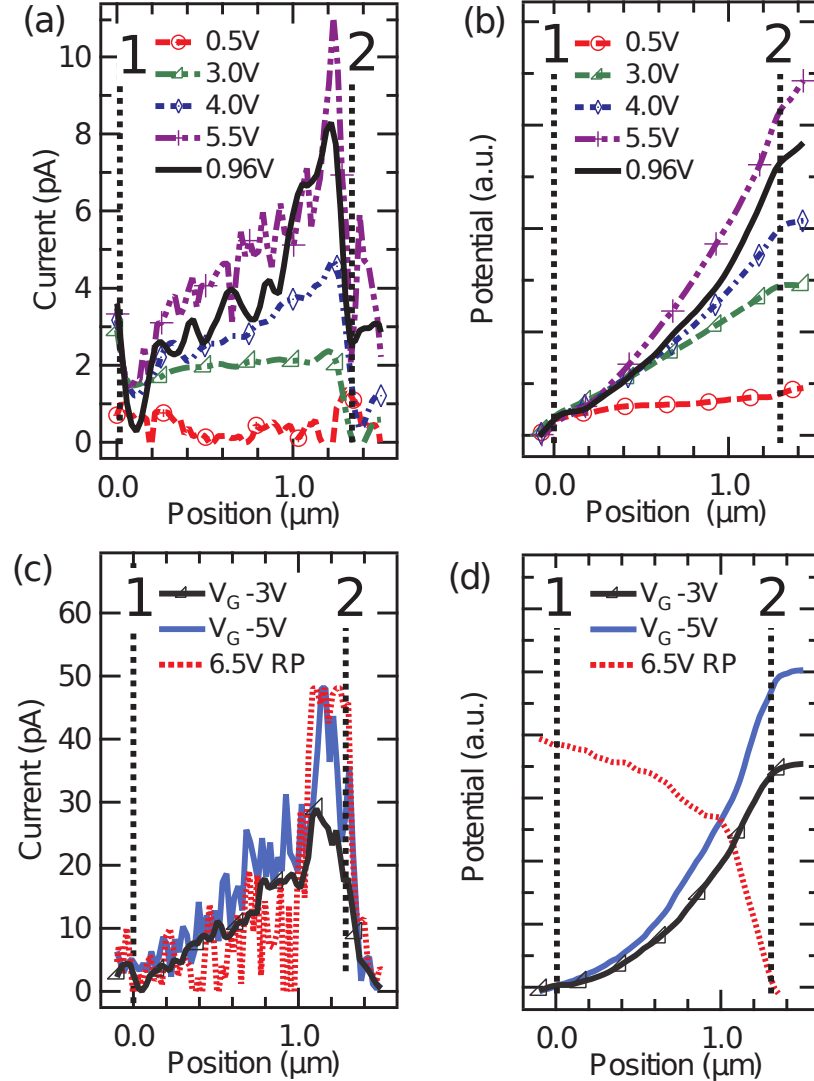


Figure 5.2: (a) Current profiles taken from EBIC images at selected values of V_b for the GeNW shown in Fig. 5.1 as denoted in the legend. The locations of the cathode (1) and anode (2) are denoted by dashed lines. (b) Corresponding potential profiles obtained from integrating the current. The EBIC profile for $V_b = 0.96V$ (black, solid) was collected last among this series of EBIC data on this device, and the local maximum in the EBIC current is seen to be much larger than that collected for nearly all other (larger) values of V_b . (c) EBIC profiles collected at $V_b = 6.5V$ with $V_g = -1$ and $V_g = -3V$. Also shown in (c) is that for reverse polarity (RP) ($V_b = -6.5V$), and its corresponding potential profile (d) (dashed red lines in each); for the trace collected under reverse bias, (1) and (2) denote the locations of the anode and cathode, respectively.

still dominate the response. The potential profile Fig. 5.2 exhibits a response (from 0.0 μm to 1.0 μm) that is similar to that under forward bias; under reverse bias the potential has a sharp decrease past the dislocation(s) approaching the cathode.

The last EBIC scan performed on this GeNW was collected under forward bias ($V_b = 0.96$ V, Fig. 5.2), taken a full day after the other scans. The EBIC profile now appears broadened, and extends to positions less than $1.0 \mu\text{m}$. The response is comparable to that collected from this GeNW previously at $V_b = 5.5\text{V}$, Fig. 5.2. The strong local E-filed still dominate the response at $V_b = 0.96$ V which is below the threshold identified for GeNW to be fully depleted . The formation of a strong local E-filed that is attributed to dislocation(s) near the anode were observed in five different GeNWs prepared and probed in the same manner as described above, suggesting that this is a preferential location for the dislocation formation.

Measurements of local E-fields are also seen in SPC. The observed photocurrent is proportional to the local E-field along the axis of the NW, $I_{ph}(x) \propto E(x) = -dV(x)/dx$ for drift currents. Integrating provides a potential profile^{39–42} for NWs and carbon nanotubes. Potential profiles obtained from SPC were compared to results from Kelvin probe microscopy, providing a strong correlation between the techniques⁴¹. Contrast in EBIC measured along an axially-modulated NW heterostructure has been attributed to local electric field²⁵. For our GeNW MSM devices, the signal observed within the bulk of the NW is dominated by the local E-field and has a clear voltage dependence. This indicates that the response is due to drift and that the diffusion component is negligible. The GeNWs are fully depleted as indicated by the E-field and the potential for applied volatges above $V_b = 3\text{V}$, (Fig.5.2).

The effect of electrostatic gating (V_g) on the EBIC response in a separate, (100 nm) diameter GeNW was also investigated (Fig. 5.3). The observed peak currents ($\sim 1\text{-}3 \text{nA}$) are nearly two orders of magnitude higher than the incident beam

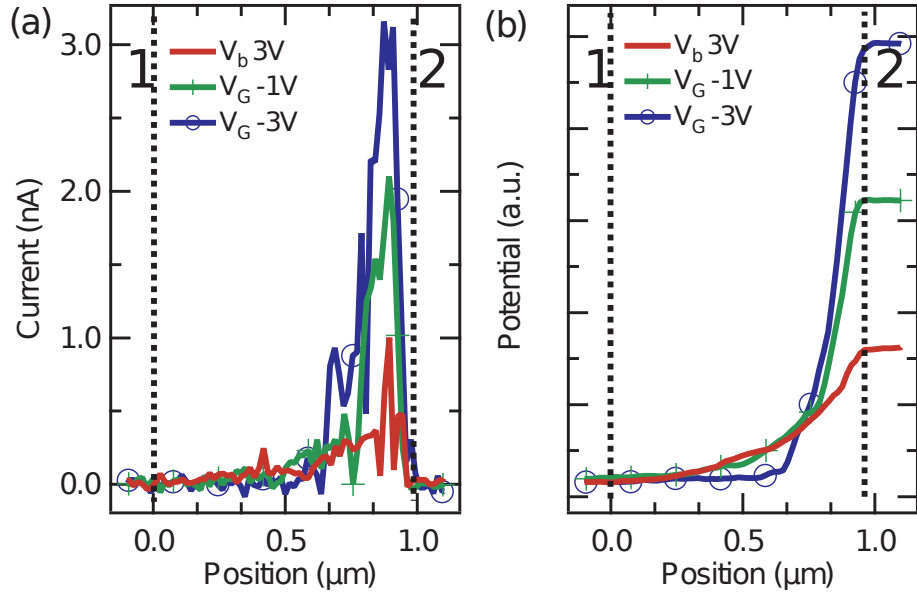


Figure 5.3: (a) Current profiles collected from a separate Schottky-contacted GeNW (diameter 100 nm) under $V_g = 0\text{V}$, -1V , and -3V after a dislocation near the anode (2) was formed under the same bias condition as that for the other GeNW, with the cathode location denoted here by (1). (b) EBIC profiles obtained with this GeNW at lower biases were qualitatively similar to that of the wire shown in Fig. 5.2 although the response for this GeNW is considerably larger than the incident beam current. Gating of the GeNW is seen to predominately affect the dislocation(s) centered at $0.85 \mu\text{m}$.

current ($\sim 50 \text{ pA}$). The effect of gating is mainly seen at the location of the dislocation(s) (Fig. 5.2). The region of the dislocation(s) also appears to have grown with successive scanning and application of gate bias. Similar effects in the observed EBIC current relative to the incident beam current were also observed in each of four other $\sim 100 \text{ nm}$ diameter GeNWs measured.

For the GeNWs studied, the preferential site for the formation of the dislocation(s) is near the anode. The results, in terms of evolution of the potential in this region, were consistent among multiple scans collected using different NWs at the same sequence of bias and gating conditions; the EBIC response changes only following changes in the bias and/or gating. The largest relative local potential within

the GeNW occurs in the region adjacent to the anode where holes are subject to the largest E-field. This, combined with the fact that the ionization rate for holes is far greater than that for electrons in Ge² accounts for why the formation of dislocations and a change in the local potential takes place near the anode. The formation of dislocations at the anode is from hot carriers, primarily holes, created by the electron beam that are accelerated by the applied E-field and impact the lattice. The mean excitation energy of carriers generated from the electron beam in Ge is ~ 2.3 eV. Since the incident electron beam has far greater energy than the band gap, electrons are excited not only from the valence band but from the split-off band.

Further supporting our claim that these dislocation(s) are caused by ionization from holes, the response of the dislocation region is influenced by gating. Under the application of a negative back gate voltage the response from the strong local E-field region is increased. With fewer electrons in the GeNW, recombination of holes with electrons is decreased and a greater number of holes can participate in the impact ionization process.

The local E-field and derived potential profile changes irreversibly after the formation of the dislocation(s). The limited dimensions of the GeNW may also be a factor in the dislocation formation near the anode, and its apparent growth and dominance within the GeNW. The behavior of these dislocations is consistent with that of micro-plasmas which are known to multiply carriers whether they are from the excitation from light or an electron beam, or from carriers injected from the contacts^{33–35}. Micro-plasma sites are thought to be defects in the form of precipitates or dense arrays of dislocations³⁵ that possess a strong internal E-field and

can cause carrier multiplication. Harnessing the energy of hot carriers in solar cells is of considerable interest in increasing their efficiency. We have created a region of strong E-field that causes carrier multiplication, which is one of the proposed routes to harvest the energy of hot carriers. Future NW based solar cells may take advantage of such multiplication sites.

The formation of the strong E-field is attributed to dislocations in GeNWs that result from hot carriers created by the electron-beam and accelerated from the applied bias voltages, greater than the depletion threshold voltage, and impacting the crystal lattice. They form adjacent to the anode due to the higher impact ionization rate for holes in Ge and propagate towards the cathode with the addition of higher applied fields and gating. The change in the local potential and E-field persists even when a much lower field is applied or the polarity of the measurement is reversed.

Chapter 6: GaAs/AlGaAs Core-Shell Nanowires

This chapter has been reformatted from the manuscript "Sub-Surface Imaging of Coupled Carrier Transport in GaAs/AlGaAs Core-Shell Nanowires"

We demonstrate spatial probing of carrier transport within GaAs/AlGaAs core-shell nanowires with nanometer lateral resolution and sub-surface sensitivity by energy-variable electron beam induced current imaging. Carrier drift that evolves with applied electric field is distinguished from a coupled drift-diffusion length. Along with simulation of injected electron trajectories, combining beam energy tuning with precise positioning for selective probing of core and shell reveals axial position- and bias-dependent differences in carrier type and transport along parallel conduction channels. These results indicate how analysis of transport within heterostructured nanomaterials is no longer limited to non-local or surface measurements. Light-matter interactions in semiconductor nanowires are drivers of new optoelectronic and photonic devices⁴³⁻⁴⁷. In III-V semiconductor heterostructures, the interface forms the basis for high-speed devices from band engineering and modulated doping^{48;49}. For instance, Type I heterostructures⁵⁰ such as GaAs-AlGaAs are beneficial for confinement of carriers and for transferred electron phenomena^{51;52}. Heterostructures in co-axial core-shell nanowires permit study of how finite size, shape, strain, interfacial atomic structure, defects, and surface influence electrostatic potential landscape and carrier conduction paths, thereby enabling new nanoelectronic device paradigms⁵³⁻⁵⁵. In buried heterostructures such as a

core with one or more surrounding shells, however, local information about excess carrier transport within and between each component needed to understand device functionality is not readily available. Additionally, increased surface-to-volume ratio in a nanowire is accompanied by surface traps, band bending, and surface recombination, all of which affect intrinsic electronic properties^{56–58}. Despite remarkable advances^{59;60}, understanding of coupling of carrier transport within core-shell nanowire components remains lacking. Thus, local probing of nanoscale contributions from carriers within surface and sub-surface nanostructured components under device operating conditions brings new insight into the operation and design of nanoscale heterojunction-based devices.

Spatially resolved current mapping with local injection of excess carriers, e.g. electron beam induced current (EBIC) and scanning photocurrent (SPC), yields characteristic lengths such as the depletion width at a Schottky contact⁶¹, diffusion length at a $p - n$ junction or within a homogeneous material⁶², and defect-induced band bending⁶³. Effective in studying excess carrier transport dynamics⁶⁴ at the interface of a semiconductor heterostructure, EBIC has superior lateral spatial resolution compared to optical diffraction-limited SPC. While a sub-micron carrier transport channel in nanowire devices is typical especially for ballistic transport studies⁶⁵, imaging along the NW radial direction demands much finer resolution: this can, in principle, be addressed by EBIC where ultimate resolution is limited by a combination of factors. Among these are electron optics and beam stability, carrier trajectory and electron beam energy- and material-dependent interaction profile, beam sweep rate and signal-to-noise, and drift.

6.1 Drift-diffusion coupling

When the conduction channel is subject to external electric field, the field will drag the excess carriers to form an asymmetric distribution. When diffusion is neglected, the carrier distribution due to drift can be analytically expressed as,

$$\Delta n(x) = (\Delta n)_0 e^{-\frac{t}{\tau}}, \text{ where } t = \frac{x}{\mu_n E}.$$

Comparing with the form $\Delta n(x) = (\Delta n)_0 e^{-\frac{x}{L_{drft,n}}}$, we can define the drifting length L_{drft} as,

$$L_{drft,n} = \mu_n E \tau.$$

Since diffusion happens simultaneously with drift in reality, we couple the drift component into the continuity equation of diffusion,

$$D_n \frac{\partial^2 \Delta n}{\partial x^2} - \mu_n E \frac{\partial \Delta n}{\partial x} - \frac{\Delta n}{\tau} = 0.$$

Using diffusion length L_n and drift length $L_{drft,n}$, the equation can be written as,

$$L_n^2 \frac{\partial^2 \Delta n}{\partial x^2} - L_{drft,n} \frac{\partial \Delta n}{\partial x} - \Delta n = 0.$$

The solution of the above equation will follow the form of $\Delta n(x) = A e^{-\frac{x}{L_1}} + B e^{\frac{x}{L_2}}$

$$L_1 = \frac{2L_n^2}{\sqrt{L_{drft,n}^2 + 4L_n^2} - L_{drft,n}};$$

$$L_2 = \frac{2L_n^2}{\sqrt{L_{drft,n}^2 + 4L_n^2} + L_{drft,n}}$$

From the above modified decay length involving the effect from the electric field, it can be easily seen that the length along the field will be extended while the one against the field is reduced.

Derivation of drift component

The field dependence of decay lengths from the EBIC measurements can be fitted to obtain L_{drft} .

$$L_{diff,n}^2 \frac{\partial^2 \Delta n}{\partial x^2} - L_{drft,n} \frac{\partial \Delta n}{\partial x} - \Delta n = 0 \quad (6.1)$$

Here drift length is introduced as $L_{drft,n} = \mu_n E \tau_n$, where μ_n and τ_n are the mobility and lifetime of electrons and E is the electric field. $L_{diff,n}$ denotes pure diffusion length and Δn is the excess carrier concentration. Under steady-state injection as boundary conditions, the solution for a decay length along the field is

$$L_1 = \frac{2L_{diff,n}^2}{\sqrt{L_{drft,n}^2 + 4L_{diff,n}^2} - L_{drft,n}} \quad (6.2)$$

It is obvious that $L_{drft,n} \ll L_{diff,n}$ at zero or low bias scenarios and therefore $L_1 \approx L_{diff,n}$. If the field is extremely large however, the drift component will be dominant, i.e. $L_1 \approx L_{drft,n}$, although this is not attained in a real material due to the sub-linear $\mu - E$ relationship under high field. Nevertheless, the bias we applied does not fall within a high-field range and we found the results using this analytic expression agrees well with our results. Reversely solving $L_{drft,n}$ from (6.2), we

have our results fit using Eq. 3:

$$L_{drft,n} = L_1 - \frac{L_{diff,n}^2}{L_1} \quad (6.3)$$

6.2 Interaction Volume

Taking advantage of the large penetration depth of an electron beam, we demonstrate a highly versatile sub-surface functional imaging approach by combining the selection of different beam energy regimes in EBIC mapping with Monte Carlo simulations of scattering of injected electrons and their trajectories. In a GaAs-AlGaAs core-shell nanowire for example the beam interacts mainly with the surrounding shell at low accelerating voltage ($V_{acc} < 3$ kV), whereas for $V_{acc} > 5$ kV the contribution from the core is apparent, even dominant. When a higher energy beam is used, a large penetration depth is accompanied by a expansion of beam interaction area deep under the surface due to beam electron trajectory from the scattering events. However, we found from the trajectory simulation results that a lateral resolution of ≈ 10 nm can be achieved.

To avoid complication from effects due to electrical contacts⁶⁶, devices were prepared with Ohmic contacts on the ends of each nanowire core (Methods and Supplementary). A field-effect hole mobility of $13 \text{ cm}^2\text{V}^{-1}\text{s}^{-1}$ is estimated from back-gate results^{67;68}. The value is expected to be lower than the intrinsic core mobility due to the shielding effect from the shell and insufficient coupling and inhomogeneous field^{68;69}.

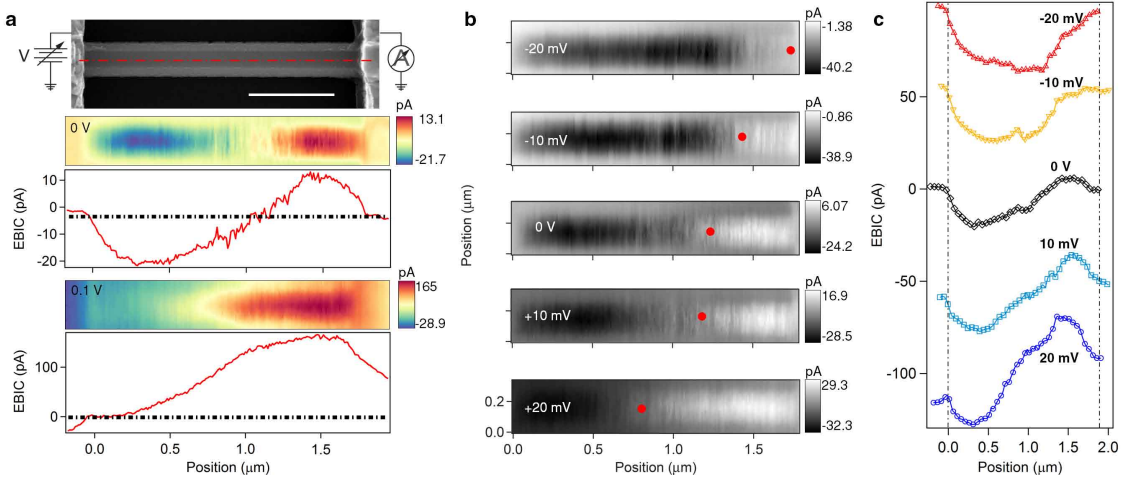


Figure 6.1: Evolution of the electronic landscape at the onset of small bias voltage. (a) EBIC images and selected line profiles $V_b = 0$ V (middle) and $V_b = 0.1$ V (bottom) taken along the center axis of the nanowire (red dash-dot line in SEM image). The right side contact is grounded. The black dash-dot lines denote zero current. The scale bar is 500 nm. A circuit diagram is superimposed on the SEM image to indicate the bias direction. (b) Series of EBIC images collected $-20 \text{ mV} < V_b < +20 \text{ mV}$. Red dots indicate the location along the nanowire where the sign of the current changes. (c) The EBIC central axis line profiles extracted from (b). Profiles are offset by 50 pA for clarity.

6.3 Characteristic Lengths

For low V_{acc} ($= 3$ kV) and at zero bias V_b (Figure 1), the signal profile along the axis of the nanowire is anti-symmetric due to diffusion and local injection-induced field, an effect that is not intuitive, but has been successfully modeled numerically.³. The central anti-symmetric point corresponds to a net zero current from the equal number of carriers diffusing to either contact. When the injection point moves away from the center (e.g. to the right), the induced field compensates the faster electron diffusion and a net positive current is reached in steady-state. From $0 < V_b < 0.1$ V the EBIC axial line profiles reveal a remarkable transition from anti-symmetric, in which the diffusion and injection induced field dominate the transport, to a peak shape with the same sign of excess current and having nearly exponential decay

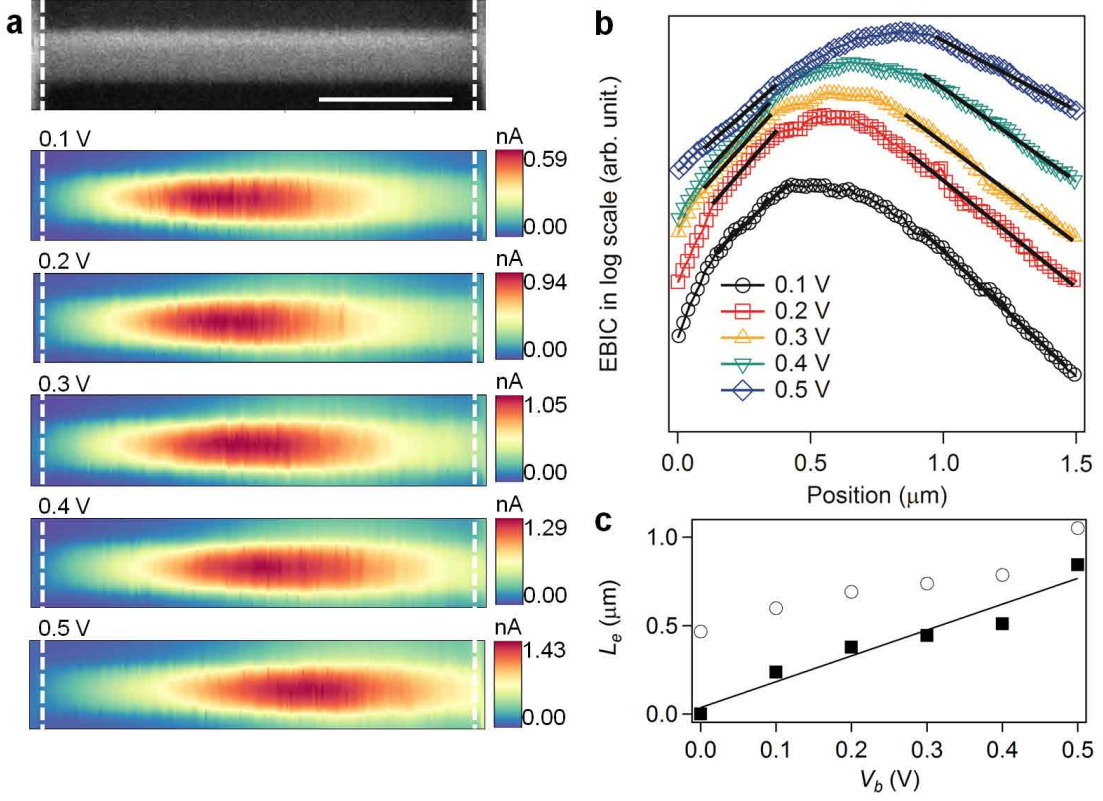


Figure 6.2: EBIC at low accelerating voltage V_{acc} . (a) EBIC maps of a single NW device at $V_b = 0.1, 0.2, 0.3, 0.4$, and 0.5 V (right side contact is grounded). White dashed lines indicate the locations of the contacts. The secondary electron image (top) is collected simultaneously, and the scale bar is 500 nm . (b) Line profiles along NW axial direction. Best fittings are shown in solid lines (black) on both sides of the EBIC signal maxima. (c) the electron drift component (solid squares) is separated from the diffusion-drift decay length (open circles); both are plotted versus V_b . The line in (c) is a linear fit of the drift length vs. V_b .

on both sides (Figure 1a). It is due to the fact that the external electric field (even at 0.1 V) is sufficiently large to overwhelm the effect from injection induced field. We investigated the process of this transition more closely. By increasing V_b from negative to positive in the vicinity of zero-bias (Figure 1b), a continuous shift of the anti-symmetric point ($\approx 1.2 \mu\text{m}$ over 40 mV) is evident. At even higher positive (negative) bias, the negative (positive) part of the signal is merged into the corresponding contact and the entire profile evolves into having a unidirectional sign.

By introducing a larger uniform external electric field along the length of the nanowire, the signal is significantly enhanced due to the drift current component. The two mechanisms of transport, diffusion and drift, form a self-consistent carrier propagation pattern characterized by a joint decay length. A peak appears indicating a transition from electron- to hole-limited current. By moving the injection point away from the peak, the number of excess carriers reaching their respective collecting electrode decays exponentially. The sign of the current over the entire nanowire is unidirectional. The contribution of drift component becomes more significant at higher bias. Serial EBIC scans at biases ranging from 1 V to 5 V with the interval of 1V are shown in Figure 2. When the bias is increased, the peak shifts toward the carrier collector for which the corresponding type of carrier has lower mobility. At $V_{acc} = 5$ kV, the beam mainly interacts with the shell. The peak shift is not significant since AlGaAs has a low electron mobility and the mobility difference between electrons and holes is minor. When the bias increases from 0.1 V to 0.5 V, the electron decay length obtained by exponential fitting evolves from $0.60 \mu\text{m}$ to $1.05 \mu\text{m}$ and the hole decay length from $0.31 \mu\text{m}$ to $0.68 \mu\text{m}$ (Figure 2a, c). The extracted lengths are also typical for $\text{Al}_{0.24}\text{Ga}_{0.76}\text{As}$ ⁷⁰. Under bias, the decay lengths are altered from the symmetric diffusion of carriers from a point injection, those along the applied field extended and against the field shortened. A more quantitative approach can be understood from the diffusion-drift continuity equation with the drift term associated with mobility and electric field⁷¹ (Supplementary Information). The derived drift component can be expressed as $L_{drift,n} = L_1 - L_{diff,n}^2/L_1$ where drift length is introduced as $L_{drift,n} = \mu_n \tau_n E$, with μ_n and τ_n the mobility

and lifetime of electrons, respectively, and E the electric field. L_1 is the measured decay length, and $L_{diff,n}$ denotes pure diffusion length at zero bias.

The drift components derived from the extracted decay lengths are found to be linearly dependent on the applied field. From the drift component, important transport parameters are uncovered. Our result gives a $\mu\tau$ product of 2.78×10^{-8} cm²/V for electrons in the shell. An electron lifetime of ≈ 2 ns is expected⁵⁸, and thus the mobility is estimated to be ≈ 10 cm²V⁻¹s⁻¹. The value is lower than bulk value probably due to a moderate doping and surface depletion. Considering the additional contribution from the GaAs core at high bias, the actual value may be even lower. Indeed, a small fraction of injected electrons penetrates deep enough to reach the high-mobility GaAs core. A shift in the peak position toward the hole collector is observed for $V_b > 0.4$ V when the core drift current component becomes large enough. The phenomenon is more conspicuous for larger beam energies.

6.4 Selectively Probing Core and Shell

Progressively larger accelerating voltages, coupled with nm-scale lateral resolution, enable high selectivity in sub-surface nanostructure component transport characteristics. For example, with $V_{acc} = 10$ kV, the interaction volume reaches the GaAs core (Figure 3c), where the signal has contributions from both the core and the shell (Figure 3a). The integration of the Monte Carlo-simulated carrier density generated by the incident electron beam over different regions (i.e. core and shell) enables construction of spatial profiles and differences in generation rates along the nanowire radius within the core and shell (Figure 3d, Methods and Supplementary). Compared with $V_{acc} = 3$ kV or 5 kV, the generated carrier density in the

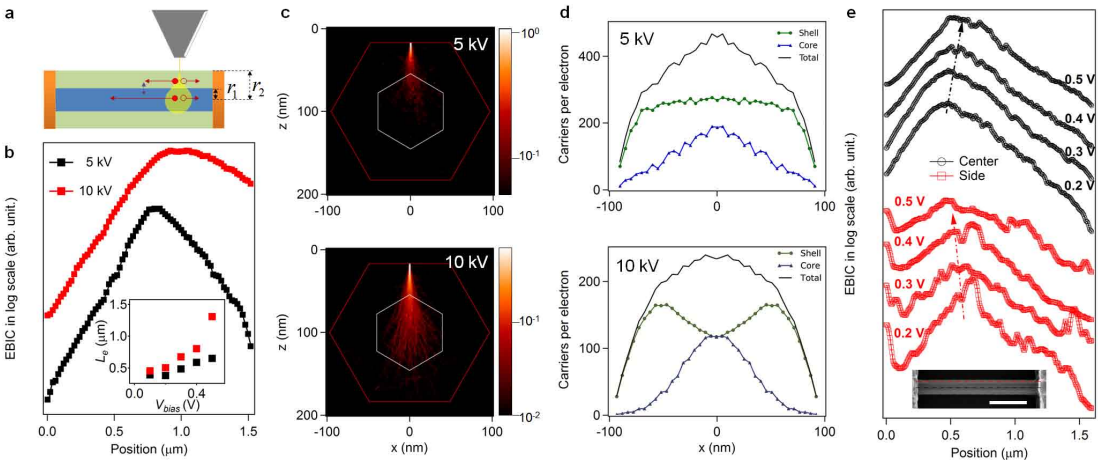


Figure 6.3: Beam energy-selective EBIC revealing transport in GaAs core. (a) Illustration of beam interaction with the two parallel transport channels having different excess carrier transport properties. The different length of red arrows indicates the mobility difference and the purple arrow indicates the possible interaction between the core and the shell. (b) Comparison of the EBIC line profiles under $V_{acc} = 5 \text{ kV}$ (black) and $V_{acc} = 10 \text{ kV}$ (red) at $V_b = 0.5\text{V}$. Inset shows evolution of the decay lengths versus V_b for $V_{acc} = 5 \text{ kV}$ (black squares) and $V_{acc} = 10 \text{ kV}$ (red squares). Monte-Carlo simulations of (c) beam trajectories when the beam is on the central NW axis and (d) carrier generation dependence on beam incident positions obtained by integrating in core and shell areas in maps, for (c) in $\text{GaAs}/\text{Al}_{0.24}\text{Ga}_{0.76}\text{As}$ nanowire cross-sections with hexagonal facets, under two different values of V_{acc} . (e) EBIC profiles at central axis (black) and side axis in shell region (red) as denoted in the inset (scale bar is 500 nm), revealing opposite drift directions.

core when beam position is at the center for $V_{acc} = 10$ kV is comparable to that in the shell due to larger penetration depth. Indeed, the central profile involves both the core and shell. Since the core electron mobility is expected to be significantly higher, the average joint decay length is expected to increase as a result. A direct comparison is shown in Figure 3b between scans under a 5 kV beam and a 10 kV beam at $V_b = 0.5$ V. A clear increase of decay length at 10 kV is seen. In fact, such increase occurs in the entire bias range from 0.1 V to 0.5 V (Figure 3b Inset). This difference without ambiguity demonstrates that a high-mobility core contributes to the overall EBIC with a dominating drift current component.

Striking differences in the EBIC profiles collected along the nanowire axis at center and at side (the Monte-Carlo is shown in Figure S2b) reveal the effects of different carrier properties in the core and shell, respectively (Figure 3e). For the center profile where e-beam interacts with both the core and the shell, shifts in the location of the observed peak with different bias are opposite that for the side profile, where only shell is concerned. Again, the direction of EBIC peak shift depends on the mobility difference. When $V_b > 0.2$ V the opposite direction of peak shift between the central and side profiles is observed due to the dominance of the core contribution at larger bias. For the core, the shift is toward the hole collecting electrode due to electron having a larger mobility, whereas the shell shows a shift, though not as significant, to the electron collecting electrode. Considering the radial distance between where the two profiles are extracted, these results explicitly demonstrate that transport characteristics near a sub-surface heterostructure can be resolved to within ≈ 10 nm in the imaging plane.

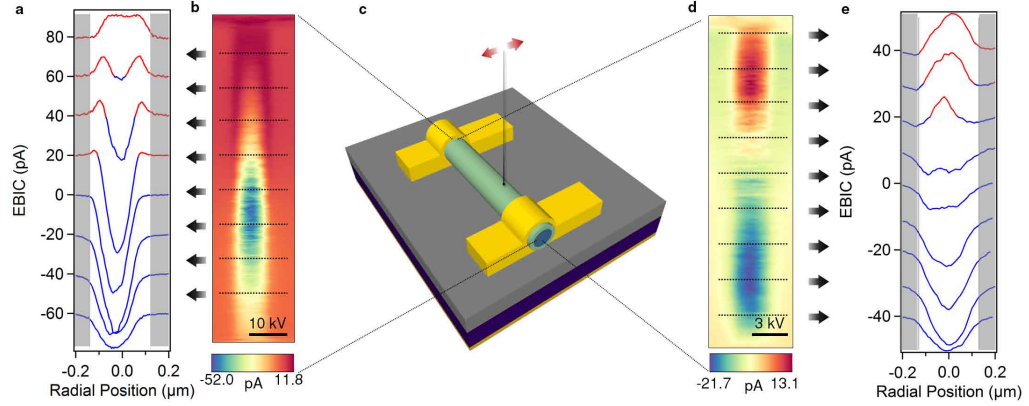


Figure 6.4: High-resolution radial profiles at zero bias. (a) and (e) Radial line profiles extracted at 200 nm intervals with $V_{acc} = 10$ kV and $V_{acc} = 3$ kV from EBIC maps (b) and (d) respectively, where black dashed lines denote the corresponding axial locations from which profiles in (a) and (e) have been extracted in an electrically-interfaced nanowire as illustrated in (c). Radial line profiles presented in (a) and (e) have two colors: red indicates positive current and blue negative. Grey areas in (a) and (e) denote areas exterior to the nanowire. Radial current profiles are offset by 20 pA in (a) and 10 pA in (e) for clarity.

6.5 Radial Profiles

Radial profiles collected using different V_{acc} reveal carrier and transport types, and degree of coupling between core and shell channels. Extraction of a series of radial profiles collected using $V_{acc} = 3$ kV and 10 kV at zero bias along different axial positions reveals changes in the sign of the current in several profiles (Figure 4). Distinct parallel transport channels from the core and the shell can be discerned at 10 kV. Significantly, current sign inversion from core to shell within a radial scan at the same axial channel position further indicates carrier transport in the two channels is partially decoupled (i.e. the core and shell channels possess their respective zero-bias profiles while the interaction between channels is negligible). Unlike carriers with different properties in homogeneous material tending to form a self-consistent ambipolar coefficient, the energy barrier at the core-shell interface impedes the interaction between two individual transport channels. When the beam interacts only

with the shell (Figure 4b) the difference in the current profiles is limited to only amplitude since the decay length is expected to be uniform in homogeneous material. The EBIC scan in Figure 4d is identical to Figure 1a. We note that the hole is also subject to the band bending which may facilitate a transfer of the holes in the shell across the interface into the core. However, the shell holes have both a short recombination time and low mobility resulting in an insignificant contribution to the overall current. Additionally, the surface depletion induced band bending drives the hole to the reverse direction. Therefore, such effect is negligible in the EBIC signal especially when the core and shell have similar values of hole mobilities. Finally, we also note that, if axial profiles are extracted from Fig. 4d, the anti-symmetric point (zero current) for the profiles on the shell portion (the side regions) at the axial center point are consistent with those of 3 kV, both of which consist of the signal from the shell section only. The fact that the zero current point in the core region is not at the axial center of the NW is due to a difference in the contact resistance on the core that arises inherently from the annealing process.

6.6 Summary

In summary, we have spatially resolved carrier transport in a core-shell heterostructure nanowire with unprecedented high resolution and capability of sub-surface probing by energy variable EBIC. The coupling of unprecedently fine lateral resolution in current imaging with electron energy-based depth, guided by simulated electron trajectories, now opens the possibility of simultaneous nanoscale discrimination of carrier type and dominant transport mechanism selectively within different media in heterogeneous nanoscale electronic devices.

Nanowire growth and device preparation. GaAs/Al_{0.24}Ga_{0.76}As NWs used in this study are grown by Au-nanoparticle-catalyzed metalorganic vapor phase epitaxy (Aixtron) on 111(B)-terminated GaAs substrates. The growth of GaAs NW cores having diameters of 60 nm was carried out using (CH₃)₃Ga and (C₄H₉)AsH₂ as metalorganic precursors at a growth temperature of 400°C, and AlGaAs shells with thickness ranging around 70 nm were subsequently grown at 650°C with the addition of (CH₃)₃Al. Low temperature photoluminescence (PL) is used to estimate the Al percentage from shell band edge excitonic emission as previously reported⁷². The GaAs core is lightly *p*-typed unintentionally doped with carbon from the precursors. The AlGaAs shell is *n*-typed doped with Si. With overall nanowire diameter ≈200 nm, a SiO₂/Si substrate, and a moderate beam current of only 100 pA, the thermoelectric current by local heating from Seebeck effect is negligible and therefore excluded from the analysis⁷³. We used a multi-layer e-beam metal evaporation consisting of Pd, Zn, Ti and Au for Ohmic contract formation. The out-diffusion of Ga in the nanowire through Pd, activated by a rapid thermal annealing at 400°C, leaves vacancies for Zn to occupy and to form local doping under the contact area, which promotes carrier tunneling and reduces the contact resistance. The devices are defined with e-beam lithography (NPGS, Bozemann, MT) and the metallization process is conducted in e-gun evaporator (BOC Edwards). All devices are subject to gentle oxygen plasma cleaning for 5-15 minutes before measurement inside a field-emission scanning electron microscope (FEI DB235, Hillsboro OR) chamber to avoid residual carbon deposition in the vicinity of the beam.

Electron beam induced current. Data were conducted with a custom-built low-noise EBIC system (Mighty EBICTM, Ephemeron Labs, Philadelphia PA and Drexel University) installed on a scanning electron microscope (FEI DB235). A transimpedance amplifier was used to convert the current signal into a voltage. All measurements were done in a DC configuration. The substrate was held at ground, the beam current for all acceleration voltages used was ≈ 100 pA, and the dwell time at each pixel before measuring the signal was 0.5 ms.

Spatial drift and vibrational noise correction. To enable longer scan times for increased resolution, an algorithm was developed and implemented to remove drift and vibrational noise from the images. The procedure locates the center of the nanowire along the axial direction using the secondary electron image as a reference and computes the gradient for each line of the scan. The center is defined as the average of the positions of maximum and minimum values of the gradient. The data points are extracted around the center and repositioned.

Monte Carlo simulations. Electron flight paths through the GaAs-core, AlGaAs-shell nanowire were simulated using Casino3.2⁸. The simulation space was 200 nm by 200 nm by 100 nm with a grid spacing of 1 nm. The incident beam was scanned radially along the nanowire in 5 nm increments at beam energies of 3 kV, 5 kV and 10 kV. The number of carriers generated was estimated in the core and shell by dividing the energy lost at each point by $3E_g$ of GaAs and AlGaAs at 300 K.

Chapter 7: Bandbending in Ge nanowires

The dynamics of locally excited carriers, electrons and holes, in semiconductor nano-electronics, are integral to understanding and designing devices, particularly nanowire devices that interact with light. Efficient carrier separation through radial junctions for nanowire and nanorod based photo-voltaic cells^{47;74-79} and photo-detectors has been the subject of much interest.

Due to the large surface to volume ratio of nanowires, the effects of bandbending and surface states can dominate the behavior of a device, and have been shown to be diameter dependent and can be advantageous^{36;80;81}, or detrimental^{24;58} to the performance of a device. Surface states have been attributed to short diffusion lengths of minority carriers in Si nanowires²⁴. Surface effects can also lead to completely depleting the semiconductor channel⁵⁸. Bandbending from Fermi level pining at surfaces has been attributed to unexpected behavior in wide range of material systems from III/V⁵⁸, Si²⁴ and Ge^{36;80;82-84}, and ZnO nanowires^{81;85;86}.

Bandbending in Ge nanowire based photodetectors from trapped electrons at the surface leading to an accumulation of holes and parallel conduction paths for both electrons and holes has been shown to increase the sensitivity over larger Ge nanowires with less bandbending and is highly diameter dependent⁸⁰. It is well known that the Ge/GeO_x interfaces has trap states for electrons⁸⁷. This has been studied extensively using transport measurements. In bulk Ge the bandbending at the interface of Ge/GeOx has been studied using time dependent transport mea-

surements and has shown to have both fast and slow trap states^{88;89}, and similar results have been shown in Ge nanowires⁸³. The effects of bandbending is so strong that highly p-doped Ge nanowires, doping concentration and profile confirmed with atom probe tomography and are expected to have n-type behavior, surprisingly have a reduced conductivity compared to intrinsic Ge nanowires⁹⁰. Ge nanowire devices often exhibit hysteresis during transport measurements and are attributed to surface states^{36;83;84}. Different approaches have been used to understand the origin and methods of passivation those surface states^{84;91}.

Studying the effects of surface on bandbending has relied on a correlation of techniques and modeling to identify the root cause. This body of work has been overwhelmingly convincing that surface effects needs to be fully understood^{83;87;90} particularly with nano-electronics. Until now, there has not been a detailed study that can directly image the filling up of surface states and how the number of occupied states affects the formation of parallel conduction channels for electrons and holes^{80;81;86}. There is a growing consensus that surface states and their effects is one of the major contributing factors in the performance of nanowire devices.

In this chapter we present the results from Ge a metal-semiconductor-metal (MSM) nanowire device, where we directly image the evolution of bandbending as charges get trapped at the Ge/GeO_x interface depleting the wire and leading to change in the conduction mode from being limited by the barriers at the Schottky contacts to a ohmic type response from a higher concentration of holes. The effects of surface band bending on Ge nanowires has been well documented making Ge nanowires an excellent test bed for investigating new ways of studying the

evolution of bandbending and how it evolves as surface trap states are filled.

7.1 Experiment setup

In Chapter 5, we saw the results of applying bias to nanowire and the onset of impact ionization and permanent change in potential inside the nanowire. Often when testing these devices the current response changes with sequential applied bias.

In a series of EBIC scans at 0V bias, performed after a conditioning voltage sweeps, of increasing magnitude from 0.1 V to 5.0 V was applied to the nanowire, we captured the effects of the surface trapped charges and the formation of parallel conduction channels for holes and electrons. Trapped electrons at the surface cause an accumulation of holes in the outer radius of the nanowire. The center of the nanowire remains charge neutral. The formation of parallel conduction channels allows for the minority carrier(electrons) diffusion length to increase dramatically increasing from 100 nm to extending over the entire length of the nanowire.

In a Ge nanowire contacted Cr/Au contacts we expect the device to have blocking Schottky contacts. When conducting transport measurements the contacts and device are often conditioned from the current passing through the device. With sequential measurements the current following through a device can substantially increase with each voltage sweep. To understand how the character of this response evolves, a series of EBIC scans are taken in between transport measurements at 0.0 V bias. The Ge nanowire was never tested before this point with any transport measurements.

Each sequential voltage sweeps ranging from 0.2 V to 5.0 V. We measured the

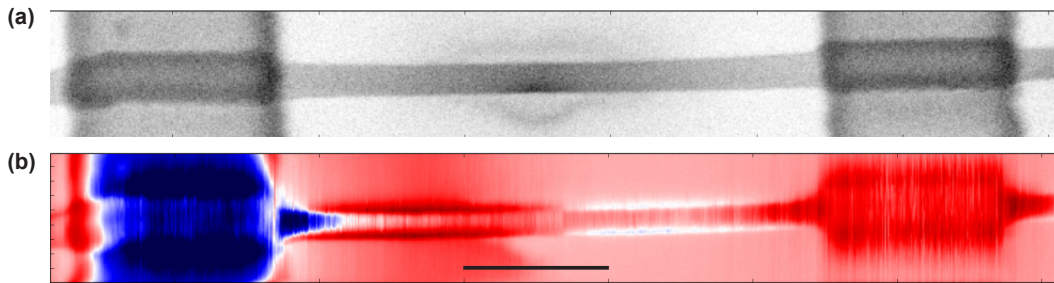


Figure 7.1: (a) Secondary image of Ge nanowire (b) EBIC image taken at 0 V bias, after a 5.0V voltage sweep showing parallel conduction channels for holes (outer shell) and electrons (center), scale bar is 500 nm. The spatial resolution of the scan is 5 nm.

current from each of these sweeps *in – situ* without the electron beam present. The voltage sweeps are bidirectional, going from 0 V to the maximum value and sweep back to 0 V. All the EBIC scans are done in DC coupling mode at 0.0V bias.

7.2 Transport Behavior

Transport measurements are taken in-situ with in the SEM with the beam blanked and DC coupled from the trans-impedance amplifier into the analog to digital converters(ADC). The response measured form the voltage sweep is the dark current response.

With voltages applied below 1 volt the response is exponential as we expect one contact to be forward bias while the other is reverse biased. Instead of the current saturating at higher voltages, the current takes on a ohmic type behavior. With sequential scans from 1V to 5V each scan sees a substantial increase in both current and hysteresis. Hysteresis in nanowires and devices is attributed to empty states at the nanowire surface capturing and releasing electrons^{36;83;84} and can have a fast

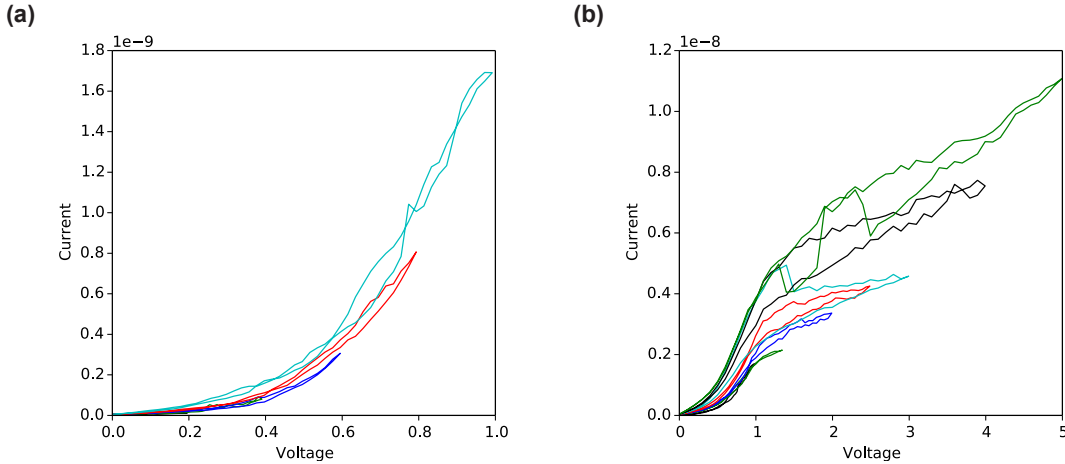


Figure 7.2: In-situ current vs. voltage sweeps of Ge nanowire inside the SEM chamber with the beam blanked(dark current response). Measurements are taken after EBIC scan held at previous voltage.(a) Voltage sweeps from 0.2 V, 0.4 V, 0.6 V, 0.8 V, and 1.0 V with EBIC scans taken after each sweep. (b) Voltage sweeps from 1.0 V, 1.4 V, 2.0 V, 2.5 V, 3.0 V, 4.0 V, 5.0 V, EBIC scans taken after each each sweep.

or slow time response. The hysteresis of higher voltage sweeps is much smaller when it is below 1 V and higher in ranges the nanowire has not been exposed to for prolonged periods. The DC current below 1 V continually increases with each voltage sweep.

This trapping of electrons at the Ge/GeO_x interface can locally accumulate more holes inside the nanowire. The nanowire is not intentionally doped and we assume it is p-type. The sign of the current response in the depletion region at the contacts, confirms the electrons are the minority carriers, as discussed in Section 7.3. To understand the origin of the hysteresis and the nature of the conduction channels, we turn to the EBIC images taken in between the progressive voltage sweeps.

7.3 Evolution of Surface States

Examining the EBIC images as we progress to higher biases applied in the voltage sweeps we observe two different behaviors emerge. In the center of the nanowire we observe the expected behavior form a p-type MSM device, black lines in Figs. 7.3 and 7.4, where we have electrons, the minority carrier being collected by the depletion region at the contacts with a negative current at the cathode, electrons following into cathode, and a positive current at the anode, electrons following into the anode contact. In the first EBIC image taken at 0V bias before any voltage sweep is applied, band bending is not present in the middle of the nanowire. We can clearly see the depletion region from the junction with the metal contact and the diffusion length of electrons at the measurement side. The depletion region at the other contact is much less visible. Most of the wire is neutral and no fields are present away form the contacts. After lower voltage sweeps the side profiles match that of the center profiles. At higher biases however, the side profiles have the response of an ohmic response due to local carrier injection³, where the local generation of charges creates a potential difference and carriers created here have both a drift and diffusion component.

Imaging after higher applied voltage sweeps, we can clearly see that this portion of the nanowire has response is that of an ohmic device, and that most of the potential drop is at the metal contacts and does not extend into the nanowire channel. That the potential drop is greatest at the contact is evident in Fig. 7.1(b) where the strongest response is observed underneath the metal contacts, even though the spatial resolution in this region is degraded from increased scattering of the e-beam

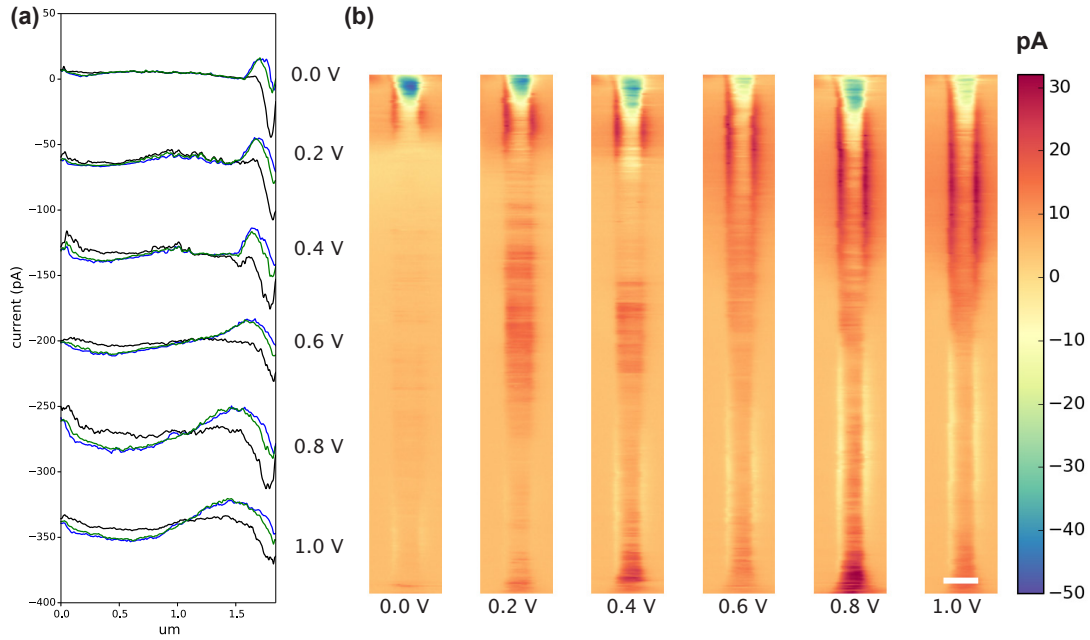


Figure 7.3: EBIC images from scans after 0.0 V to 1.0 V sweeps applied . (a) Sequence of EBIC profiles along the left side(green), right side(blue) of the Ge nanowire axis, profile from the center. Profiles are offset by 75pA for each scan. The profiles extracted from EBIC images (b). (b) Scale bar for EBIC images is 100 nm.

from the Au contacts.

As higher voltages sweeps are applied the nanowire, and the EBIC scans in between we begin to see more of the nanowire respond from the beam. Both the center and side profiles converge in the middle of the nanowire scan after the 0.2V sweep. During this applied scan we begin to see more bandbending close to the contacts but just outside of the depletion region of the MS contacts. Due to the depletion region at the MS contacts, electrons are collected and do not have a chance to fill surface states. This trend in the EBIC scans continues from 0.4V to 0.6V sweeps where the side and center profiles along the nanowire axis diverge. The regions with trapped electrons at the surface start from the contacts both anode and cathode and after larger voltage sweeps are applied move towards the center of the

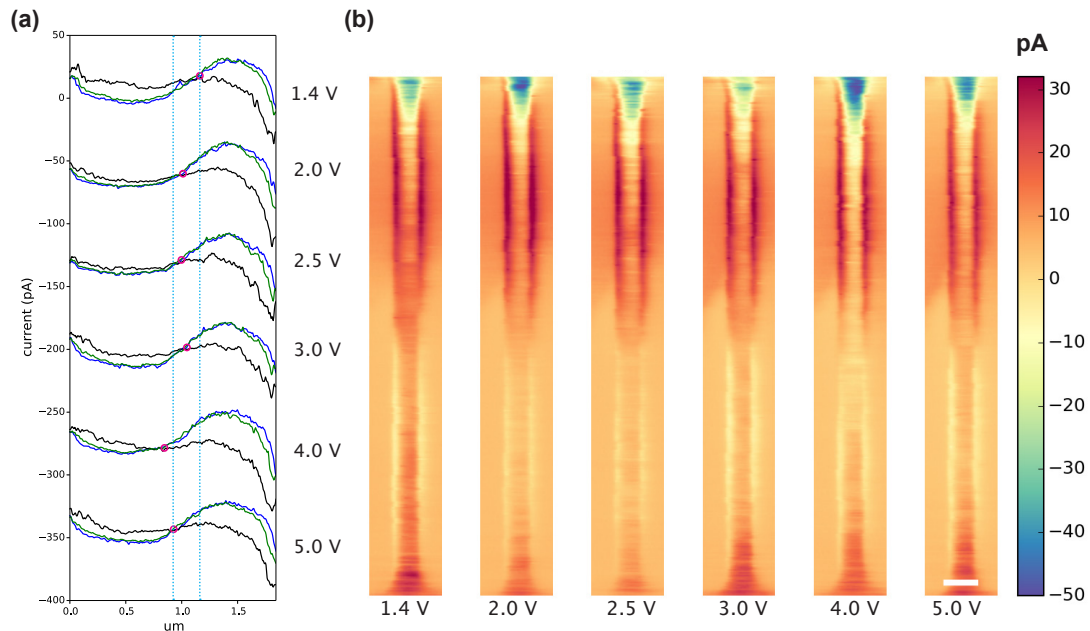


Figure 7.4: EBIC images from scans after from 1.4 V to 5.0 V sweeps. (a) Sequence of EBIC profiles along the left side(green), right side(blue) of the Ge nanowire axis, profile from center (black). The cross over point for where the center(black) and side profiles(green, blue) diverge is denoted with magenta circle. The first cross over point(after 1.4 V sweep) and the last(5.0 V sweep) are marked with cyan dashed lines. Profiles are offset by 75pA for each scan. The profiles extracted from EBIC images (b), scale bar for EBIC images is 100 nm.

nanowire.

The character of the center profile from scans after 0.8V to 5 V sweeps is due to the diffusion of electrons towards the MS contacts. The side profiles shown in blue and green from 0.8V to 5V in Fig.7.3 and Fig.7.4 show the evolution of bandbending in the nanowire as progressively greater voltage sweeps are applied to the device. The point where the center an side profiles are equal value is a crosspoint is dependent on the local difference between the two signals. Overall, with progressive scans this crosspoint tracks to the anode. When the difference is greater at the cathode then at the anode, the point shifts further to the anode 2.0V and 2.5 V sweeps. When the local difference between center and side profiles at the anode becomes more balanced the cross over point shifts slightly back 3.0V sweep. This pattern repeats after the 4.0 V sweep when the cathode side difference is greater and then shifts back once the anode side becomes more even.

7.4 Carrier Generation Profile

To understand the origin of the two different characteristic behaviors observed, an ohmic response on the sides and Schottky in the center of the nanowire, we need to consider the interaction volume and generation of carriers in those regions. That the Ge nanowire is not intentionally doped and it is not a core/shell geometry, means another effect must be present to cause this behavior. Generation of carriers can be estimated using Monte Carlo simulations of electron trajectories through the Ge nanowire. All measurements are conducted using a 10kV electron beam. The cross sections represent the total energy dissipated in the nanowire from the beam. In the simulation we take into account the density of Ge. The total number of carriers

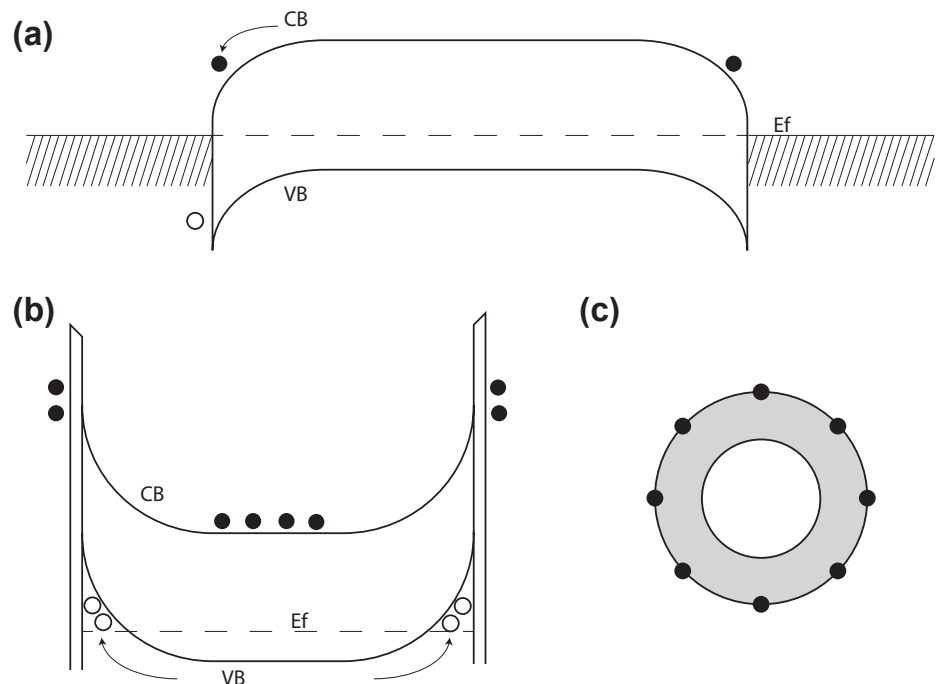


Figure 7.5: (a) Band diagram along the axis of the Ge nanowire depicting the depletion region due to the Schottky contacts at either end. (b) Band diagram in radial direction in regions away from Schottky contact, shows electrons in traps at the surface (black dots), and holes open circles accumulating near the surface of the nanowire. (c) illustration showing the depletion in gray

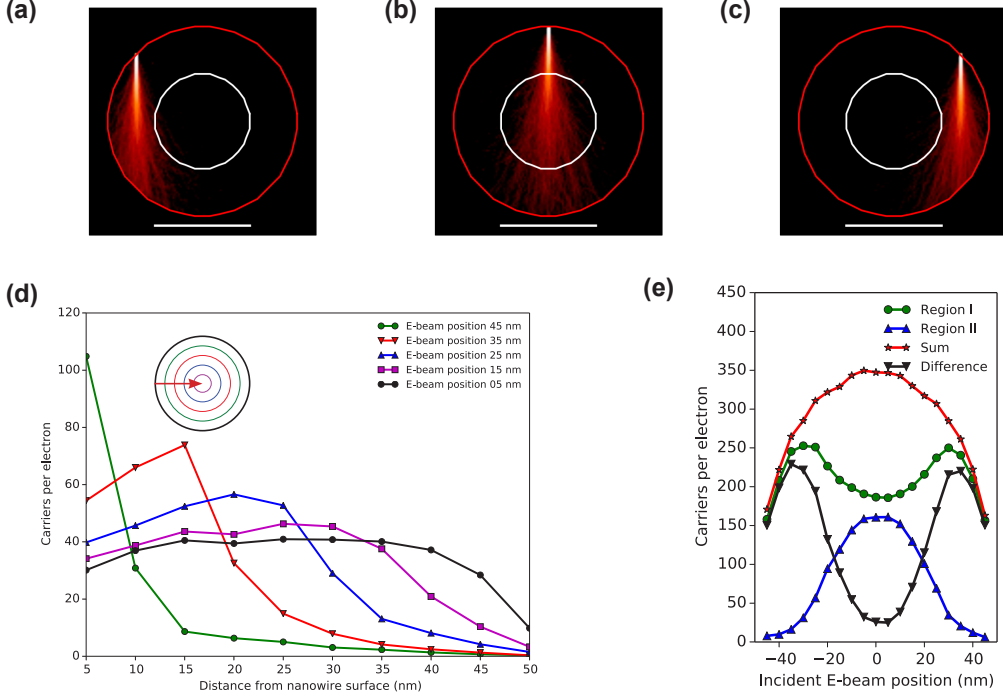


Figure 7.6: (Monte Carlo electron flights simulations of 1000 electrons at -40 nm (a) , 0 nm (b), and +40 nm(c) beam positions. (d) Radial distribution of carriers generated from beam positions 45 nm to 5 nm, with 50 nm the center of the 100 nm nanowire. (e) Simulated cross sectional profiles, total Δn , Δp created per incident electron within the nanowire moving the incident beam position 5nm for each point in the depleted zone region I(green) and the neutral zone region II(blue). Also plotted are the sum(red) of the two regions and the difference (black).

both Δn and Δp can be estimated using Eq.7.1.

$$\Delta n, \Delta p = \frac{Ed}{3Eg} \quad (7.1)$$

The shape of the interaction volume is highly dependent on both the incident energy and the geometry of the sample. The difference of the response from the sides and the center leads us to believe that the outer portion of the nanowire has its bands bent and is in a mode of hole accumulation. To match this response, we split the nanowire into different regions. One is bounded by an outer radius of from

50 to 25 nm our estimate of the extent of the depletion region. The second is the inner 25 nm that we expect to be charge neutral. We performed a series of electron flight simulations with different incident beam positions in 5 nm steps from -45nm to 45nm with zero indicating the center of the nanowire.

We consider the distribution of carriers in the radial direction for beam position for 45nm to 5 nm in Fig.7.6(d). For scan positions of 45 nm and 35 nm the number of carriers generated drops significantly at 10 nm and 20nm from the nanowire surface. For scan positions from 25 nm to 0 nm the distribution flattens out with 5 nm beam position having a even distribution of carriers in both regions. Integrating the total number of carriers generated in each region we can produce simulated profiles orthogonal to the nanowire axis, Fig.7.6(e). The profile can range in shape from a sum of all the carriers generated in both region I and region II or the difference of the two signals, we observe both extremes in the Ge nanowire. Given that the observed EBIC current is much smaller than the DC component confirms that the EBIC measurement is taking place in low injection mode.

7.4.1 Profiles across the nanowire axis

The nature of the signals is due mainly to holes in the outer region close to the surface and electrons in the neutral region, and at the MS contacts we expect to have a difference of signals for most of the wire. At zero bias the Ge nanowire has almost no response outside of the MS contact region. From the EBIC scans after 0.2V to 0.6 V sweeps the middle portion of the wire is transitioning from a sum of signals to a flattening of the signal in the center. The region just outside of the depletion region from the MS contacts has the strongest signal of bandbending and

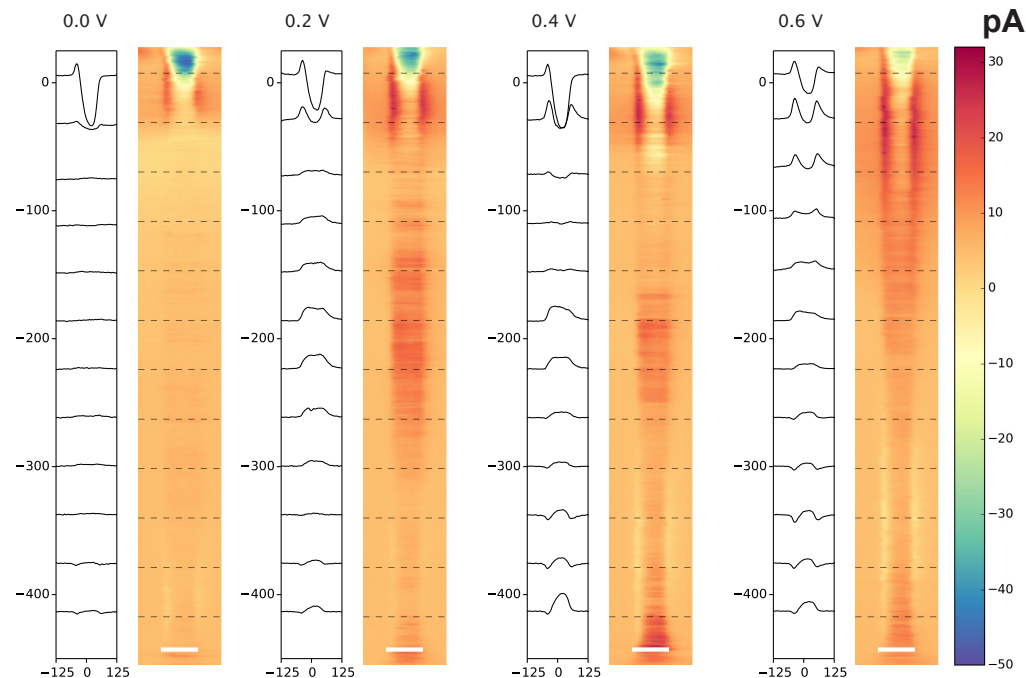


Figure 7.7: Cross-section profiles and EBIC images after 0.0 V to 0.6 voltage sweeps, taken at 150 nm intervals across the nanowire axis from corresponding EBIC image and voltage bias profiles are offset -37pA for each interval the dash lines denote the section of the image plotted in profile. The scale bar in the EBIC images is 100nm. The all units are in pA

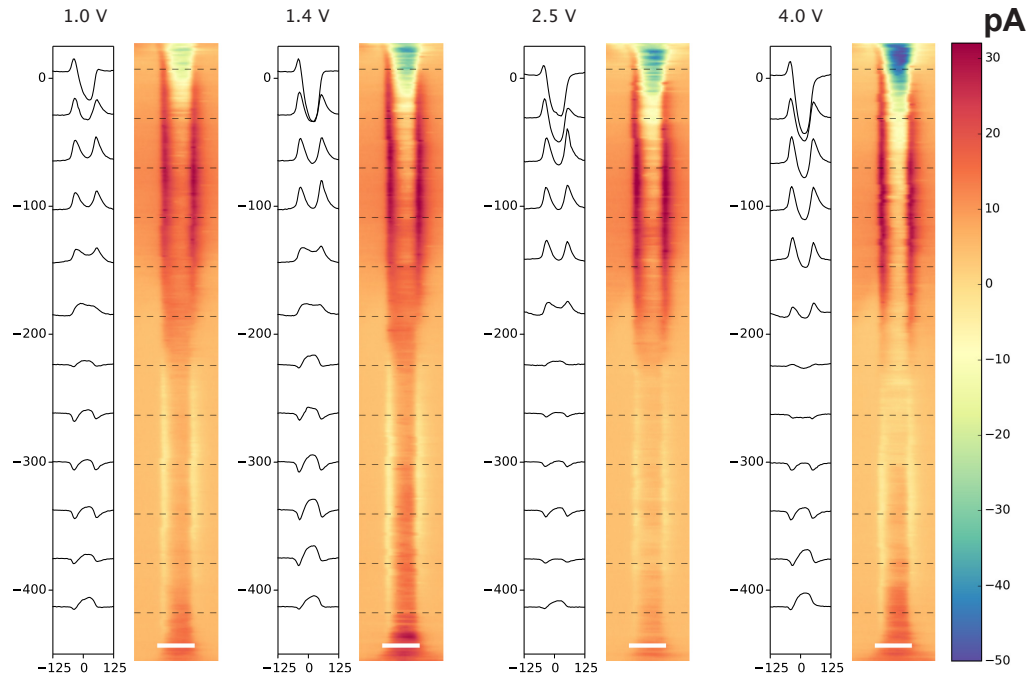


Figure 7.8: Cross-section profiles and EBIC images taken after voltage sweeps from 1.0 V to 4.0 V, taken at 150 nm intervals across the nanowire axis from corresponding EBIC image and voltage bias profiles are offset -37pA for each interval the dash lines denote the section of the image plotted in profile. The scale bar in the EBIC images is 100nm. The all units are in pA

matches the simulated difference profiles that we expect from the hole and electron components. From either contact after the 1.0V to 5.0 V sweep we can clearly see this transition continue until they meet in the middle of the wire, and there is now a continuous conduction channel for both electron and holes.

7.4.2 Summary

We have shown the relation of surface trap states filling and the transport behavior in the Ge nanowire device. As more surface states contain electrons there is greater hole accumulation in the region below the surface of the nanowire as the whole nanowire has bend-bending and an accumulation of holes throughout the device the

current beyond 1V for each sequential voltage sweep goes up substantially. Through Monte Carlo simulations, we have confirmed the shape of the side profiles and have an estimate for the number of carriers created in both the neutral region and the accumulation region below the surface we have estimated that this is region approximately 25nm from the surface.

The outer region with an accumulation of holes leads the sides of the nanowire to exhibit the response ohmic nanowire. We first observe this transition at biases above 1 V from the profile scans it is evident that more electrons have been trapped at the surface effectively lowering the resistance of the device.

The hysteresis in the transport measurements corresponds to a shift in the location and number of holes in the accumulation region. Looking at the extracted profiles along the side of the nanowire in the direct of the axis we observe the shift of the cross over point and along the beam axis we have seen the cross sectional profiles and how they become much more pronounced. Finally, we show the origin of why surface bandbending can create gain in Ge nanowire based photodetectors and measured a increase of the minority carrier diffusion length from 100 nm to extending throughout the nanowire. This work represents the first time surface bandbending has been directly imaged in a nanowire using EBIC. The techniques demonstrated here can be applied to all radial junctions and hetero-structures in nanowire based devices and greatly enhance our understanding how these devices behave.

Chapter 8: Local probing of Si MIS nanowire devices

In this chapter we look at the response of a Si nanowire Schottky device we explore the region underneath an extended contact that is purposely electron transparent to probe the behavior underneath the contact with nanometer resolution. In the Ge MSM device in Chapter 7, we found the strongest response was the area underneath the metal contacts. Due to the thickness of these contacts the electron beam scatters and has a much larger interaction volume with the sample, limiting the spatial resolution. The other limitations to working with VLS grown Ge nanowires is that the doping level is hard to control as well as the doping distribution⁹⁰. It is well known that the native oxide in Ge isn't stable and can trap charges, we explore this in detail in Chapter 7.

To understand the dynamics of the behavior at the MIS junction, we designed a test structure that would be well suited to answer these questions. We choose to work with Si nanowires that are etched from a wafer using the MACE process, explained in Chapter 4.2. These provide us a simpler system to work with in that we can have a known doping concentration and type, a single crystalline and orientation, and Si oxide, which is much more predictable than the Ge/GeO_x interface and more widely studied.

8.0.3 Test structure

The test structure for the MIS required that we have an electron transparent contact. We choose aluminum as the contact material, as it scatters the electron beam to the

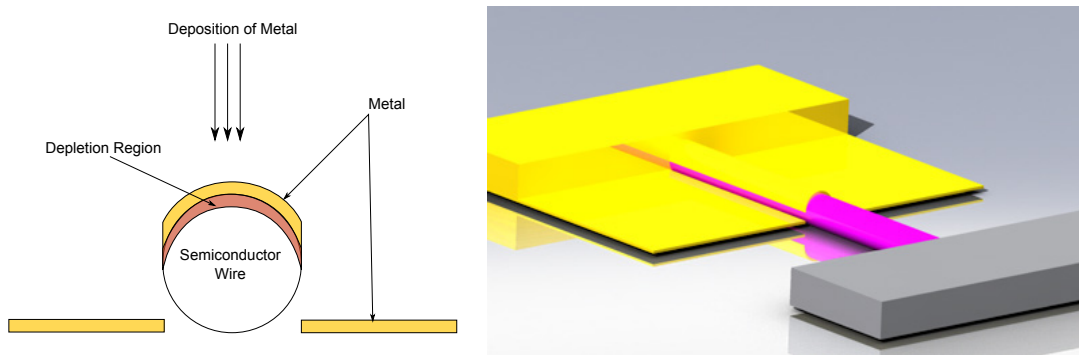


Figure 8.1: Side view of MIS test structure Schottky contact is shown in yellow, deposition of metal is directional and not continuous for thin extended contact that is electron transparent. Si nanowire is shown in pink, with ohmic contact in grey.

same extent as Si and we can have a far smaller probe size and maintain control over the interaction volume. The thickness 12nm of the Al contact was chosen so that it was continuous, but sufficiently thin to minimize scattering in the contact. The MIS contact was sputtered on to a window on the substrate. Sputtering provides a more conformal thickness on the material and if the using multiple sources and rotating the sample. We provided two ohmic contacts to the device to test only the transport behavior in the nanowire.

8.0.4 EBIC of MIS nanowires

The EBIC results of the MIS Si nanowires show that we have not made Schottky diodes as originally intended, instead we have the response of a MSM device. We will examine these results and what they can tell us about the processing of these devices, and identify opportunities to improve device performance. This is one of the key applications of EBIC analysis, process discovery and validation.

If the sputtered Al contact was continuous, and created a junction at the nanowire

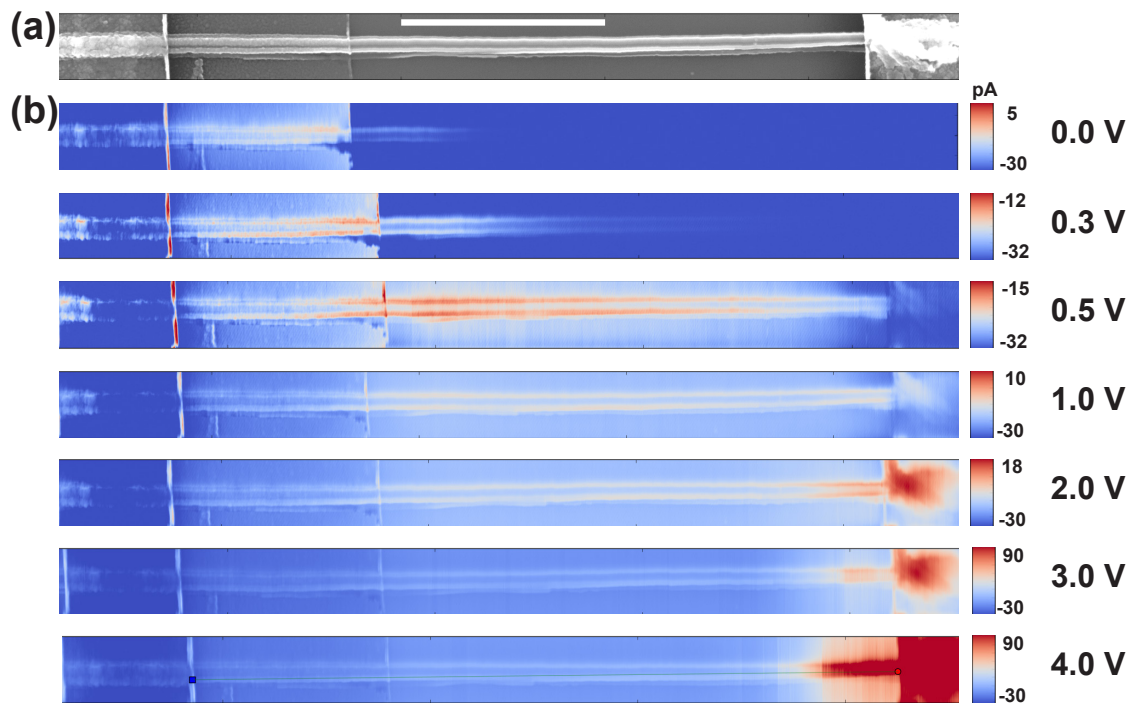


Figure 8.2: (a)Secondary electron image of p-type Si nanowire with sputtered aluminum contact and evaporated contacts,A thicker 120 nm evaporated contact goes over the sputtered Al contact to maintain electrical continuity form the top of the nanowire to the electrode contacts, scale bar is $2\mu m$. (b) Progressive EBIC scans from 0 V to 4.0 V bias. The left contact is the cathode the right contact is the anode. Acceleration voltage of the e-beam is 10kV, probe current is 100pA

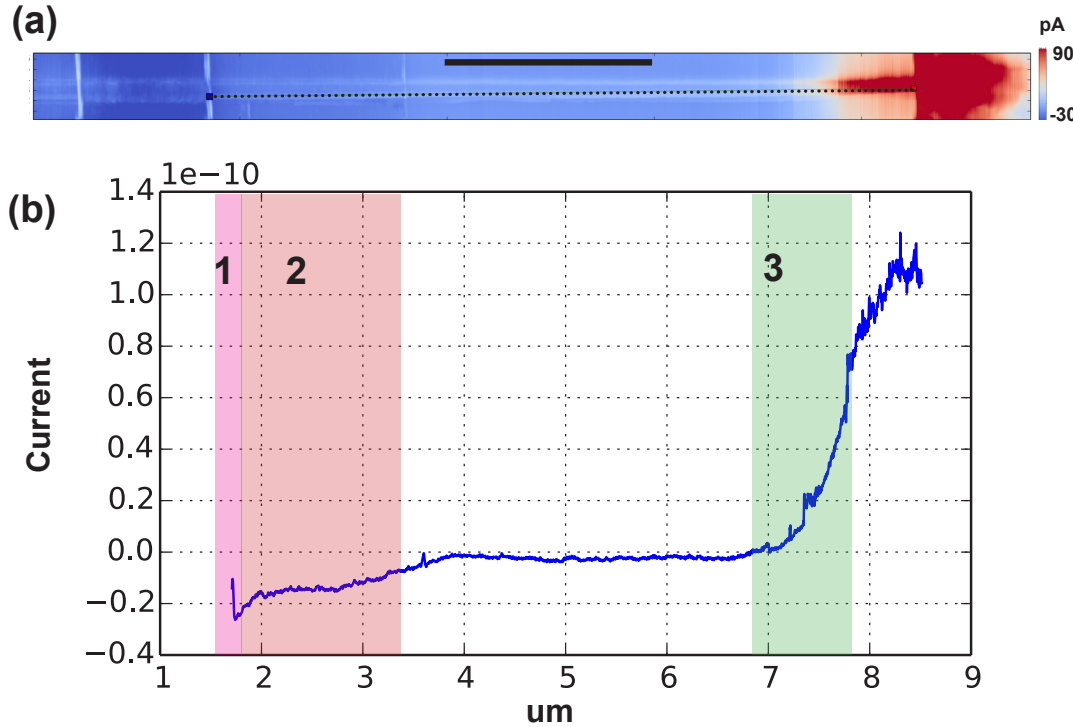


Figure 8.3: EBIC image of Si nanowire Fig. 8.2 with extracted profile(a) 4 V bias applied to device, scale bar is 2 μm . (b)extracted profile from (a) along dashed line. Region 1,2 underneath MIS contact of sputter 12nm Al. Region 1(pink) denotes where diffusion length near cathode. Region 3(green) drift/diffusion length from anode.(a) and (b) are aligned to extracted profile.

surface, the area underneath the sputtered contact should have the highest response. Additionally the oxide thickness on the Si nanowire could still be to thick on the nanowires measured, making the barrier height to high to create a rectifying junction. The oxide is native on these nanowires. At 0 V only the EBIC response at the MIS contact and extending 1 μm into the nanowire is observed, Fig. 8.2. The whole nanowire doesn't have a response until 0.5 V bias is applied.

With an applied voltage bias of 2.0 V and above we start to see an depletion region at the anode of the device, and a diffusion of electrons (minority carrier). Looking at an extracted profile along the side of the nanowire from the evaporated

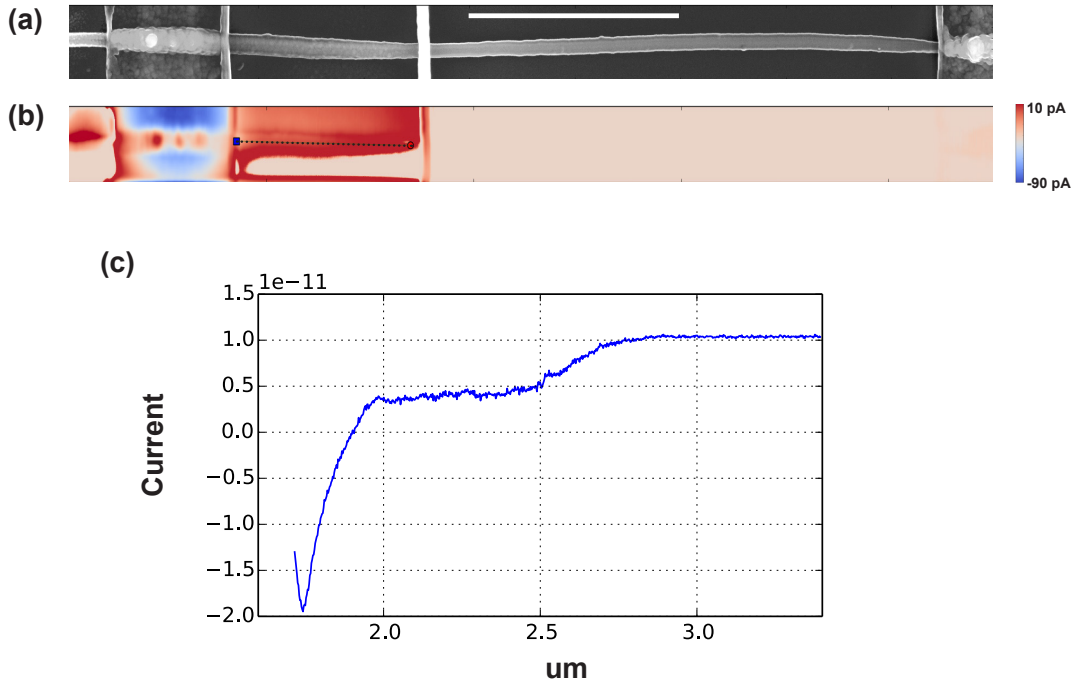


Figure 8.4: SE and EBIC images collected from Si MIS NW device at 5kV.(a)SE image, scale bar $2\mu m$. (b)EBIC image (c) Extracted profile from (b) dashed line signal from MIS contact.

contact at the cathode, Fig.8.3(b) with a applied bias of 4 V, we see the diffusion length of electrons from that contact in region 1. In region 2, under the MIS Al contact there is an EBIC response from $2 \mu m$ to $3.5 \mu m$, the thin Al contact appears to have modified the fields inside the nanowire underneath the contact. From $7 \mu m$ to $8 \mu m$ we see a characteristic shape of a depletion region at the anode and the diffusion length of electrons flowing into the anode. The nanowires measured with EBIC were not annealed, which is a requirement for forming an ohmic contact, where bonds between the metal and semiconductor need to be made. The response at the anode is that of a blocking contact. From EBIC scans from 1 V to 4.0 V we can see the response change as the contacts are conditioned from current following through them.

To understand the signal from underneath the MIS contact we examine a separate nanowire at a incident beam energy of 5 kV, Fig. 8.4(b). At the cathode at the edge of the evaporated contact on top of the thin Al extended contact we see the same diffusion length. From $2\mu m$ to $2.5\mu m$ the response on the extracted profile is flat, until it transitions again. This is the same response of the profile shown in Fig.8.3(b) in regions 1 and 2. It is clear that the thin Al contact modifies the surface and E fields of the nanowire. The nanowire doesn't respond to the e-beam outside of this region. That the diffusion length is much shorter and signal level is much lower at the cathode is a result most likely of a oxide that is to thick to make rectifying junction and limiting the current that passes through the device. Annealing is important for forming ohmic contacts, but is also key to forming a Schottky contact and can lead to better device performance and less interface states and higher barriers.

An applied voltage bias also effects the response underneath the MIS contact, As we saw with the other MIS Si nanowire devices, the anode is conditioned from applying a voltage bias. This conditioning allows a conduction path for electrons out of the nanowire. Line profiles extracted from EBIC scans at 0V and 6 V, Fig. 8.5 show a transition at the edges of the nanowire, where we know from Chapter 7 are more likely to have band bending, from a less negative response compared to the background signal to a positive current. The left side of the nanowire has a stronger response to the beam in both sets of profiles. The profiles of the 6 V scan also show the response from right edge of the nanowire as well.

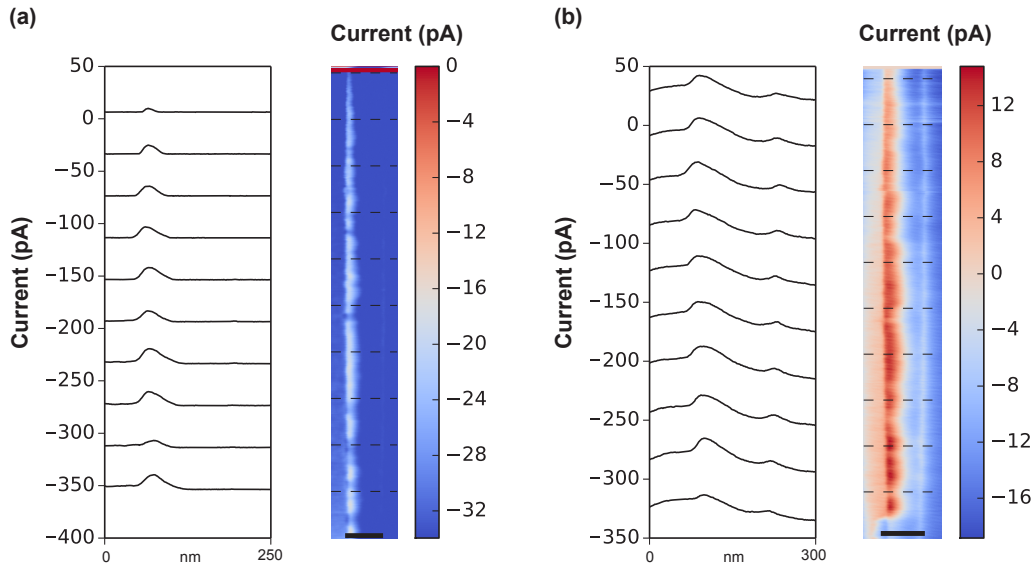


Figure 8.5: EBIC images under MIS contact of Si nanowire with extracted profiles denoted by dashed black lines(a) 0 V bias, scale bar 125 nm. (b) 6 V bias, scale bar 150 nm. EBIC profiles are offset by -40 pA and are extracted from EBIC images at the dashed lines.

8.0.5 Summary

We have shown that the quality of the oxide and thickness is the limiting factor in making MIS nanowire devices. The active area of the device primarily at MIS junction and not in the channel of the device which had a flat response. The variations observed underneath the MIS contact are likely due to an uneven oxide thickness. The evolution of the depletion region at the anode is the result of the contact being conditioned from current following through the device. Before the anode was conditioned it was highly blocking. The observed signal level difference at the MIS cathode and anode indicates that the oxide was successfully etched before the anode contact was put down, but still formed a blocking contact even though Al is a p-type dopant because of interface states a lack of bonds between the metal and the semiconductor. To improve on the quality of the device an annealing process and

growth of a low interface trap density oxide layer are needed.

Chapter 9: Applications to Other Systems

In looking beyond semiconductor nanowires, there are many other devices and material systems that we can investigate with EBIC. The increased resolution and sensitivity we have demonstrated presents an opportunity for far more in depth analysis than is possible with other techniques.

In this chapter we will highlight results from electron beam absorbed current (EBAC) using a single contact and resolving domains of ferroelectric materials BFO and PZT. These domains are normally imaged with piezo-force microscopy (PFM), our results have a direct correlation to PFM measurements.

We introduce applications of EBIC to 2D semiconductor materials, namely MoS₂. With sheets of materials and junctions that are only one or two mono-layers this material class represents an limit in the thickness of interfaces. While most materials used in semiconductor devices at reduced dimensions it is necessary to consider the effects of termination of surfaces, in the case of 2D materials the material is the interface. The task of understanding these materials is well suited to EBIC because the interaction volume is limited to a single mono-layer and resolution will be unparalleled due to a lack of the beam spread from scattering events.

Finally we investigate depletion region of a PN junction in a commercial Si solar cells. EBIC has been used extensively to investigate defects in solar cells and to characterize junctions. However, due to the limitations of most EBIC measurement systems in that they have limited sensitivity and dynamic range there is much infor-

mation that goes missing. The results we show not only image the depletion region and the diffusion lengths of the minority carriers, we show a superimposed signal due to local variations in doping and how dopants interact with each other.

9.1 Electron Beam Absorbed Current

Anisotropy in the crystal structure is one mechanism in bright field contrast in transmission electron microscopy (TEM)⁹². Anisotropy is also seen in backscatter electron signal⁶. The simplest way to approach this is to see that changing the orientation of the crystal changes the probability of scattering events. We propose that this net difference in scattering events effects the absorbed current when imaging materials outside of depletion regions. The results in this section are comparable quality to broad view TEM and represents a non-destructive alternative to imaging with TEM.

9.1.1 Bismuth Ferrite

Bismuth Ferrite (BFO) is a ferroelectric material with domains where the cation and anion displacements result in polarization in the lattice along a set of directions. Originally we intended to measure EBIC response of the potential across domains with two electrodes parallel to the domain walls. This was demonstrated with exposure to light of having very large photo-voltages. Due to extremely high leak currents we were not able to get a EBIC signal. We then removed one of the contacts and imaged again, measuring the electron beam absorbed current. What we found was domains in the material.

In this imaging mode the transimpedance amplifier is replace the system ground

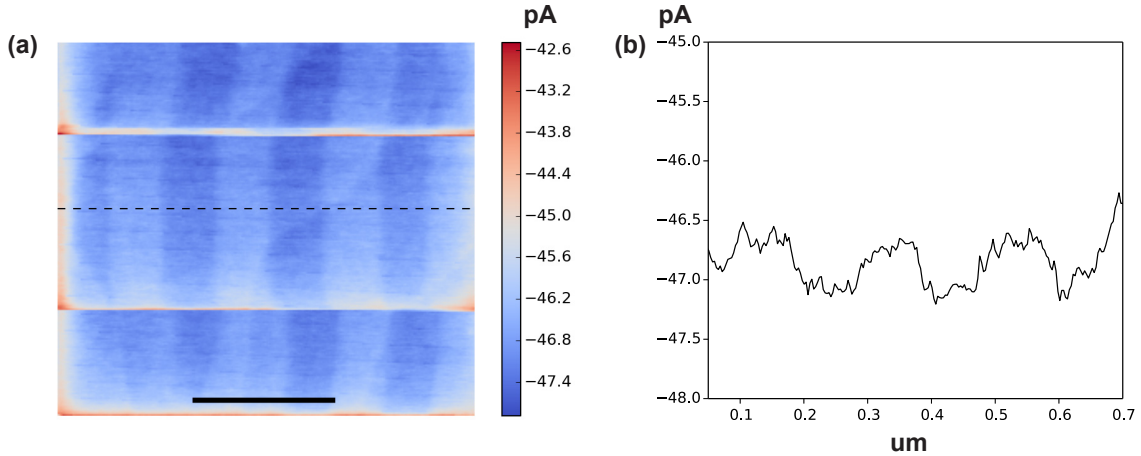


Figure 9.1: (a) Bismuth Ferrite Domains imaged by EBAC, scale bar in 250 nm. (b) Profile extracted from (a) orthogonal to domain orientation denoted by dashed line. Signal level is less than 0.5 pA between domains

of the SEM, where it can source or sink current to maintain charge neutrality. The signal level between domains is only 0.5 pA from peak to peak, Fig. 9.1. The number of electron-hole pairs generated is still the same in the material in EBAC mode however there is no separation of carriers so that recombination dominates. The observed signal is from local differences in the generation and recombination rates. Crossing the domains is the atomic step height from the STO substrate.

Samples with similar structures were imaged using both PFM and later pulled out and imaged with TEM showed dynamic switch on domains using bright field contrast⁹³. TEM is regularly used to investigate BFO and other ferroelectric materials such as PZT⁹⁴.

Carbon deposited on the sample from hydrocarbons in the SEM diffusing to the beam decomposing, does cause an offset in the amount of current being absorbed. This offset however doesn't change the relative difference in absorbed current between domains, Fig. 9.2.

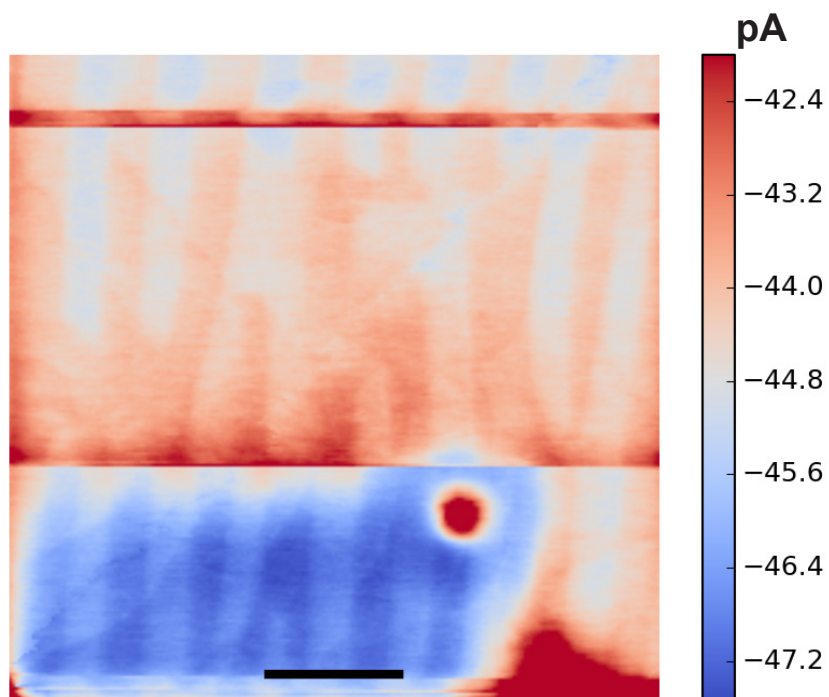


Figure 9.2: Carbon contamination from overlapping scan blue area as an offset compared to red area. Contrast mechanism does not change, scale bar is 320 nm.

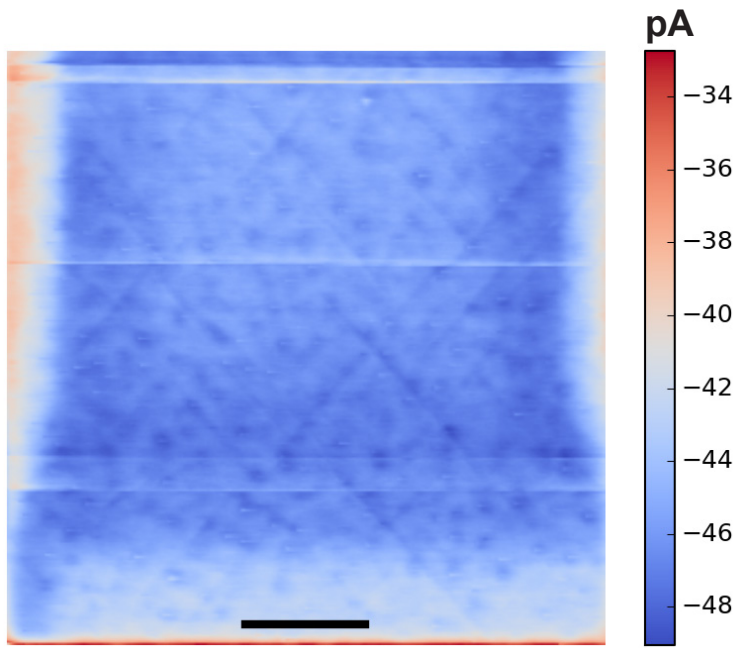


Figure 9.3: EBAC of PZT A and C domains are visible ,scale bar is 540 nm, acceleration voltage of 5kV

9.1.2 Lead Zirconate Titanate

In a PZT sample grown by MBE, in the absorbed current mode we see c domains that are needle like that are surrounded by a domains. The scan direction is at a 45 degree angle to the c domains, Fig. 9.3. As we take a closer look at the domains in Fig.9.4, there appear to be defects in the crystal material that are all orientated the same way and have three points separated by 120 degrees.

These results are preliminary, but could result in an imaging mode that could have broad application to a wide range of materials. The obvious progression of this work is to tilt the sample and see if the contrast does indeed change.

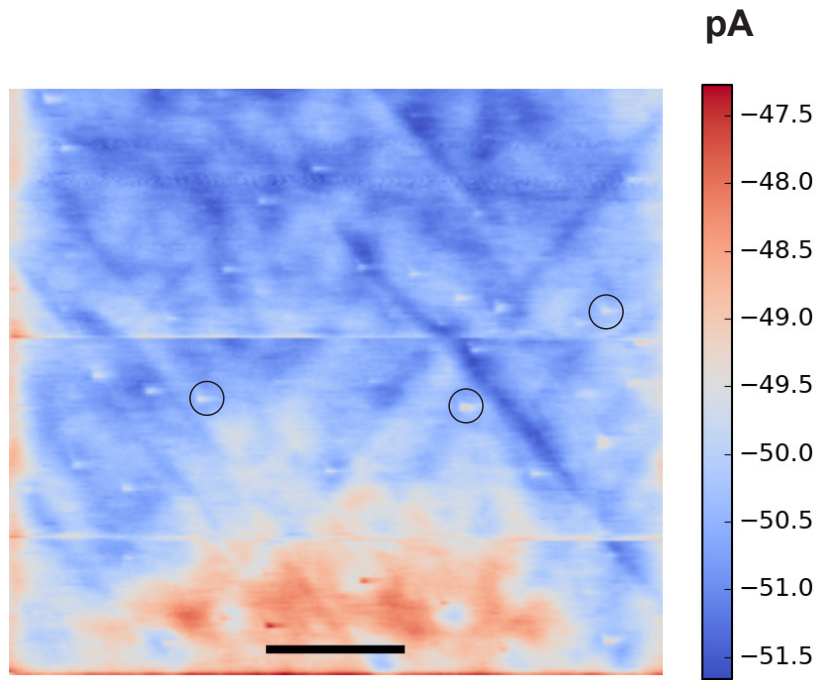


Figure 9.4: EBAC of PZT both A and C domains are visible, with triangular defects with the same crystallographic orientation, scale bar is 240 nm.

9.2 2D Materials and Devices

With the discovery of graphene⁹⁵ numerous analogous single mono-layer semiconductor materials have been investigated as transistor materials. Molybdenum disulphide has attracted considerable attention in that it is analogous to graphene but it has a bandgap in the visible⁹⁶. MoS₂ transitions from an indirect semiconductor for more than 2 layers to a direct bandgap semiconductor with one monolayer.

In both Fig 9.5. and Fig. 9.6, we can trace layers of MoS₂ as they go underneath one another. Ripples resulting in the deposition process of the MoS₂ onto the wafer, from the same mechanical cleaving process used to isolate graphene (scotch tape

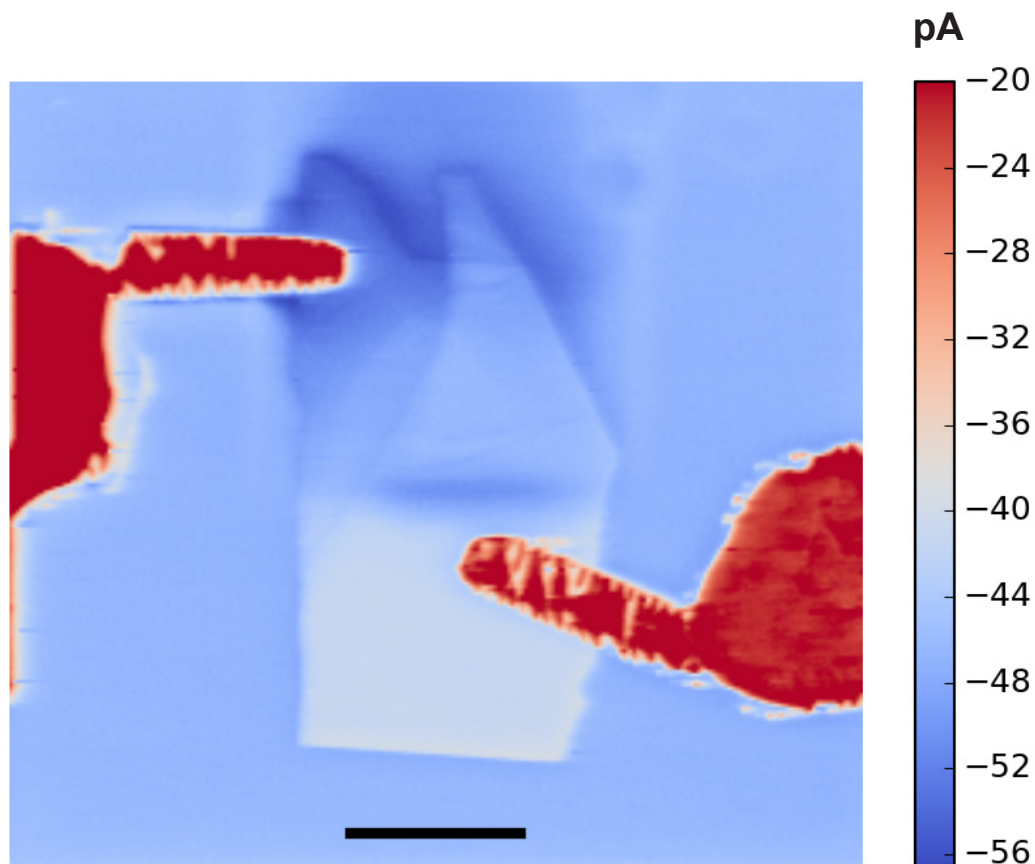


Figure 9.5: EBIC response of MoS_2 device with two electrodes at 0V bias, the sample has multiple layers that overlap, scale bar is $1.5 \mu\text{m}$

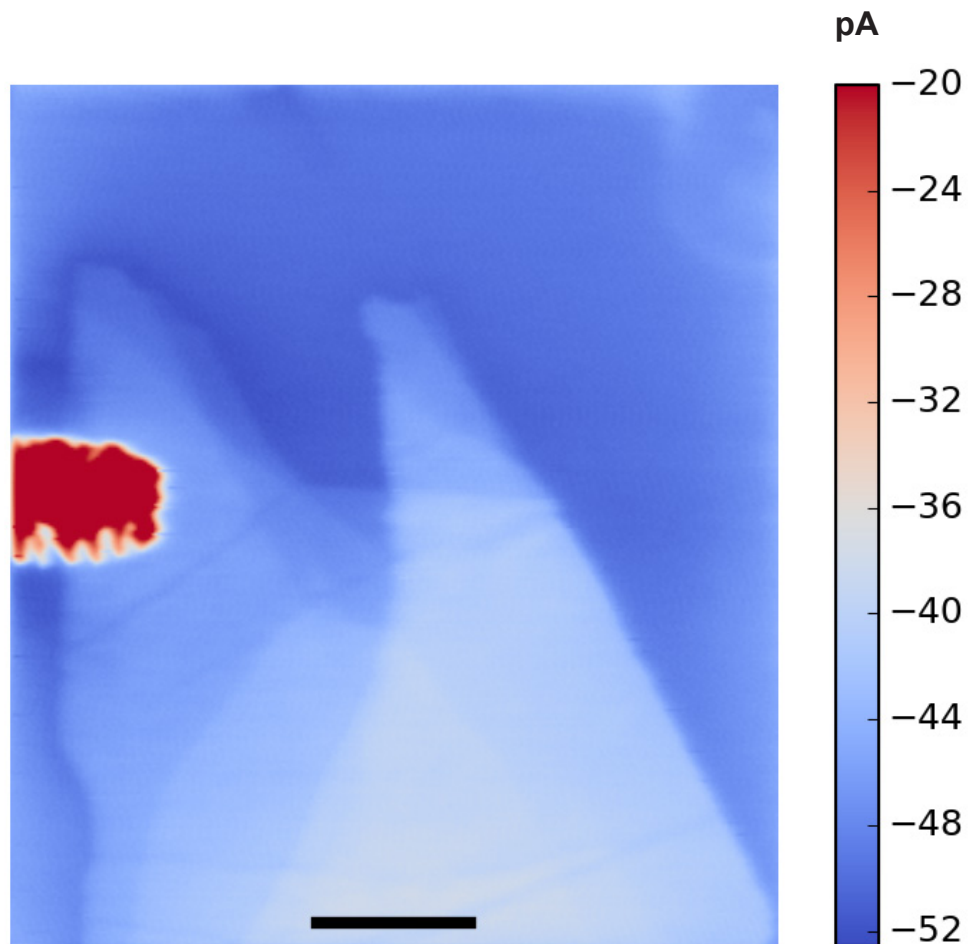


Figure 9.6: Higher magnification scan showing one electrode of MoS₂ device at 0 V bias. Interfaces between layers are visible in EBIC mode as well as folding of layers., scale bar is 620 nm.

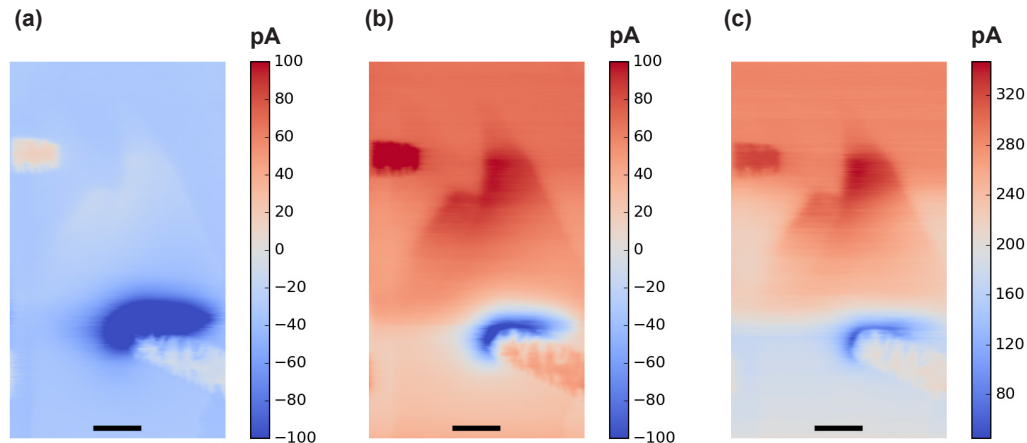


Figure 9.7: Multi layer MoS₂ device with Cr/Au contacts (a) 1 V bias (b) 3 V bias (c) 5 V bias. Scale bars are 620 nm.

method), are also evident in these scans.

When applying a bias to the material we see a depletion region form near the anode contact. With a greater applied bias, the response goes from a both positive and negative current below 3 V to all positive at a bias of 5 volts.

As with the nanowire devices, in MoS₂ we can perform EBIC studies with voltages applied and evaluate the quality of the contacts and behavior of carriers within the device and how they are modulated by local variations.

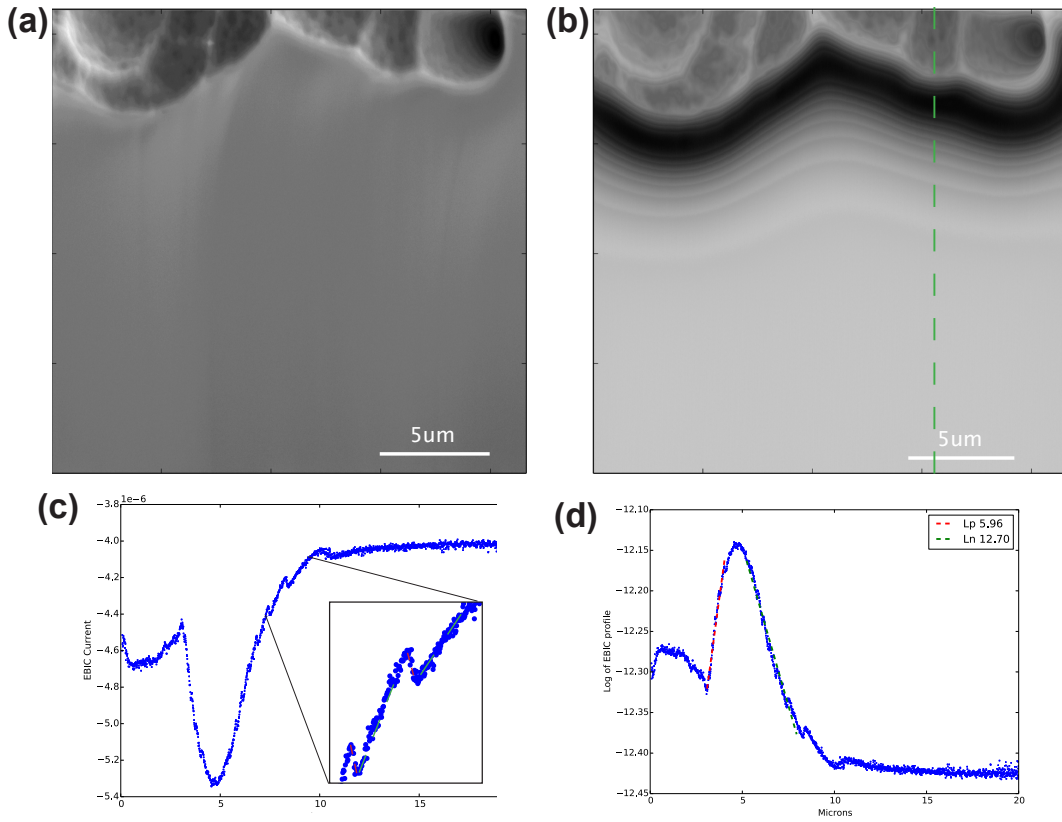


Figure 9.8: Cross section of Si solar cell p-type substrate with n-type top layer simultaneous sampling of SE and EBIC (a)SE image, scale bar 5 microns(b)EBIC image, scale bar 5 microns, green dashed line shows position extracted profile.(c)Extracted profile from (b), inset shows close up profile of ridges due to doping profile(d) natural log of (c) (inverted) with least squares fit L_P , dashed red line and L_n dashed green line on either side of depletion region.

9.3 Solar Cells

EBIC has been used in measuring the cross section Si PN junctions for some time^{10-12;14-16}.

Normally the depletion region extent and the diffusion lengths of the minority carriers is the main focus of EBIC measurements. In this case we demonstrate that there is far more information than was previously assumed. This can be attributed entirely to the increased dynamic range of the Mighty EBIC system.

We imaged a cross section of a micro-cleaved Si solar cell with EBIC and SE

image simultaneously at an acceleration voltage of 5 kV. In Fig.9.8(b) there are a number of bands that are evident outside of the depletion region on both the P side and N side. These bands are periodic when we look at a extracted line profile from Fig.9.8(c) we see from the inset that these bands appear to be mini depletion regions with diffusion on either side.

In this type of graded junction, doping is achieved by bombarding the sample with ion implantation process at different energies. To activate these dopants and make bonds with the lattice, the sample must be annealed causing some diffusion of the dopants locally. The dopants that are already in the sample compensate each other.

The diffusion lengths of the overall solar cell appear in Fig. 9.8(d) where we find the diffusion length for holes to be 5.96 microns by taking the natural log of the EBIC profile on the n-type side. On the p-type side we find the diffusion length of electrons to be 12.70 microns.

Chapter 10: Conclusions and Future Work

10.1 Conclusions

We have demonstrated the ability to locally probe and image carrier dynamics on the nanoscale in complex geometries.

In germanium nanowires we have observed within MSM devices applied voltages leading to the complete depletion of the channel and extracted relative potential profiles. With increasing bias past the flat band condition we observed the onset of impact ionization from holes and the creation of a built-in E field within the Ge nanowire device. The impact ionization was further enhanced when the nanowire device was back gated with a negative potential leading to an accumulation of holes reducing the number of electron available for recombination.

Studying the effects of current passing through a Ge nanowire and being conditioned we imaged with EBIC with 0V bias applied after voltage sweep. Here we saw the evolution of electrons getting trapped in the germanium oxide and leading to an accumulation of holes at the nanowire surface and bandbending in the radial direction. The bandbending started at the contacts and with greater voltages applied in the in-situ transport measurements moved towards the center. As more of the surface states were filled, the diffusion length of electrons, the minority carriers, was greatly enhanced.

In the radial hetero-structure of ohmic contacted GaAs/AlGaAs core/shell nanowire we used depth profiling to measure the electron mobility of the AlGaAs shell. With

deeper interaction volumes we probed the properties of both the core and shell materials and observed.

With Si MIS devices we demonstrated the value of EBIC towards refining semiconductor processing by spatially identifying and measuring the local electric fields at interfaces and contacts. We determined that better control of the thickness of oxide at the MIS junction was needed to make a rectifying contact and the annealing processing needed to be refined to make ohmic contacts.

Utilizing electron beam absorbed current we were able to locally map the difference between recombination and generation that was dependent of polarization and distortion to the crystal lattice in ferroelectric materials BFO and PZT. This technique can also be expanded to the studying of defects outside depletion regions in a wide number of material classes.

10.2 Future Work

EBIC as a metrology technique can probe carrier dynamics in nanoscale structures with a resolution not accessible by other methods. The value of this technique has great promise in providing a deeper understanding of the way materials interact and create fields within a device. The greater potential for EBIC however lies in correlative microscopy where a much fuller picture of how a device operates not only with electric fields but energy levels and carrier lifetimes, and changing operational conditions. The implications of this for processing technology could great accelerate the pace of innovation and lead to more discoveries.

The most obvious choice for correlative microscopy technique with EBIC is cathode-luminescence (CL), where carriers lifetimes, in time resolved CL, and energy spectra

from radiative recombination can be directly measured from the emitted light. CL typically requires using low temperature, liquid helium range, to decrease the effects of surface states where carriers can non-radiatively recombine. This can be advantageous for EBIC in exploring the effects of temperature on carrier dynamics. The optics required to measure the recombinative light in CL, can also be used to excite with light and probe the effects quasi-Fermi levels with EBIC. This also presents the possibility of measuring in micro-Raman, and photo-luminescence in the same field of view as EBIC and CL. Through the work of Ephemerion Labs with Attolight this combined EBIC and time resolved CL system is being developed.

Correlative microscopy, is not limited to in-situ measurements. Using spatial markers on a sample, ex-situ measurements can be combined with EBIC and CL into a datacube. The most obvious choices are correlating scanning probe techniques and TEM with EBIC and CL.

Bibliography

- [1] Philip Hofmann. *Physics Figures*. URL <http://users-phys.au.dk/philip/pictures/physicsfigures/physicsfigures.html>.
- [2] S.M.Sze and Kwok K. Ng. *Physics of Semiconductor Devices, 3rd Ed.* John Wiley and Sons, Jan 2006.
- [3] Deyi Fu, Jijun Zou, Kevin Wang, Rong Zhang, Dong Yu, and Junqiao Wu. Electrothermal dynamics of semiconductor nanowires under local carrier modulation. *Nano letters*, 11(9):3809–15, September 2011. ISSN 1530-6992. doi: 10.1021/nl2018806. URL <http://dx.doi.org/10.1021/nl2018806>.
- [4] Jungkil Kim, Young Heon Kim, Suk-Ho Choi, and Woo Lee. Curved silicon nanowires with ribbon-like cross sections by metal-assisted chemical etching. *ACS Nano*, 5(6):5242–5248, 2011. doi: 10.1021/nn2014358. URL <http://dx.doi.org/10.1021/nn2014358>. PMID: 21557544.
- [5] H. J. Leamy. Charge collection scanning electron microscopy. *Journal of Applied Physics*, 53(6):R51–R80, 1982. doi: <http://dx.doi.org/10.1063/1.331667>. URL <http://scitation.aip.org/content/aip/journal/jap/53/6/10.1063/1.331667>.
- [6] Ludwig Reimer. *Scanning electron microscopy: physics of image formation and microanalysis*. Springer, Jan 1998.
- [7] T. E. Everhart and P. H. Hoff. Determination of kilovolt electron energy dissipation vs penetration distance in solid materials. *Journal of Applied Physics*, 42(13):5837–5846, 1971. doi: <http://dx.doi.org/10.1063/1.1660019>. URL <http://scitation.aip.org/content/aip/journal/jap/42/13/10.1063/1.1660019>.
- [8] Hendrix Demers, Nicolas Poirier-Demers, Alexandre Ral Couture, Dany Joly, Marc Guilmain, Niels de Jonge, and Dominique Drouin. Three-dimensional electron microscopy simulation with the casino monte carlo software. *Scanning*, 33(3):135–146, 2011. ISSN 1932-8745. doi: 10.1002/sca.20262. URL <http://dx.doi.org/10.1002/sca.20262>.
- [9] D. B. Holt and E. Napchan. Quantitation of sem ebic and cl signals using monte carlo electron-trajectory simulations. *Scanning*, 16(2):78–86, 1994. ISSN 1932-8745. doi: 10.1002/sca.4950160203. URL <http://dx.doi.org/10.1002/sca.4950160203>.
- [10] W. H. Hackett, R. H. Saul, R. W. Dixon, and G. W. Kammlott. Scanning electron microscope characterization of gap redemitting diodes. *Journal of Applied Physics*, 43(6):2857–2868, 1972. doi: <http://dx.doi.org/10.1063/1.1661606>. URL <http://scitation.aip.org/content/aip/journal/jap/43/6/10.1063/1.1661606>.
- [11] W. H. Hackett. Electronbeam excited minoritycarrier diffusion profiles in semiconductors. *Journal of Applied Physics*, 43(4):1649–1654, 1972. doi: <http://dx.doi.org/10.1063/1.1661375>. URL <http://scitation.aip.org/content/aip/journal/jap/43/4/10.1063/1.1661375>.
- [12] H.K. Kuiken. Theory of lifetime measurements with the scanning electron microscope: Transient analysis. *Solid-State Electronics*, 19(6):447 – 450, 1976. ISSN 0038-1101. doi: [http://dx.doi.org/10.1016/0038-1101\(76\)90004-6](http://dx.doi.org/10.1016/0038-1101(76)90004-6). URL <http://www.sciencedirect.com/science/article/pii/0038110176900046>.

- [13] D E Ioannou. A sem-ebic minority-carrier lifetime-measurement technique. *Journal of Physics D: Applied Physics*, 13(4):611, 1980. URL <http://stacks.iop.org/0022-3727/13/i=4/a=014>.
- [14] N. C. MacDonald and T. E. Everhart. Direct measurement of the depletion layer width variation vs applied bias for a pn junction. *Applied Physics Letters*, 7(10):267–269, 1965. doi: <http://dx.doi.org/10.1063/1.1754252>. URL <http://scitation.aip.org/content/aip/journal/apl/7/10/10.1063/1.1754252>.
- [15] Jim-Yong Chi and Harry C. Gatos. Nondestructive determination of the depth of planar p-n junctions by scanning electron microscopy. *Electron Devices, IEEE Transactions on*, 24(12):1366–1368, Dec 1977. ISSN 0018-9383. doi: 10.1109/T-ED.1977.19017.
- [16] Naotaka Kuroda, Chiaki Sasaoka, Akitaka Kimura, Akira Usui, and Yasunori Mochizuki. Precise control of pn-junction profiles for gan-based {LD} structures using gan substrates with low dislocation densities. *Journal of Crystal Growth*, 189190:551 – 555, 1998. ISSN 0022-0248. doi: [http://dx.doi.org/10.1016/S0022-0248\(98\)00191-2](http://dx.doi.org/10.1016/S0022-0248(98)00191-2). URL <http://www.sciencedirect.com/science/article/pii/S0022024898001912>.
- [17] D.B. Holt and B.G. Yacobi. *Extended Defects in Semiconductors: Electronic Properties, Device Effects and Structures*, pages 442–446. Cambridge University Press, 2007.
- [18] J Chen, T Sekiguchi, D Yang, F Yin, K Kido, and S Tsurekawa. Electron-beam-induced current study of grain boundaries in multicrystalline silicon. *Journal of Applied Physics*, 96(10):5490–5495, 2004.
- [19] M Kittler and W Seifert. On the origin of electron-beam-induced-current contrast of extended defects in silicon. *Scanning microscopy*, 6(4):979–991, 1992.
- [20] B Raza and DB Holt. Ebic contrast of grain boundaries in polycrystalline silicon solar cells.
- [21] K. Mizukoshi, T. Oyamada, A. Shimase, Y. Matsumoto, S. Yorisaki, and T. Majima. Fault location using electron beam current absorbed in lsi interconnects. In *Future of Electron Devices, 2004. International Meeting for*, pages 31–32, July 2004. doi: 10.1109/IMFEDK.2004.1566393.
- [22] Wen Pin Lin and Hsiu Ju Chang. Physical failure analysis cases by electron beam absorbed current amp; electron beam induced current detection on nano-probing sem system. In *Physical and Failure Analysis of Integrated Circuits (IPFA), 2010 17th IEEE International Symposium on the*, pages 1–4, July 2010. doi: 10.1109/IPFA.2010.5532245.
- [23] S. Wei, Soonhuat Lim, M. Zulkifli, Syahirah, and D. Khatri. Optimization and application of electron beam absorbed current technique. In *Physical and Failure Analysis of Integrated Circuits (IPFA), 2015 IEEE 22nd International Symposium on the*, pages 250–254, June 2015. doi: 10.1109/IPFA.2015.7224371.
- [24] Jonathan E. Allen, Eric R. Hemesath, Daniel E. Perea, Jessica L. Lensch-Falk, LiZ. Y., Feng Yin, Mhairi H. Gass, Peng Wang, Andrew L. Bleloch, Richard E. Palmer, and Lincoln J. Lauhon. High-resolution detection of au catalyst atoms in si nanowires. *Nat. Nano*, 3(3):168–173, 03 2008.
- [25] Anders Gustafsson, Mikael T Björk, and Lars Samuelson. Locating nanowire heterostructures by electron beam induced current. *Nanotechnology*, 18(20):205306, 2007.
- [26] Alfredo M. Morales and Charles M. Lieber. A laser ablation method for the synthesis of crystalline semiconductor nanowires. *Science*, 279(5348):208–211, 1998. doi: 10.1126/science.279.5348.208. URL <http://www.sciencemag.org/content/279/5348/208.abstract>.

- [27] Zhipeng Huang, Nadine Geyer, Peter Werner, Johannes de Boor, and Ulrich Gsele. Metal-assisted chemical etching of silicon: A review. *Advanced Materials*, 23(2):285–308, 2011. ISSN 1521-4095. doi: 10.1002/adma.201001784. URL <http://dx.doi.org/10.1002/adma.201001784>.
- [28] Lincoln J Lauhon, Mark S Gudiksen, Deli Wang, and Charles M Lieber. Epitaxial core–shell and core–multishell nanowire heterostructures. *Nature*, 420(6911):57–61, 2002.
- [29] Sabine Kolodinski, Jurgen H. Werner, Thomas Wittchen, and Hans J. Queisser. Quantum efficiencies exceeding unity due to impact ionization in silicon solar cells. *Applied Physics Letters*, 63(17):2405–2407, 1993. doi: 10.1063/1.110489. URL <http://link.aip.org/link/?APL/63/2405/1>.
- [30] William A. Tisdale, Kenrick J. Williams, Brooke A. Timp, David J. Norris, Eray S. Aydil, and X.-Y. Zhu. Hot-electron transfer from semiconductor nanocrystals. *Science*, 328(5985):1543–1547, 2010. doi: 10.1126/science.1185509. URL <http://www.sciencemag.org/content/328/5985/1543.abstract>.
- [31] Christophe Delerue, Guy Allan, J. J. H. Pijpers, and M. Bonn. Carrier multiplication in bulk and nanocrystalline semiconductors: Mechanism, efficiency, and interest for solar cells. *Phys. Rev. B*, 81:125306, Mar 2010. doi: 10.1103/PhysRevB.81.125306. URL <http://link.aps.org/doi/10.1103/PhysRevB.81.125306>.
- [32] Guannan Chen, Eric M. Gallo, Oren D. Leaffer, Terrence McGuckin, Paola Prete, Nico Lovergne, and Jonathan E. Spanier. Tunable hot-electron transfer within a single core-shell nanowire. *Phys. Rev. Lett.*, 107:156802, Oct 2011. doi: 10.1103/PhysRevLett.107.156802. URL <http://link.aps.org/doi/10.1103/PhysRevLett.107.156802>.
- [33] John W. Gaylord. Microplasma observations in silicon junctions using a scanning electron beam. *J Electrochem Soc*, 113(7):753–754, 1966. doi: 10.1149/1.2424108.
- [34] N. F. B. Neve, K. A. Hughes, and P. R. Thornton. Scanning electron microscope as a means of studying microplasmas at high resolution. *J. Appl. Phys.*, 37(4):1704–1709, 1966. doi: 10.1063/1.1708587.
- [35] William Shockley. Problems related to p-n junctions in silicon. *Solid State Electron.*, 2(1):35 – 60, IN9-IN10, 61–67, 1961. ISSN 0038-1101. doi: DOI:10.1016/0038-1101(61)90054-5.
- [36] Y. H. Ahn and Jiwoong Park. Efficient visible light detection using individual germanium nanowire field effect transistors. *Appl. Phys. Lett.*, 91(16):162102, 2007. doi: 10.1063/1.2799253.
- [37] Guannan Chen, Eric Gallo, Joan Burger, Bahram Nabet, Jonathan E. Spanier, Adriano Cola, Paola Prete, and Nico Lovergne. On direct-writing methods for electrically contacting gaas and ge nanowire devices. *Appl. Phys. Lett.*, in press(1), 2010.
- [38] Nicholas W. M. Ritchie. A new monte carlo application for complex sample geometries. *Surf. Interface Anal.*, 37(11):1006–1011, 2005.
- [39] Yeonghwan Ahn, James Dunning, and Jiwoong Park. Scanning photocurrent imaging and electronic band studies in silicon nanowire field effect transistors. *Nano Lett.*, 5(7):1367–1370, 06 2005.
- [40] Jonathan E. Allen, Daniel E. Perea, Eric R. Hemesath, and Lincoln J. Lauhon. Nonuniform nanowire doping profiles revealed by quantitative scanning photocurrent microscopy. *Adv. Mater.*, 21(30):3067–3072, 2009.
- [41] E. Koren, Y. Rosenwaks, J. E. Allen, E. R. Hemesath, and L. J. Lauhon. Nonuniform doping distribution along silicon nanowires measured by kelvin probe force microscopy and scanning photocurrent microscopy. *Appl. Phys. Lett.*, 95(9):092105, 2009. doi: 10.1063/1.3207887.

- [42] Marcus Freitag, James C. Tsang, Ageeth Bol, Dongning Yuan, Jie Liu, and Phaedon Avouris. Imaging of the schottky barriers and charge depletion in carbon nanotube transistors. *Nano Lett.*, 7(7):2037–2042, 06 2007.
- [43] Katsuhiro Tomioka, Masatoshi Yoshimura, and Takashi Fukui. A IIIV nanowire channel on silicon for high-performance vertical transistors. *Nature*, 488(111):0–4, 2012. ISSN 00280836. doi: 10.1038/nature11293. URL <http://www.nature.com/doifinder/10.1038/nature11293>.
- [44] V S Pribiag, S Nadj-Perge, S M Frolov, J W G van den Berg, I van Weperen, S R Plissard, E P A M Bakkers, and L P Kouwenhoven. Electrical control of single hole spins in nanowire quantum dots. *Nature nanotechnology*, 8(3):170–174, February 2013. ISSN 1748-3395. doi: 10.1038/nnano.2013.5. URL <http://dx.doi.org/10.1038/nnano.2013.5>.
- [45] Linyou Cao, Bahram Nabet, and Jonathan E. Spanier. Enhanced raman scattering from individual semiconductor nanocones and nanowires. *Phys. Rev. Lett.*, 96:157402, Apr 2006. doi: 10.1103/PhysRevLett.96.157402. URL <http://link.aps.org/doi/10.1103/PhysRevLett.96.157402>.
- [46] Linyou Cao, Justin S. White, Joon-Shik Park, Jon A. Schuller, Bruce M. Clemens, and Mark L. Brongersma. Engineering light absorption in semiconductor nanowire devices. *Nat Mater.*, 8(8):643–647, 2009. ISSN 1476-1122. doi: 10.1038/nmat2477. URL <http://dx.doi.org/10.1038/nmat2477>
<http://www.nature.com/nmat/journal/v8/n8/abs/nmat2477.html>
<http://www.nature.com/nmat/journal/v8/n8/pdf/nmat2477.pdf>.
- [47] Michael D. Kelzenberg, Shannon W. Boettcher, Jan A. Petykiewicz, Daniel B. Turner-Evans, Morgan C. Putnam, Emily L. Warren, Joshua M. Spurgeon, Ryan M. Briggs, Nathan S. Lewis, and Harry A. Atwater. Enhanced absorption and carrier collection in Si wire arrays for photovoltaic applications. *Nat Mater.*, 9(3):239–244, March 2010. ISSN 1476-1122. doi: 10.1038/nmat2635. URL <http://dx.doi.org/10.1038/nmat2635>
<http://www.nature.com.ezproxy2.library.drexel.edu/nmat/journal/v9/n3/full/nmat2635.html>
<http://www.nature.com.ezproxy2.library.drexel.edu/nmat/journal/v9/n3/pdf/nmat2635.pdf>.
- [48] Ramesh G Mani, Jürgen H Smet, Klaus von Klitzing, Venkatesh Narayanamurti, William B Johnson, and Vladimir Umansky. Zero-resistance states induced by electromagnetic-wave excitation in GaAs/AlGaAs heterostructures. *Nature*, 420(6916):646–50, December 2002. ISSN 0028-0836. doi: 10.1038/nature01277. URL <http://dx.doi.org/10.1038/nature01277>.
- [49] R.G. Walker. High-speed III-V semiconductor intensity modulators. *IEEE Journal of Quantum Electronics*, 27(3):654–667, March 1991. ISSN 00189197. doi: 10.1109/3.81374. URL http://apps.webofknowledge.com/full_record.do?product=UA&search_mode=GeneralSearch&qid=5&SID=4EqyTJfypvUZ4rp2qnQ&page=1&doc=2.
- [50] Sadao Adachi. GaAs, AlAs, and Al_xGa_{1-x}As Material parameters for use in research and device applications. *Journal of Applied Physics*, 58(3):R1, 1985. ISSN 00218979. doi: 10.1063/1.336070. URL <http://link.aip.org/link/JAPIAU/v58/i3/pR1/s1&Agg=doi>.
- [51] K. Hess, H. Morkoc, H. Shichijo, and B. G. Streetman. Negative differential resistance through real-space electron transfer. *Applied Physics Letters*, 35(6):469, 1979. ISSN 00036951. doi: 10.1063/1.91172. URL <http://link.aip.org.ezproxy2.library.drexel.edu/link/APPLAB/v35/i6/p469/s1&Agg=doi>.
- [52] Guannan Chen, Eric Gallo, Oren Leaffer, Terrence McGuckin, Paola Prete, Nico Lovergne, and Jonathan Spanier. Tunable Hot-Electron Transfer Within a Single Core-Shell Nanowire. *Physical Review Letters*, 107(15):1–5, 2011. ISSN 00319007. doi: 10.1103/PhysRevLett.107.156802. URL <http://link.aps.org/doi/10.1103/PhysRevLett.107.156802>.

- [53] Kimberly A Dick, Philippe Caroff, Jessica Bolinsson, Maria E Messing, Jonas Johansson, Knut Deppert, L Reine Wallenberg, and Lars Samuelson. Control of IIIV nanowire crystal structure by growth parameter tuning. *Semiconductor Science and Technology*, 25(2):024009, February 2010. ISSN 0268-1242, 1361-6641. doi: 10.1088/0268-1242/25/2/024009. URL <http://iopscience.iop.org/0268-1242/25/2/024009>http://iopscience.iop.org/0268-1242/25/2/024009/pdf/0268-1242_25_2_024009.pdf.
- [54] Peter Krogstrup, Ronit Popovitz-Biro, Erik Johnson, Morten Hannibal Madsen, Jesper Nygård, and Hadas Shtrikman. Structural phase control in self-catalyzed growth of GaAs nanowires on silicon (111). *Nano letters*, 10(11):4475–82, November 2010. ISSN 1530-6992. doi: 10.1021/nl102308k. URL <http://dx.doi.org/10.1021/nl102308k>.
- [55] Guannan Chen, Guan Sun, Yujie J. Ding, Paola Prete, Ilio Miccoli, Nico Lovergne, Hadas Shtrikman, Patrick Kung, Tsachi Livneh, and Jonathan E. Spanier. Direct measurement of band edge discontinuity in individual coreshell nanowires by photocurrent spectroscopy. *Nano Letters*, 13(9):4152–4157, 2013. doi: 10.1021/nl401737u. URL <http://pubs.acs.org/doi/abs/10.1021/nl401737u>.
- [56] S. Thunich, L. Prechtel, D. Spirkoska, G. Abstreiter, A. Fontcuberta i Morral, and A. W. Holleitner. Photocurrent and photoconductance properties of a GaAs nanowire. *Applied Physics Letters*, 95(8):083111, August 2009. ISSN 00036951. doi: 10.1063/1.3193540. URL <http://link.aip.org/link/?APPLAB/95/083111/1>.
- [57] Eric M Gallo, Guannan Chen, Marc Currie, Terrence McGuckin, Paola Prete, Nico Lovergne, Bahram Nabet, and Jonathan E Spanier. Picosecond response times in GaAs/AlGaAs core/shell nanowire-based photodetectors. *Applied Physics Letters*, 98(24):241113, 2011. ISSN 00036951. doi: 10.1063/1.3600061. URL <http://link.aip.org/link/APPLAB/v98/i24/p241113/s1&Agg=doi>.
- [58] O. Demichel, M. Heiss, J. Bleuse, H. Mariette, and A. Fontcuberta i Morral. Impact of surfaces on the optical properties of GaAs nanowires. *Applied Physics Letters*, 97(20):201907, 2010. ISSN 00036951. doi: 10.1063/1.3519980. URL <http://link.aip.org.ezproxy2.library.drexel.edu/link/APPLAB/v97/i20/p201907/s1&Agg=doi>.
- [59] Kristian Storm, Filip Halvardsson, Magnus Heurlin, David Lindgren, Anders Gustafsson, Phillip M Wu, Bo Monemar, and Lars Samuelson. Spatially resolved Hall effect measurement in a single semiconductor nanowire. *Nature nanotechnology*, 7(11):718–722, October 2012. ISSN 1748-3395. doi: 10.1038/nnano.2012.190. URL <http://dx.doi.org/10.1038/nnano.2012.190>.
- [60] Mohammad Montazeri, Howard E Jackson, Leigh M Smith, Jan M Yarrison-Rice, Jung-Hyun Kang, Qiang Gao, Hark Hoe Tan, and Chennupati Jagadish. Transient Rayleigh scattering: a new probe of picosecond carrier dynamics in a single semiconductor nanowire. *Nano letters*, 12(10):5389–95, October 2012. ISSN 1530-6992. doi: 10.1021/nl302767u. URL <http://dx.doi.org/10.1021/nl302767u>.
- [61] Y. Gu, E.-S. Kwak, J. L. Lensch, J. E. Allen, T. W. Odom, and L. J. Lauhon. Near-field scanning photocurrent microscopy of a nanowire photodetector. *Applied Physics Letters*, 87(4):043111–3, July 2005. doi: 10.1063/1.1996851. URL <http://link.aip.org/link/?APL/87/043111/1>.
- [62] Christoph Gutsche, Raphael Niepelt, Martin Gnauck, Andrey Lysov, Werner Prost, Carsten Ronning, and Franz-Josef Tegude. Direct Determination of Minority Carrier Diffusion Lengths at Axial GaAs Nanowire p-n Junctions. *Nano letters*, 12(3):1453–8, March 2012. ISSN 1530-6992. doi: 10.1021/nl204126n. URL <http://dx.doi.org/10.1021/nl204126n>.

- [63] M. Kittler, C. Ulhaq-Bouillet, and V. Higgs. Influence of copper contamination on recombination activity of misfit dislocations in SiGe/Si epilayers: Temperature dependence of activity as a marker characterizing the contamination level. *Journal of Applied Physics*, 78(7):4573, October 1995. ISSN 00218979. doi: 10.1063/1.359802. URL <http://link.aip.org/link/?JAPIAU/78/4573/1>.
- [64] A. Eisenbeiss, H. Heinrich, J. Opschoor, R. P Tijburg, and H. Preier. Determination of the bandedge offset in heterojunctions by electron beam induced current (GaAs/GaAlAs). *Applied Physics Letters*, 50(22):1583–1585, June 1987. ISSN 00036951. doi: doi:10.1063/1.97787. URL http://apl.aip.org/resource/1/applab/v50/i22/p1583_s1http://link.aip.org/link/?APPLAB/50/1583/1/pdf.
- [65] Jie Xiang, Wei Lu, Yongjie Hu, Yue Wu, Hao Yan, and Charles M Lieber. Ge/Si nanowire heterostructures as high-performance field-effect transistors. *Nature*, 441(7092):489–93, May 2006. ISSN 1476-4687. doi: 10.1038/nature04796. URL <http://www.nature.com.ezproxy2.library.drexel.edu/nature/journal/v441/n7092/full/nature04796.html>.
- [66] Yeonghwan Ahn, James Dunning, and Jiwoong Park. Scanning Photocurrent Imaging and Electronic Band Studies in Silicon Nanowire Field Effect Transistors. *Nano Letters*, 5(7):1367–1370, July 2005. ISSN 1530-6984. doi: 10.1021/nl050631x. URL <http://dx.doi.org/10.1021/nl050631x>.
- [67] Olaf Wunnicke. Gate capacitance of back-gated nanowire field-effect transistors. *Applied Physics Letters*, 89(8):083102, August 2006. ISSN 00036951. doi: 10.1063/1.2337853. URL <http://link.aip.org/link/?APPLAB/89/083102/1>.
- [68] D. R. Khanal and J. Wu. Gate Coupling and Charge Distribution in Nanowire Field Effect Transistors. *Nano Letters*, 7(9):2778–2783, 2007. doi: 10.1021/nl071330l. URL <http://dx.doi.org/10.1021/nl071330lhttp://pubs.acs.org/doi/full/10.1021/nl071330l>.
- [69] Kristian Storm, Gustav Nylund, Lars Samuelson, and Adam P Micolich. Realizing lateral wrap-gated nanowire FETs: controlling gate length with chemistry rather than lithography. *Nano letters*, 12(1):1–6, January 2012. ISSN 1530-6992. doi: 10.1021/nl104403g. URL <http://dx.doi.org/10.1021/nl104403g>.
- [70] H. A. Zarem, P. C. Sercel, J. A. Leibens, L. E. Eng, A. Yariv, and K. J. Vahala. Direct determination of the ambipolar diffusion length in GaAs/AlGaAs heterostructures by cathodoluminescence. *Applied Physics Letters*, 55(16):1647, October 1989. ISSN 00036951. doi: 10.1063/1.102226. URL <http://link.aip.org/link/?APPLAB/55/1647/1>.
- [71] David Ferry. *Semiconductor Transport*. Taylor & Francis, 2000. ISBN 0748408665.
- [72] P. Prete, F. Marzo, P. Paiano, N. Lovergne, G. Salviati, L. Lazzarini, and T. Sekiguchi. Luminescence of GaAs/AlGaAs core-shell nanowires grown by MOVPE using tertiarybutylarsine. *Journal of Crystal Growth*, 310(23):5114–5118, November 2008. ISSN 0022-0248. doi: 10.1016/j.jcrysgr.2008.08.039.
- [73] Leonhard Prechtel, Milan Padilla, Nadine Erhard, Helmut Karl, Gerhard Abstreiter, Anna Fontcuberta I Morral, and Alexander W. Holleitner. Time-Resolved Photoinduced Thermoelectric and Transport Currents in GaAs Nanowires. *Nano Letters*, page 120417132814007, April 2012. ISSN 1530-6984. doi: 10.1021/nl300262j. URL <http://dx.doi.org/10.1021/nl300262j>.
- [74] Erik Garnett and Peidong Yang. Light trapping in silicon nanowire solar cells. *Nano Letters*, 10(3):1082–1087, 2010. doi: 10.1021/nl100161z. URL <http://dx.doi.org/10.1021/nl100161z>. PMID: 20108969.

- [75] Erik C. Garnett and Peidong Yang. Silicon nanowire radial pn junction solar cells. *Journal of the American Chemical Society*, 130(29):9224–9225, 2008. doi: 10.1021/ja8032907. URL <http://dx.doi.org/10.1021/ja8032907>. PMID: 18576622.
- [76] Andrew Barnabas Wong, Sarah Brittman, Yi Yu, Neil P. Dasgupta, and Peidong Yang. Coreshell cdscu2s nanorod array solar cells. *Nano Letters*, 15(6):4096–4101, 2015. doi: 10.1021/acs.nanolett.5b01203. URL <http://dx.doi.org/10.1021/acs.nanolett.5b01203>. PMID: 25993088.
- [77] Michael D. Kelzenberg, Daniel B. Turner-Evans, Brendan M. Kayes, Michael A. Filler, Morgan C. Putnam, Nathan S. Lewis, and Harry A. Atwater. Photovoltaic measurements in single-nanowire silicon solar cells. *Nano Letters*, 8(2):710–714, 2008. doi: 10.1021/nl072622p. URL <http://dx.doi.org/10.1021/nl072622p>. PMID: 18269257.
- [78] Bozhi Tian, Xiaolin Zheng, Thomas J Kempa, Ying Fang, Nanfang Yu, Guihua Yu, Jinlin Huang, and Charles M Lieber. Coaxial silicon nanowires as solar cells and nanoelectronic power sources. *Nature*, 449(7164):885–889, 2007.
- [79] Brendan M. Kayes, Harry A. Atwater, and Nathan S. Lewis. Comparison of the device physics principles of planar and radial p-n junction nanorod solar cells. *Journal of Applied Physics*, 97(11):114302, 2005. doi: <http://dx.doi.org/10.1063/1.1901835>. URL <http://scitation.aip.org/content/aip/journal/jap/97/11/10.1063/1.1901835>.
- [80] Cheol-Joo Kim, Hyun-Seung Lee, Yong-Jun Cho, Kibum Kang, and Moon-Ho Jo. Diameter-dependent internal gain in ohmic ge nanowire photodetectors. *Nano Letters*, 10(6):2043–2048, 2010. doi: 10.1021/nl100136b. URL <http://dx.doi.org/10.1021/nl100136b>. PMID: 20420371.
- [81] Youfan Hu, Yang Liu, Wenliang Li, Min Gao, Xuelei Liang, Quan Li, and Lian-Mao Peng. Observation of a 2d electron gas and the tuning of the electrical conductance of zno nanowires by controllable surface band-bending. *Advanced Functional Materials*, 19(15):2380–2387, 2009. ISSN 1616-3028. doi: 10.1002/adfm.200900179. URL <http://dx.doi.org/10.1002/adfm.200900179>.
- [82] G. Gu, M. Burghard, G. T. Kim, G. S. Dsberg, P. W. Chiu, V. Krstic, S. Roth, and W. Q. Han. Growth and electrical transport of germanium nanowires. *Journal of Applied Physics*, 90(11): 5747–5751, 2001. doi: <http://dx.doi.org/10.1063/1.1413495>. URL <http://scitation.aip.org/content/aip/journal/jap/90/11/10.1063/1.1413495>.
- [83] Tobias Hanrath and Brian A. Korgel. Influence of surface states on electron transport through intrinsic ge nanowires. *J. Phys. Chem. B*, 109(12):5518–5524, 02 2005.
- [84] Dunwei Wang, Ying-Lan Chang, Qian Wang, Jien Cao, Damon B. Farmer, Roy G. Gordon, , and Hongjie Dai*. Surface chemistry and electrical properties of germanium nanowires. *Journal of the American Chemical Society*, 126(37):11602–11611, 2004. doi: 10.1021/ja047435x. URL <http://dx.doi.org/10.1021/ja047435x>. PMID: 15366907.
- [85] L. C. Campos, M. H. D. Guimaraes, A. M. B. Goncalves, S. de Oliveira, and R. G. Lacerda. Zno uv photodetector with controllable quality factor and photosensitivity. *AIP Advances*, 3(2): 022104, 2013. doi: <http://dx.doi.org/10.1063/1.4790633>. URL <http://scitation.aip.org/content/aip/journal/adva/3/2/10.1063/1.4790633>.
- [86] Cheng-Ying Chen, Jose Ramon Duran Retamal, I-Wen Wu, Der-Hsien Lien, Ming-Wei Chen, Yong Ding, Yu-Lun Chueh, Chih-I Wu, and Jr-Hau He. Probing surface band bending of surface-engineered metal oxide nanowires. *ACS Nano*, 6(11):9366–9372, 2012. doi: 10.1021/nn205097e. URL <http://dx.doi.org/10.1021/nn205097e>. PMID: 23092152.

- [87] R. H. Kingston. Review of germanium surface phenomena. *Journal of Applied Physics*, 27(2): 101–114, 1956. doi: <http://dx.doi.org/10.1063/1.1722317>. URL <http://scitation.aip.org/content/aip/journal/jap/27/2/10.1063/1.1722317>.
- [88] S. Roy Morrison. Slow surface reaction on germanium. *Phys. Rev.*, 102:1297–1301, Jun 1956. doi: 10.1103/PhysRev.102.1297. URL <http://link.aps.org/doi/10.1103/PhysRev.102.1297>.
- [89] R. H. Kingston and A. L. McWhorter. Relaxation time of surface states on germanium. *Phys. Rev.*, 103:534–540, Aug 1956. doi: 10.1103/PhysRev.103.534. URL <http://link.aps.org/doi/10.1103/PhysRev.103.534>.
- [90] Shixiong Zhang, Eric R. Hemesath, Daniel E. Perea, Edy Wijaya, Jessica L. Lensch-Falk, and Lincoln J. Lauhon. Relative influence of surface states and bulk impurities on the electrical properties of ge nanowires. *Nano Lett.*, 9(9):3268–3274, 08 2009.
- [91] Tobias Hanrath and Brian A. Korgel. Chemical surface passivation of ge nanowires. *J. AM. CHEM. SOC.*, 126(47):15466–15472, 11 2004.
- [92] Ludwig Reimer. *Transmission electron microscopy: physics of image formation and microanalysis*, volume 36. Springer, 2013.
- [93] C.R. Winkler, A.R. Damodaran, J. Karthik, L.W. Martin, and M.L. Taheri. Direct observation of ferroelectric domain switching in varying electric field regimes using in situ {TEM}. *Micron*, 43(11):1121 – 1126, 2012. ISSN 0968-4328. doi: <http://dx.doi.org/10.1016/j.micron.2012.02.009>. URL <http://www.sciencedirect.com/science/article/pii/S0968432812000522>. In situ {TEM}.
- [94] P.G. Lucua, V. Teodorescu, and F. Vasiliu. Sem, saed, and tem investigations of domain structure in pzt ceramics at morphotropic phase boundary. *Applied Physics A*, 37(4):237–242, 1985. ISSN 0947-8396. doi: 10.1007/BF00614823. URL <http://dx.doi.org/10.1007/BF00614823>.
- [95] KSA Novoselov, Andre K Geim, SVb Morozov, Da Jiang, MIc Katsnelson, IVa Grigorieva, SVb Dubonos, and AAb Firsov. Two-dimensional gas of massless dirac fermions in graphene. *nature*, 438(7065):197–200, 2005.
- [96] Kin Fai Mak, Changgu Lee, James Hone, Jie Shan, and Tony F. Heinz. Atomically thin mos₂: A new direct-gap semiconductor. *Phys. Rev. Lett.*, 105:136805, Sep 2010. doi: 10.1103/PhysRevLett.105.136805. URL <http://link.aps.org/doi/10.1103/PhysRevLett.105.136805>.

Vita

Subsurface Imaging of Coupled Carrier Transport in GaAs/AlGaAs CoreShell Nanowires, Guannan Chen , Terrence McGuckin , Christopher J. Hawley , Eric M. Gallo , Paola Prete , Ilio Miccoli , Nico Lovergne , and Jonathan E. Spanier, Nano Lett., 2015, 15 (1), pp 7579 DOI: 10.1021/nl502995q

Selective epitaxial growth on germanium nanowires via hybrid oxide-stabilized/vapor-liquid-solid growth, C. J. Hawley, T. McGuckin and J. E. Spanier, Crystal Growth and Design, ASAP (2013) DOI: 10.1021/cg3016595.

The ferroelectric field effect in an integrated core-shell nanowire, S. S. Nonnenmann, M. A. Islam, B. R. Beatty, E. M. Gallo, T. McGuckin, and J. E. Spanier, Adv. Func. Mater. (2012), DOI: 10.1002/adfm.201200865.

Tunable hot-electron transfer within a single core-shell nanowire, G. Chen, E. M. Gallo, O. D. Leaffer, T. McGuckin, P. Prete, N. Lovergne, and J. E. Spanier, Phys. Rev. Lett. 107, 156802 (2011), Picosecond response times in GaAs/AlGaAs core/shell nanowire-based photodetectors, E. M. Gallo, G. Chen, M. Currie, T. McGuckin, P. Prete, N. Lovergne, B. Nabot and J. E. Spanier, Appl. Phys. Lett. 98, 241113 (2011). Selected for inclusion in the July 4, 2011 issue of Virtual Journal of Nanoscience and Technology.

